JOURNAL OF
PETROLOGY

Journal of Petrology, 2021, Vol. 62, No. 9, 1–39
doi: 10.1093/petrology/egab041
Advance Access Publication Date: 9 June 2021
Original Manuscript

OXFORD

Geochemical Systematics of High Arctic Large Igneous Province Continental Tholeiites from Canada—Evidence for Progressive Crustal Contamination in the Plumbing System

Jean H. Bédard[1,*], Benoit Michel Saumur[2], Christian Tegner[3], Valentin R. Troll[4], Frances M. Deegan[4], Carol A. Evenchick[5], Stephen E. Grasby[6] and Keith Dewing[6]

[1]Geological Survey of Canada, 490 de la Couronne, Québec, QC G1K 9A9, Canada; [2]Département des sciences de la Terre et de l'atmosphère, Université du Québec à Montréal, 201 av. du Président-Kennedy, Montréal, QC H2X 3Y7, Canada; [3]Department of Geoscience, Centre of Earth System Petrology, Aarhus University, Denmark; [4]Department of Earth Sciences, Section for Natural Resources & Sustainable Development, Uppsala University, Villavägen 16, 75236, Sweden; [5]Geological Survey of Canada, 605 Robson Street, Vancouver, BC V6B 5J3, Canada; [6]Geological Survey of Canada, 3303 33rd St NW, Calgary, AB T2L 2A7, Canada

*Corresponding author. E-mail: JeanH.Bedard@RNCan-NRCan.gc.ca

Received 2 July 2020; Accepted 23 May 2021

ABSTRACT

Cretaceous High Arctic large igneous province (HALIP) sub-alkaline magmatic rocks in Canada are mostly evolved (MgO 2–7 wt%), sparsely plagioclase + clinopyroxene ± olivine-phyric tholeiitic basalts. There were two main HALIP continental flood basalt (CFB) eruption episodes: 135–120 Ma (Isachsen Fm.) and 105–90 Ma (Strand Fiord Fm.), both associated with cogenetic doleritic sills and dykes. Building on a large modern database, 16 HALIP tholeiite types are defined and grouped into genetic series using Ce vs Sm/Yb_{NMORB} distributions. Comparison with model melting curves implies that higher-Sm/Yb HALIP basalt types record low-degree melting of garnet-bearing mantle sources. More voluminous intermediate- and low-Sm/Yb HALIP basalt types separated from the mantle at shallower levels after further extensive melting in the spinel-peridotite field. Within a given Sm/Yb range, increases in incompatible elements such as Ce are coupled with progressive clockwise rotation of normalized incompatible trace element profiles. Trace element modeling implies this cannot be due to closed-system fractional crystallization but requires progressive and ubiquitous incorporation of a component resembling continental crust. The fractionation models imply that low-Sm/Yb HALIP basalts (~7 wt% MgO) initially crystallized olivine gabbro assemblages, with lower-MgO basalts successively crystallizing gabbro and ilmenite-gabbro assemblages. In contrast, higher-Sm/Yb basalts fractionated more clinopyroxene and ilmenite, but extensive plagioclase fractionation is still required to explain developing negative Sr–Eu anomalies. Back-fractionation models require about 40 % addition of olivine to bring the most primitive HALIP basalts (~7 % MgO) into equilibrium with Fo_{89} mantle. Inverse fractionation–assimilation modeling shrinks the CFB signature, making decontaminated model parental melts more similar to enriched mid-ocean ridge basalt. The progressive increase of the contamination signature within each HALIP tholeiitic differentiation series is not consistent with models involving derivation of HALIP basalts from a mantle source previously enriched by subduction. Strong interaction of basalt with Sverdrup Basin sedimentary rocks may cause localized over-enrichment in K–Rb–Th–U, but cannot explain strong Ba enrichment in the absence of concomitant K–Rb–Th–U enrichment. The localized Ba enrichment could reflect either a Ba-rich lithospheric mantle component that is strongly manifested in the coeval HALIP alkaline suites, or syn- to post-emplacement fluid-mediated transfer from Ba-rich host rocks.

Key words: *basalt*; *contamination*; *continental LIP*; *HALIP*; *plumbing system*

INTRODUCTION

The most voluminous manifestations of continental large igneous provinces (LIPs) are continental flood basalt (CFB) suites (Ernst, 2014), many with distinctive geochemical signatures such as enrichment of K–Rb–Th–U and depletion of Nb–Ta–Ti that imply interaction with a continental reservoir. In oceanic environments there is debate about the nature and location of the enriched components responsible for the normal mid-ocean ridge basalt (N-MORB) to ocean island basalt (OIB) geochemical spectrum (e.g. Gast, 1968; Viereck *et al.*, 1989; Weaver, 1991; Hofmann, 1997; Anderson, 2005; Sobolev *et al.*, 2007; Willbold & Stracke, 2010; Weis *et al.*, 2011; Stracke, 2012). Similar OIB-like fertile components may also be involved in the genesis of continental basalts, but constraining their potential contribution is hampered by common post-segregation contamination by continental crust and/or lithospheric mantle (Lassiter & DePaolo, 1997). One end-member view is that most tholeiitic CFBs and associated alkaline magmas were similar to oceanic plateau basalts or OIB prior to their exposure to lithospheric influences (DePaolo, 1981; Arndt *et al.*, 1993; Anderson, 1994; Bhattacharya *et al.*, 2013; Heinonen *et al.*, 2016; Ashwal, 2021), and that the continental trace element signatures of CFBs are primarily the result of extensive shallow assimilation of continental crust. Other researchers have proposed that CFBs acquired their distinctive continental signatures before arriving in the crust; but there is diversity of opinion concerning where and how this might have happened. High-volume CFB events could imply a major mantle thermal anomaly, such as a deep-rooted plume, but could also reflect enhanced melt productivity caused by an enriched source residing in the æsthenosphere (Foulger *et al.*, 2005). Fertile components could be dispersed in an ascending plume or ambient æsthenosphere, but could also occur as veins or enriched metasomatic zones in the sub-continental lithospheric mantle (SCLM). Many believe that metasomatized SCLM can itself experience bulk melting to generate CFBs, or alternatively, contaminate ascending æsthenospheric melts (Ellam & Cox, 1991; Hawkesworth *et al.*, 1992; Ionov *et al.*, 1993; Lightfoot *et al.*, 1993; Gibson *et al.*, 1995; Turner & Hawkesworth, 1995; Puffer, 2001; Murphy & Dostal, 2007; Jourdan *et al.*, 2007, 2009; Zhang *et al.*, 2008; Rooney *et al.*, 2017). Others have argued that CFBs come directly from æsthenospheric mantle domains that were mechanically mixed with continental sediments and metasomatized subduction zone wedges during orogenic terrane assembly (Callegaro *et al.*, 2014; Merle *et al.*, 2014; Whalen *et al.*, 2015; Marzoli *et al.*, 2018; Tegner *et al.*, 2019), or that CFBs may be sourced in accumulations at mid-mantle phase transitions of foundered and subducted sediment- and subduction-modified lithosphere (e.g. Anderson, 1979; Maruyama & Okamoto, 2007; Ivanov *et al.*, 2008; Fukao *et al.*, 2009; Ivanov & Litasov, 2013; Wang *et al.*, 2016). These sediment-modified mantle domains would then either ascend and melt through decompression (Anderson & Natland, 2014; Wang *et al.*, 2016), or mix with products of rising hotter plume mantle (Kingsbury *et al.*, 2016; Kimura *et al.*, 2018). In this paper we interpret an extensive dataset of new and compiled data from over 600 rocks to unravel the processes that contributed to the genesis and evolution of the Canadian portion of the Mesozoic High Arctic Large Igneous Province continental tholeiites (HALIP, Fig. 1), informing the debate on the origin of the 'continental' signature in CFBs.

GEOLOGICAL SETTING, STRATIGRAPHIC AND AGE CONSTRAINTS

The tholeiitic magmatic rocks we discuss occur within the Sverdrup Basin in the northern Canadian Arctic Islands (Fig. 1; Balkwill, 1978; Ricketts *et al.*, 1985; Trettin, 1989; Embry & Beauchamp, 2019). The Sverdrup Basin is bound to the south and east by the cratonic Canadian Shield and overlying Paleozoic fold belts, and to the north by a horst of continental crust, the Sverdrup Rim. The area is partly underlain by Archaean cratonic basement reworked in the Proterozoic, on which was deposited a Cambrian to Early Devonian Franklinian passive margin sequence related to the breakup of Rodinia (Trettin, 1989, 1991*b*). Ellesmerian orogenesis (~400–350 Ma) and accretion of the Pearya exotic terrane (Trettin, 1987, 1991*a*, 1991*c*) were followed by Early Carboniferous (Visean) orogenic collapse and the initiation of the Sverdrup Basin (Balkwill, 1978; Estrada *et al.*, 2018; Embry & Beauchamp, 2019). Active rifting ceased in the Early Permian, and the Sverdrup Basin then acted as a sag basin, filled by mostly siliciclastic sediments. Widespread uplift and erosion occurred with the onset of rifting in the latest Triassic (Hadlari *et al.*, 2016). Subsequent shelf and fluvio-deltaic deposition in the Sverdrup Basin continued until a latest Valanginian phase of tectonic uplift (Embry, 1991) that is interpreted to coincide with the beginning of seafloor spreading in the Amerasia Basin (Grantz *et al.*, 2011).

Renewed Early Cretaceous extension in the Sverdrup Basin (Phase 6 of Embry & Beauchamp, 2019)

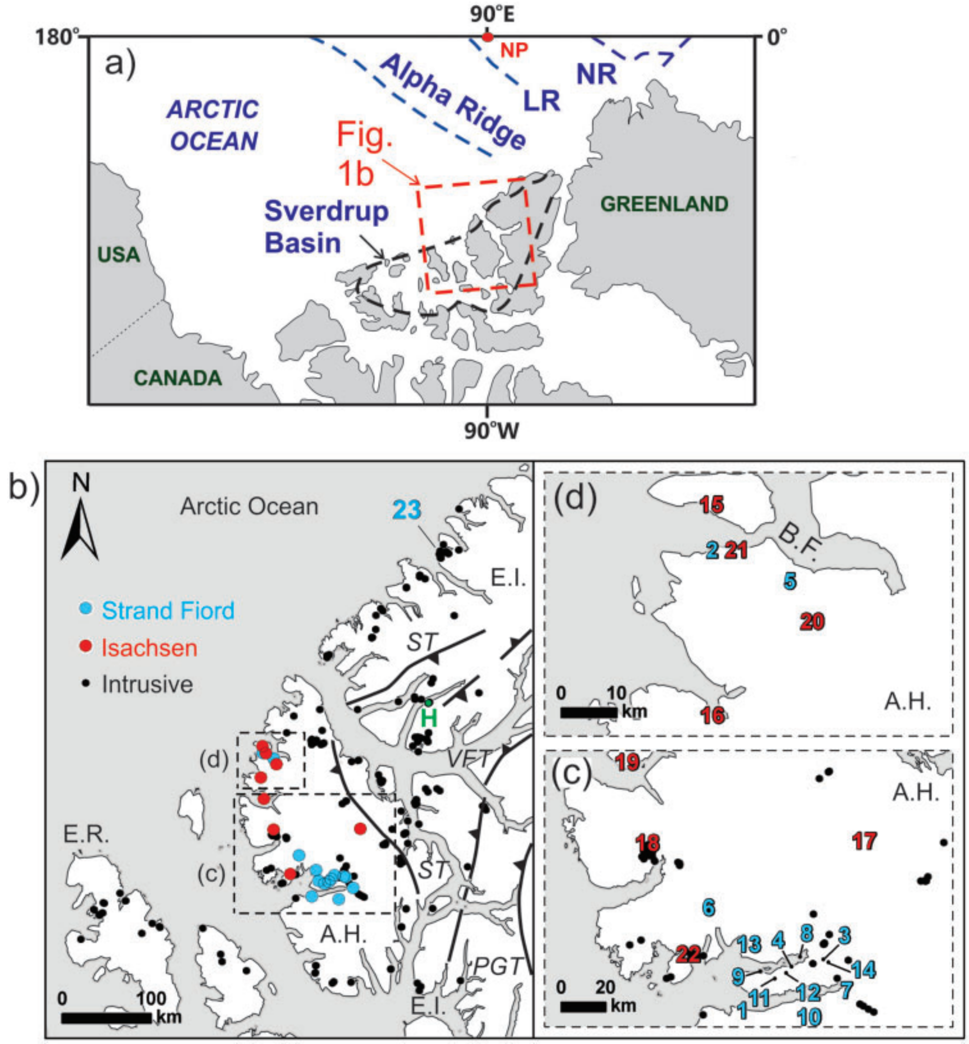

Fig. 1. (a) Polar projection of Arctic Ocean Basin. LR, Lomonosov Ridge; NR, Nansen Ridge; NP, North Pole. Red box is outline of (b). Subsequent panels use a NAD1983 UTM Zone 15N Lambert conformal conic projection. (b–d) Maps showing intrusive samples (black dots) and main tholeiitic volcanic occurrences (numbers). Strand Fiord Formation volcanic sections in blue : 1, Amarok River; 2, Arthaber Creek; 3, Bastion Ridge; 4, Camp Ridge; 5, Celluloid Creek; 6, East Fiord; 7, East Glacier Fiord Syncline; 8, Erratics Island; 9, Index Ridge; 10, South; 11, Split Mountain; 12, North; 13, Twisted Ridge; 14, West Castle Mountain; 23, Hansen Point Volcanic Complex. Isachsen Formation volcanic sections in red: 15, Bjarnason Island; 16, Camp 5 Creek; 17, Geodetic Hills; 18, Middle Fiord; 19, Bals Fiord; 20, Paterson Island; 21, Scree Ridge; 22, Cuesta Ridge. The green dot marked by a green H is the location of the Hare Sill. *ST*, Stolz Thrust; *VFT*, Vesle Fiord–East Cape Thrust; *PGT*, Parrish Glacier Thrust. E.I., Ellesmere Island; A.H., Axel Heiberg Island; E.R., Ellef Ringnes Island; B.F., Bunde Fiord. Supplementary Data Fig. S1 shows distribution of different tholeiitic types and series.

saw deposition of coarse-grained, fluvial or deltaic sediments and a first pulse of exclusively tholeiitic HALIP continental basaltic volcanism (the Isachsen Fm., 135–120 Ma; Embry & Osadetz, 1988). HALIP magmatism was possibly related to arrival of a mantle plume that may also have created the 30 km thick Alpha–Mendeleev Ridge (Embry & Osadetz, 1988; Maher, 2001; Tegner *et al.*, 2011; Døssing *et al.*, 2013; Chernykh *et al.*, 2018) whilst generating giant radial and circumferential dyke swarms (Buchan & Ernst, 2006, 2018). As an alternative to a plume interpretation for HALIP rifting and magmatism, Hadlari *et al.* (2014, 2018) and Shephard *et al.* (2016), interpreted the area as a broad, long-lived, intra-continental rift zone in a distal back-arc setting, generated through eastward subduction beneath Pangea during the Triassic.

After another phase of widespread uplift in latest Albian time, the Sverdrup Basin experienced renewed subsidence and transgression in the earliest Cenomanian (earliest Late Cretaceous; Phase 7 of Embry & Beauchamp, 2019) with deposition of shallow marine to delta plain deposits and renewed eruption of tholeiitic basalts of the Strand Fiord Formation (105–90 Ma; Embry & Osadetz, 1988; Evenchick *et al.*, 2015; Dostal & MacRae, 2018; Kingsbury *et al.*, 2018), synchronous with cessation of seafloor spreading in the Amerasia Basin to the north (Embry & Beauchamp, 2019). Age data on dykes and sills and stratigraphic constraints show that intermittent basaltic magmatism spanned the apparent gap in volcanism, however, implying that the area was continuously magmatically active for about 50 Myr (Estrada & Henjes-Kunst, 2013; Evenchick *et al.*, 2015; Dockman *et al.*, 2018; Naber *et al.*, 2021). Small volumes of transitional-alkaline to alkaline HALIP lavas and intrusions of the Hassel Formation and Fulmar Suite are coeval with the Strand Fiord Formation (Osadetz & Moore, 1988; Estrada, 2015; Bédard *et al.*, 2021). Younger, more strongly alkaline lavas and associated intrusions of the Audhild Bay Suite (ABS, previously referred to as the Hansen Point Volcanics: Naber *et al.*, 2021) were emplaced along the northern coast of Ellesmere Island, and alkaline magmatism continued until ~80 Ma (Trettin & Parrish, 1987; Dewing & Embry, 2007; Tegner *et al.*, 2011; Estrada & Henjes-Kunst, 2013; Dockman *et al.*, 2018). Alkaline HALIP magmatism is dicussed more extensively in the companion paper (Bédard *et al.*, 2021). Post-HALIP horizontal shortening of Paleozoic and Mesozoic strata related to the Eurekan Orogeny began in earliest Paleocene (Thorsteinsson & Tozer 1970; Piepjohn *et al.*, 2007, 2016; Piepjohn & von Gosen, 2018 ; Ruppel *et al.*, 2018).

Basaltic lavas in the lower Isachsen Formation (Paterson Island Member; 135–130 Ma) are sparsely preserved. A single 10·5 m flow is exposed in the Geodetic Hills (17 in Fig. 1c; Embry & Osadetz, 1988), and there are occurrences on Ellef Ringnes (Evenchick *et al.*, 2015) and Bjarnason islands (15 in Fig. 1c; Embry & Osadetz, 1988; Saumur & Williamson, 2016). Pillowed to massive flows are more widespread in the upper Isachsen Formation (Walker Island Member; 127–120 Ma; Dockman *et al.*, 2018), and form thicker accumulations, with up to 300 m preserved at Bunde Fiord (B.F. in Fig. 1d; Embry & Osadetz, 1988; Williamson *et al.*, 2017; Dostal & MacRae, 2018). The thickest and most widespread volcanic manifestations of the HALIP are the Strand Fiord Formation basalts (105–90 Ma; Embry & Osadetz, 1988; Dockman *et al.*, 2018). Thorsteinsson (1971), Ricketts *et al.* (1985) and Embry & Osadetz (1988) documented a maximum thickness (789 m) of the Strand Fiord Formation in northern Axel Heiberg Island at Bunde Fiord (B.F. in Fig. 1d), and Dostal & MacRae (2018) measured and sampled a section over 700 m thick at East Fiord (6 in Fig. 1b). The volcanology of the extrusive sequences has been discussed elsewhere (Williamson *et al.*, 2016; Dostal & MacRae, 2018), but the extrusive chemo-stratigraphy is briefly considered where measured volcanic sections inform the discussion with respect to processes active within the HALIP magmatic plumbing system.

GEOCHEMISTRY

Samples, classification, petrology

Our interpretations are based on 328 new whole-rock major and trace element analyses, and five new Sr–Nd isotopic analyses, which are integrated with literature analyses on 281 rocks. New data were generated as part of the GEM2 Program of the Geological Survey of Canada on samples collected between 2013 and 2017; on rocks recovered from the archives of the Geological Survey of Canada and Dalhousie University in Halifax (Saumur, 2015; Saumur *et al.*, 2015, 2016); and on samples collected during the 2017 CASE expedition. Of the new data, 93 analyses are provided as a spreadsheet in the Supplementary Data, together with details about analytical procedures (Supplementary Data E, Appendices 1 and 2; supplementary data are available for downloading at http://www.petrology.oxfordjournals.org). Additional new data (235 analyses) considered here have been reported by Saumur *et al.* (2021). Representative analyses are given in Table 1. Data compiled from the literature include: Trettin (1996) $n = 4$; Estrada & Henjes-Kunst (2004, 2013) $n = 52$; Ernst & Buchan (2010) and Jowitt *et al.* (2014) $n = 32$; Estrada (2015) $n = 8$; Evenchick *et al.* (2015) $n = 8$; Estrada *et al.* (2016) $n = 22$; Kingsbury (2016), Kingsbury *et al.* (2016), and C. Kingsbury (personal communication, 2019) $n = 60$; Estrada *et al.* (2018) $n = 11$; Estrada & Piepjohn (2018) $n = 8$; Dockman *et al.* (2018) $n = 38$; Naber *et al.* (2021) $n = 11$. The complete HALIP dataset (new and compiled, including available metadata and coordinates) has been reported by Bédard *et al.* (2020).

Locations of sub-alkaline basaltic samples treated here (both new and compiled) are shown in Fig. 1 and Supplementary Data Fig. S1. In this paper, major element weight per cent values (wt%) are always given and are plotted volatile-free. Although treated with caution, even altered samples are considered. Felsic magmatic rocks with MgO < 2 wt% are discussed only where they provide additional insight into petrogenesis of the mafic magmas, or where their position in the overall geochemical distribution sheds additional light on the HALIP as a whole.

We divided all HALIP subalkaline mafic rocks for which there are reliable trace element data into informal types and series. After multiple iterations we chose the Ce vs Sm/Yb_{NMORB} diagram (Fig. 2) as a binning tool to break up inchoate data into testable entities. A complete justification for this will be provided when the incompatible trace element data are presented below. All subsequent figures use these symbol and colour conventions. Symbols with dark center-dots are inferred to be mafic cumulates. Older trace element data were excluded from consideration.

The Zr/Ti vs Nb/Y (Fig. 3) and total alkalis vs silica (TAS, $Na_2O + K_2O$ vs SiO_2, Supplementary Data Fig. S2) diagrams were used to classify samples and yielded generally consistent results. Occasional misfits in the TAS diagram probably reflect post-magmatic remobilization of alkalis and silica (Pearce, 2008, 2014) and strongly anomalous values were excluded from the averaging (Table 2). Subalkaline HALIP rocks are mostly classified as basalts with lesser basaltic andesite and andesite (Fig. 3), and many could be described as icelandites. For simplicity we call them all basalts *(sensu*

Table 1: Representative HALIP basalts

	Low-Sm/Yb			Low-intermediate Sm/Yb			
Series:	a–b–c	a–b–c	a–b–c	d–e–f–g	d–e–f–g	d–e–f–g	d–e–f–g
Type:	a	b	c	d	e	f	g
Sub-suite sample:	15JHB016A	15JHB030A	17C140	GQA16-12A	15JHB056C	15JHB020A	15WJA-B008-B1
Major + traces:	Actlabs	Actlabs	Acme	INRS-ETE	Actlabs	Actlabs	OGS
Rock:	dyke core	sill	dyke	dyke	sill	dyke	gabbroic sill
Lat.:	79·73942	79·64623	81·72435	81·20475	81·00814	79·73300	79·41064
Long.:	–87·21549	–88·42186	–88·20760	–84·57023	–84·96038	–87·31209	–90·76605
Major elements (wt%)							
SiO_2	49·84	49·69	50·5	50·5	50·28	51·73	48·86
TiO_2	2·045	2·51	2·58	1·95	2·63	1·994	1·95
Al_2O_3	13·31	13·1	12·7	14	13·2	12·73	13·7
Fe_2O_3*	14·55	15·63	15·5	13·5	15·3	14·35	14·18
MnO	0·243	0·245	0·24	0·221	0·236	0·221	0·214
MgO	6·41	5·59	4·94	5·74	5·4	5·18	6·31
CaO	10·86	10·34	9·36	11·2	9·68	8·07	10·70
Na_2O	2·21	2·72	2·39	2·3	2·42	3·11	2·51
K_2O	0·52	0·61	0·99	0·46	0·56	0·84	0·49
P_2O_5	0·21	0·28	0·3	0·174	0·25	0·29	0·189
LOI	0·23	<0·09	0·82	0·40	0·5	1·46	1·06
Sum	100·43	100·72	100·32	100·45	100·39	99·98	100·16
S	0·03	0·004	b.d.l.	0·021	0·063	0·017	0·079
Trace elements (ppm)							
S	300	43	b.d.l.	210	630	170	790
Cs	0·9	0·8	1·2	0·64	1·5	0·8	1·23
Rb	16	16	39·5	16·4	19	28	43·5
Ba	111	135	169	65·2	191	266	306
Th	1·38	1·77	3·7	1·2	1·97	3·2	5·33
U	0·41	0·5	1·1	0·37	0·55	0·79	1·42
Nb	7·7	12·6	15·2	10·6	10·7	14·7	36·6
Ta	0·43	0·89	1·2	0·653	0·67	0·85	2·36
La	10·6	15	21·2	13·3	14·6	23	35·6
Ce	25·9	35·2	47·7	26·8	36·1	52	77·4
Pr	3·66	4·86	6·26	4·29	4·84	6·79	11·1
Sr	165	210	228·3	234	238	232	383
Pb	<5	<5	1·2	1·7	<5	<5	6
Nd	16·9	21·7	27·6	17·5	23·1	28·9	50·5
Sm	4·89	6·03	7·34	4·75	6·36	7·42	13·0
Zr	145	182	218	128	190	228	406
Hf	3·5	3·9	5·7	3·16	4·3	5·2	10·53
Eu	1·78	1·91	2·12	1·67	2·2	2·28	3·88
Gd	6·08	6·8	8·43	5·47	7·85	7·85	15·3
Tb	1·05	1·17	1·43	0·93	1·27	1·29	2·42
Dy	6·9	7·25	8·88	6·08	7·31	7·96	15·41
Y	37·2	38·4	50·4	33·5	39·8	40·4	83·2
Ho	1·4	1·43	1·88	1·24	1·46	1·56	3·09
Er	3·91	4·01	5·37	3·37	4·01	4·43	8·94
Tm	0·575	0·562	0·76	0·522	0·552	0·64	1·26
Yb	3·71	3·89	4·93	2·94	3·5	4·07	7·88
Lu	0·563	0·572	0·74	0·453	0·524	0·613	1·17
Ga	20	21	19·3	16·4	22	20	41·7
Cr	210	40	67	141	70	70	150
Ni	90	50	15·9	81	40	60	105
Cu	260	220	267·4	198	250	160	379
Zn	190	160	85	108	140	140	252
Co	46	47	47	48·2	46	44	90
Sc	43	42	n.a.	39·3	39	34	>63
V	400	385	438	371	408	336	345
W	<0·5	<0·5	n.a.	0·73	<0·5	<0·5	0·79
Bi	<0·1	<0·1	n.a.	0·051	<0·1	<0·1	<0·47
As	<5	<5	n.a.	3·1	<5	<5	n.a.
Mo	<2	<2	0·5	0·69	<2	<2	2·55
Ag	<0·5	0·5	n.a.	0·146	<0·5	0·6	n.a.
In	<0·1	0·1	n.a.	0·093	0·1	<0·1	0·2124
Sn	1	2	2	1·44	1	2	4
Sb	<0·2	<0·2	n.a.	1·2	<0·2	<0·2	0·16
Te	n.a.	Na	n.a.	<0·12	n.a.	n.a.	n.a.
Cd	n.a.	Na	n.a.	<0·8	n.a.	n.a.	0·261
Li	n.a.	Na	n.a.	n.a.	n.a.	n.a.	23·8
Be	1	1	n.a.	n.a.	1	2	2·6
Ge	1·5	1·5	n.a.	n.a.	1·4	1·4	n.a.

(continued)

Table 1: Continued

	Low-Sm/Yb			Low-intermediate Sm/Yb			
Tl	<0·05	<0·05	n.a.	n.a.	0·1	<0·05	0·187
$^{147}Sm/^{144}Nd$	0·1749327				0·1664539		
$^{143}Nd/^{144}Nd$	0·5129024				0·5128818		
±	0·0000072				0·0000066		
$^{145}Nd/^{155}Nd$	0·3484104				0·3484084		
±	0·0000054				0·0000049		
εNd(90 Ma)-CHUR	5·4083969				5·1042866		
$^{87}Rb/^{86}Sr$	0·2805205				0·2309493		
$^{87}Sr/^{86}Sr$	0·7057244				0·7059943		
±	0·000007				0·000008		
$^{87}Sr/^{88}Sr$	0·119796				0·1200253		
Sr_i	0·7053417				0·7056793		

	High-intermediate Sm/Yb				High-Sm/Yb		Very High-Sm/Yb
Series:	k–l–m	k–l–m	k–l–m	p–q–r	p–q–r	p–q–r	w–u
Type:	k	l	m	p	q	r	w
Sub-suite aample:	15JHB035A	15JHB028A	17C99	17C2	15JHB032A	15JHB047A	15JHB015A
Major + traces:	Actlabs	Actlabs	Acme	Acme	Actlabs	Actlabs	Actlabs
Rock:	sill	sill core	dyke	dyke core	sill core	sill core	sill core
Lat.:	80·677824	79·640579	82·292510	81·835652	80·687144	81·055831	79·739421
Long.:	–85·782753	–88·424387	–84·234125	–82·271888	–85·898456	–85·350818	–87·215516
Major elements (wt%)							
SiO_2	48·22	49·1	53·3	49·7	50·91	49·36	48·34
TiO_2	2·77	2·994	2·46	2·76	2·625	3·055	4·004
Al_2O_3	12·67	12·73	13·1	13·7	13·22	12·71	12·82
$Fe_2O_3^*$	15·93	15·88	12·9	13·6	14·98	16·02	14·65
MnO	0·2	0·23	0·21	0·2	0·213	0·257	0·201
MgO	4·79	4·98	3·94	6·21	4·91	4·11	4·48
CaO	7·94	8·64	7·17	10·2	9·02	8·43	8·52
Na_2O	3·14	2·88	3	2·51	2·65	2·53	3·01
K_2O	1·22	1·09	1·79	0·42	1·08	1·29	0·68
P_2O_5	0·24	0·26	0·3	0·26	0·31	1·11	0·56
LOI	2·16	1·21	1·27	<0·02	0·73	1·22	2·09
Sum	99·28	99·99	99·44	99·56	100·65	100·09	99·36
S	0·1715	0·12	b.d.l.	b.d.l.	0·06	0·17	0·177
Trace elements (ppm)							
S	1715	1200	b.d.l.	b.d.l.	600	1700	1770
Cs	0·5	1	1	0·5	2	3·9	0·3
Rb	44	35	70·4	9·7	38	40	14
Ba	314	403	305	71	300	469	163
Th	2·19	3·04	6·9	1·2	4·38	5·85	2·55
U	0·63	0·77	1·7	0·3	1·13	1·36	0·8
Nb	9·7	13·7	27·3	10	16·5	21·5	18·8
Ta	0·69	1·03	1·8	0·7	1·31	1·58	1·27
La	15·5	19·6	37·2	12·6	26·7	49·1	24·2
Ce	36·5	46	78·8	30·8	60·1	109	60·4
Pr	4·87	6·01	9·83	4·68	7·63	14	8·53
Sr	519	283	281·3	300·5	272	318	371
Pb	<5	<5	4·3	1·8	<5	<5	<5
Nd	21·9	25·4	40·9	22·8	32·8	57·5	38·8
Sm	5·93	6·67	9·22	6·31	8·4	13·6	9·9
Zr	163	201	303	174	243	406	287
Hf	3·8	4·3	8	4·6	5·4	8·1	6·6
Eu	2·04	2·11	2·57	2·1	2·35	4·12	3·31
Gd	6·29	7·17	10·28	6·97	8·42	13·2	10·5
Tb	1·06	1·13	1·59	1·07	1·38	2	1·6
Dy	6·41	6·92	9·73	6·4	8·37	12	9·31
Y	33	36	52·5	33·1	42·1	60·2	45·7
Ho	1·22	1·36	1·91	1·22	1·62	2·21	1·72
Er	3·43	3·7	5·61	3·29	4·62	6·3	4·47
Tm	0·483	0·514	0·74	0·44	0·638	0·831	0·615
Yb	3·08	3·43	4·79	2·63	3·93	5·51	3·89
Lu	0·469	0·511	0·73	0·39	0·605	0·81	0·561
Ga	22	21	22·4	20·7	21	21	24
Cr	20	40	67	134	40	30	<20
Ni	50	60	15	27·8	50	30	40
Cu	220	230	50·4	189·8	200	50	150
Zn	130	130	83	36	150	180	140
Co	46	45	39·3	46·6	42	32	39

(continued)

Table 1: Continued

	High-intermediate Sm/Yb				High-Sm/Yb		Very High-Sm/Yb
Sc	35	37	n.a.	n.a.	35	36	29
V	543	548	337	408	373	204	426
W	<0·5	<0·5	n.a.	n.a.	<0·5	<0·5	<0·5
Bi	<0·1	<0·1	n.a.	n.a.	<0·1	<0·1	<0·1
As	<5	<5	n.a.	n.a.	<5	<5	<5
Mo	<2	<2	0·6	0·3	<2	<2	<2
Ag	<0·5	0·8	n.a.	n.a.	0·7	1·4	0·9
In	<0·1	0·1	n.a.	n.a.	0·1	0·1	0·1
Sn	1	2	17	1	2	2	2
Sb	<0·2	<0·2	n.a.	n.a.	<0·2	<0·2	<0·2
Te	n.a.	n.a.	n.a.	n.a.	n.a.	n.a.	n.a.
Cd	n.a.	n.a.	n.a.	n.a.	n.a.	n.a.	n.a.
Li	n.a.	n.a.	n.a.	n.a.	n.a.	n.a.	n.a.
Be	1	2	n.a.	n.a.	2	2	2
Ge	1·6	1·4	n.a.	n.a.	1·6	1·5	1·6
Tl	0·13	<0·05	n.a.	n.a.	0·1	0·1	<0·05
$^{147}Sm/^{144}Nd$						0·1429947	
$^{143}Nd/^{144}Nd$						0·5126510	
±						0·0000060	
$^{145}Nd/^{155}Nd$						0·3484064	
±						0·0000040	
εNd(90 Ma)-CHUR						0·8700293	
$^{87}Rb/^{86}Sr$						0·3639509	
$^{87}Sr/^{86}Sr$						0·7076384	
±						0·000007	
$^{87}Sr/^{88}Sr$						0·1198164	
Sr_i						0·7071419	

*All iron as Fe_2O_3.

LOI, loss on ignition. n.d., not determined; b.d.l., below detection limit. (See Electronic Data Appendices 1 and 2 for other analyses and methods.) INRS-ETE is the Institut National de la Recherce Scientifique - Eau, Terre et Environnement laboratory in Québec City.

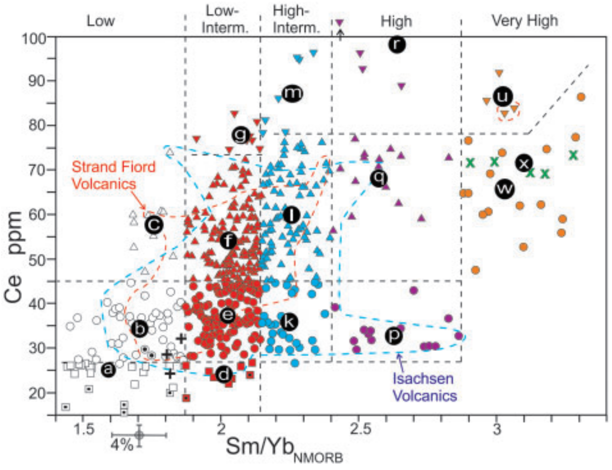

Fig. 2. Ce (ppm) vs Sm/Yb_{NMORB} (normalized to N-MORB, Sm = 2·63 ppm, Yb = 3·05 ppm from Sun & McDonough, 1989) for HALIP tholeiites (see Fig. 3 for a more detailed symbol key). Labelled divisions along upper axis refer to Sm/Yb_{NMORB} groupings discussed below. Dashed black lines delimit the types and series. White letters in black circles show type averages. Type x are within the w field but have different trace element profiles (see below). Dashed red and blue lines show range of volcanic rocks from the Strand Fiord and Isachsen Formations, respectively. Symbols do not discriminate between volcanic and intrusive samples. (See text for discussion of the rationale of division.)

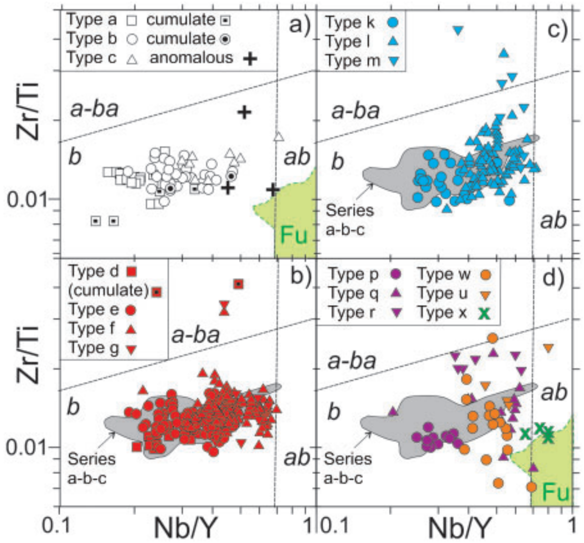

Fig. 3. Zr/Ti vs Nb/Y discriminant of Pearce (2014; after Winchester & Floyd, 1977) for sub-alkaline HALIP rocks. The basalt–alkali basalt transition is at Nb/Y ~ 0·7. (a) Types a–b–c; (b) Types d–e–f–g; (c) Types k–l–m; (d) Types p–q–r and w–u–x. Green field marked Fu indicates Fulmar Suite HALIP alkaline rocks (Bédard *et al.*, 2021). Grey field shows distribution of basalt Types a–b–c from (a). *b*, basalt; *a-ba*; andesite–basaltic andesite; *ab*, alkali-basalt. HALIP basaltic types and series are defined graphically in Fig. 2. In (a), the + symbols correspond to three samples from Dockman *et al.* (2018) that fall in the Type a bin of Fig. 2, but that have unusual trace element profiles (see Supplementary Data Fig. S3d). Misfits between this plot and the TAS diagram (Supplementary Data Fig. S2) probably reflect overprinting alteration and remobilization of alkalis and silica.

lato) henceforth. Rocks straddling the subalkaline–alkaline boundary (Fig. 3 and Supplementary Data Fig. S2) are described as transitional-alkaline.

Table 2: Average of different HALIP magma types defined using criteria from Fig. 2

		Low-Sm/Yb			Low-Intermediate Sm/Yb			
Type		a	b	c	d	e	f	g
N		18	40	10	8	113	124	8
SiO2	wt%-N	50·66	50·32	50·68	50·40	50·77	50·80	50·93
TiO2	wt%-N	1·98	2·27	3·09	1·98	2·41	2·88	3·30
Al2O3	wt%-N	13·63	13·95	12·98	14·44	14·14	13·62	13·38
FeO*	wt%-N	13·24	13·71	15·03	12·16	13·51	14·44	13·82
MnO	wt%-N	0·23	0·24	0·26	0·22	0·22	0·23	0·24
MgO	wt%-N	6·39	5·37	4·16	5·70	5·19	4·46	4·26
CaO	wt%-N	10·85	10·70	9·12	12·16	10·04	9·21	8·80
Na2O	wt%-N	2·30	2·55	2·73	2·36	2·74	2·99	3·15
K2O	wt%-N	0·50	0·53	1·11	0·42	0·69	0·90	1·19
P2O5	wt%-N	0·19	0·23	0·37	0·18	0·25	0·35	0·46
LOI	wt%	1·00	2·63	2·04	3·40	2·62	2·47	2·87
S	ppm or ug/g	593	544	1425	420	1218	656	1800
Cs	ppm	1·331	2·610	1·458	1·798	0·898	1·346	1·250
K	ppm	4175	4364	9208	3475	5700	7494	9870
Rb	ppm	16·14	15·88	43·40	12·29	20·23	27·94	39·17
Ba	ppm	97	139	245	112	186	239	320
Th	ppm	1·563	2·314	4·375	1·198	2·572	4·062	5·312
U	ppm	0·429	0·614	1·163	0·373	0·665	1·049	1·304
Nb	ppm	7·24	12·14	21·94	8·00	12·61	21·62	29·83
Ta	ppm	0·435	0·841	1·684	0·449	0·926	1·489	1·915
La	ppm	10·62	15·13	26·59	11·29	16·49	24·67	35·13
Ce	ppm	25·63	34·36	58·31	24·76	37·99	54·85	78·03
Pr	ppm	3·616	4·741	7·671	3·829	5·147	7·171	10·164
Sr	ppm	177	203	219	245	243	248	277
Pb	ppm	6·91	3·85	6·84	2·60	5·54	6·56	5·04
Nd	ppm	16·96	21·40	33·01	16·94	23·66	31·63	42·51
Sm	ppm	4·865	5·670	8·153	4·731	6·100	7·757	10·07
P	ppm	810	993	1601	769	1109	1530	2002
Zr	ppm	139	162	250	119	176	229	298
Hf	ppm	3·42	4·21	6·25	3·15	4·41	5·92	7·78
Ti	ppm	11890	13619	18548	11844	14468	17289	19798
Eu	ppm	1·625	1·843	2·453	1·620	1·949	2·324	2·989
Gd	ppm	5·886	6·713	9·414	5·459	6·844	8·505	11·029
Tb	ppm	1·024	1·147	1·577	0·892	1·138	1·408	1·797
Dy	ppm	6·581	7·233	9·723	5·723	7·007	8·547	10·903
Y	ppm	36·0	39·9	53·4	31·5	37·2	45·4	58·6
Ho	ppm	1·329	1·490	2·061	1·153	1·398	1·737	2·187
Er	ppm	3·753	4·182	5·644	3·128	3·856	4·849	6·081
Tm	ppm	0·5625	0·6144	0·8553	0·4738	0·5566	0·7012	0·8920
Yb	ppm	3·547	3·886	5·405	2·731	3·496	4·413	5·657
Lu	ppm	0·5344	0·5780	0·7999	0·4111	0·5234	0·6501	0·8358
Ga	ppm	19·1	19·3	22·4	17·3	21·0	22·0	25·4
Cr	ppm	154	81	36	149	72	46	58
Ni	ppm	81	52	31·5	80	48	35·3	31·6
Cu	ppm	230	222	233	184	155	132	136
Zn	ppm	139	118	130	100	123	129	170
Co	ppm	49	49	51	46	47	47	46
Sc	ppm	42	42	38	37	36	34	36
V	ppm	389	396	436	354	371	391	392
W	ppm	77·1	10·7	74·4	1·43	16·5	21·3	1·14
Bi	ppm	–	0·354	–	0·050	0·630	0·680	0·021
As	ppm	–	4·04	4·4	3·76	3·77	5·1	1·51
Mo	ppm	0·68	0·86	1·14	0·96	1·12	1·66	2·68
Ag	ppm	0·20	0·35	0·23	0·11	3·65	10·8	0·46
In	ppm	0·096	0·098	0·132	0·089	0·095	0·151	0·147
Sn	ppm	1·16	1·90	2·95	1·79	1·82	2·46	3·24
Sb	ppm	0·92	1·14	1·62	2·29	1·36	1·01	0·49
Cd	ppm	0·66	1·57	1·20	–	0·58	0·68	0·18
F	ppm	289	437	654	–	379	711	1299
Cl	ppm	–	1·34	326	–	554	131	123
Li	ppm	30·2	14·8	–	–	16·0	13·7	21·2
Be	ppm	0·978	1·06	1·70	–	1·26	1·69	2·52
Ge	ppm	1·61	1·63	–	–	1·67	1·51	–
Tl	ppm	0·171	0·132	0·19	–	0·104	0·16	0·15

(continued)

Table 2: Continued

		High-Intermediate Sm/Yb			High-Sm/Yb			Very-High-Sm/Yb		
Type		k	l	m	p	q	r	w	u	x
N		29	89	7	14	15	6	17	4	5
SiO2	wt%-N	49·81	51·45	55·19	48·54	51·76	52·12	50·79	53·33	50·25
TiO2	wt%-N	2·50	2·95	2·55	2·91	3·21	2·98	3·90	2·87	3·79
Al2O3	wt%-N	14·35	13·42	13·66	15·04	13·53	13·21	13·22	13·79	14·01
FeO*	wt%-N	13·47	14·24	11·66	12·81	14·09	14·06	13·69	12·87	13·85
MnO	wt%-N	0·21	0·23	0·22	0·22	0·25	0·26	0·20	0·23	0·24
MgO	wt%-N	5·33	4·42	3·23	5·31	4·48	3·95	4·69	3·65	4·67
CaO	wt%-N	10·34	8·60	6·57	11·60	8·02	7·37	8·48	7·87	7·18
Na2O	wt%-N	3·03	3·04	2·96	2·74	3·29	2·94	3·50	3·41	3·22
K2O	wt%-N	0·54	1·06	2·29	0·32	0·91	1·78	0·73	1·24	1·66
P2O5	wt%-N	0·25	0·36	0·52	0·28	0·45	0·93	0·55	0·74	0·50
LOI	wt%	4·82	2·35	3·56	4·80	2·45	1·51	1·79	2·53	2·45
S	ppm	1005	1171	815	446	2041	1337	1709	1010	3680
Cs	ppm	0·954	1·406	2·136	0·552	1·519	2·195	0·809	3·765	0·528
K	ppm	4445	8785	19014	2673	7571	14747	6038	10272	13807
Rb	ppm	15·93	35·11	63·46	7·04	28·96	54·00	20·72	25·05	44·32
Ba	ppm	158	300	461	157	307	439	233	835	500
Th	ppm	2·215	4·356	7·543	1·630	4·014	5·969	3·056	4·605	5·590
U	ppm	0·582	1·119	1·860	0·416	1·051	1·433	0·842	1·230	1·378
Nb	ppm	11·41	22·30	30·28	10·51	24·95	27·07	22·73	30·63	31·58
Ta	ppm	0·751	1·522	2·017	0·732	1·733	1·752	1·604	1·948	1·895
La	ppm	15·32	27·30	40·73	13·63	31·85	44·77	27·40	37·23	31·72
Ce	ppm	36·12	60·30	87·43	34·00	69·11	99·95	65·72	86·30	71·36
Pr	ppm	4·985	7·836	10·843	4·933	9·078	12·831	9·131	11·255	8·912
Sr	ppm	261	287	233	293	346	295	380	411	340
Pb	ppm	3·77	6·48	5·97	2·17	5·68	8·54	2·23	6·80	8·50
Nd	ppm	22·892	33·978	46·090	24·180	39·693	54·180	42·431	50·893	40·200
Sm	ppm	6·092	8·097	10·327	6·487	9·196	12·249	10·581	11·585	9·318
P	ppm	1111	1561	2280	1220	1985	4067	2392	3214	2169
Zr	ppm	166	237	327	179	256	364	296	281	254
Hf	ppm	4·26	6·01	8·28	4·67	6·32	8·11	7·27	7·11	7·27
Ti	ppm	15001	17664	15253	17440	19255	17856	23368	17228	22730
Eu	ppm	1·907	2·410	2·982	2·097	2·809	3·634	3·278	3·638	2·656
Gd	ppm	6·692	8·619	10·764	6·889	9·583	12·195	11·012	11·200	9·374
Tb	ppm	1·088	1·394	1·799	1·123	1·494	1·916	1·698	1·713	1·318
Dy	ppm	6·641	8·512	10·455	6·722	8·857	11·339	9·707	9·995	7·930
Y	ppm	34·7	45·5	55·0	33·9	47·0	58·7	48·3	51·7	40·9
Ho	ppm	1·309	1·700	2·102	1·309	1·744	2·201	1·819	1·933	1·520
Er	ppm	3·573	4·717	5·906	3·443	4·596	6·133	4·665	5·135	4·030
Tm	ppm	0·5096	0·6721	0·8536	0·4660	0·6640	0·8179	0·6520	0·7633	0·5768
Yb	ppm	3·147	4·184	5·345	2·861	4·152	5·388	3·997	4·443	3·488
Lu	ppm	0·4601	0·6256	0·7823	0·4181	0·6058	0·7860	0·5789	0·6600	0·5050
Ga	ppm	20·4	22·4	23·7	20·9	23·0	21·7	23·8	25·9	28·6
Cr	ppm	92	47	54	131	44	34	62	36	46
Ni	ppm	52	32·5	16·1	59	30·5	11·9	41	21·8	25·9
Cu	ppm	154	102	58	213	99	42	145	38	51
Zn	ppm	112	132	102	96	138	174	132	210	123
Co	ppm	45	45	27	47	48	31	46	37	46
Sc	ppm	35	32	21	36	31	31	29	26	29
V	ppm	373	387	225	404	355	189	386	259	402
W	ppm	1·71	16·2	0·682	0·394	44·4	0·847	22·1	–	3·14
Bi	ppm	0·366	0·391	0·685	0·397	0·405	–	0·630	–	0·096
As	ppm	3·78	3·46	5·7	3·5	4·4	–	–	–	8·1
Mo	ppm	1·04	1·42	1·92	0·66	1·64	1·87	1·18	1·49	1·62
Ag	ppm	0·18	0·34	26·0	0·20	0·43	1·27	0·42	–	0·38
In	ppm	0·094	0·111	0·107	0·093	0·113	0·111	0·115	0·110	0·112
Sn	ppm	1·77	2·66	5·07	1·85	2·48	2·72	2·50	1·90	3·70
Sb	ppm	1·77	1·40	1·46	1·56	1·59	0·33	0·91	–	6·42
Cd	ppm	0·26	0·59	0·24	0·98	1·15	0·40	0·84	0·80	–
F	ppm	664	762	660	–	797	–	725	1258	–
Cl	ppm	205	102	170	–	385	–	368	407	–
Li	ppm	37·9	17·7	22·5	28·2	42·9	47·2	16·1	–	–
Be	ppm	1·14	1·94	3·00	0·66	2·01	2·21	2·03	2·20	–
Ge	ppm	1·31	1·47	1·35	–	1·65	1·47	1·9	–	–
Tl	ppm	0·113	0·157	0·187	0·228	0·139	0·192	0·148	0·16	–

major elements normalized to 100% volatile-free
FeO* = total iron as FeO

Older and younger pulses of HALIP mafic tholeiitic lavas are both dominated by low-MgO (<7 wt%) basalt with sparse plagioclase + clinopyroxene ± olivine phenocrysts (Dostal & MacRae, 2018; Dockman *et al.*, 2018; Naber *et al.*, 2021). Swarms of compositionally similar basaltic sills and dykes are associated with the Strand Fiord and Isachsen Formation volcanism (Saumur *et al.*, 2016, 2021), and some are interpreted as sub-volcanic feeders. These intrusions are typically fine- to medium-grained, sparsely plagioclase + clinopyroxene ± olivine-phyric dolerite. There is little layering and no evidence of extensive *in situ* differentiation in most sills and dykes. For example, 26 samples taken from the 17 m thick Hare Sill (Green H in Fig. 1b, our detailed petrological and geochemical case study) show internal variation for most elements (except Ba) within analytical error. Thicker intrusive bodies develop coarser gabbroic cores that may contain subordinate pigeonite, orthopyroxene, Fe–Ti-oxides, and minor interstitial hornblende, sulphides, biotite, quartz and apatite. The scarcity of hornblende and biotite imply low magmatic water contents. Alteration is typically minor, with rare exceptions. Subalkaline HALIP lavas and intrusions show near-complete compositional overlap, although the intrusions have a slightly larger compositional range (Fig. 2). As pointed out previously (Estrada *et al.*, 2016; Dostal & MacRae, 2018), the close similarity in composition between Isachsen and Strand Fiord basalts (Fig. 2) makes it impossible to correlate most undated sills or dykes to either formation based on geochemistry alone. For this reason intrusive and extrusive rock data are interpreted together using an age-blind geochemical approach, with stratigraphic and geochronological constraints being brought in later.

Major and minor elements

HALIP tholeiites have low MgO (<7 wt%), Ni and Cr (Tables 1 and 2), and define a diffuse tholeiitic trend of FeO*–TiO_2–P_2O_5 enrichment (Fig. 4), and of Al_2O_3 and CaO depletion (Figs 5 and 6) as MgO decreases, that approximately follows plagioclase + clinopyroxene ± olivine cotectics (see Estrada, 2015; Kingsbury *et al.*, 2016; Dockman *et al.*, 2018; Dostal & MacRae, 2018). However, HALIP data show a steeper FeO*–TiO_2–P_2O_5 enrichment trend than any individual model liquid line of descent (LLD, Fig. 4). HALIP tholeiites show a range of TiO_2 and P_2O_5 at a given MgO content (Fig. 4b and c), with higher-Sm/Yb series rocks ranging to the highest TiO_2 and P_2O_5 contents. Below 3–4% MgO, values of FeO*, TiO_2, Sc and V generally decrease (Figs 4–6), except for a subset of low-MgO rocks that have unusually high Al_2O_3–CaO–Sr§ [Figs 5–7, Sr§ = Sr_N – (Pr_N + Nd_N)/2, where subscript N indicates concentration in N-MORB], and that also show marked relative enrichment in Sc, V, Co, Cr and Ni (Figs 8 and 9; Tables 1 and 2). Most HALIP basalts show a clear decrease of Al_2O_3, Sr§ and Eu/Eu* with decreasing MgO

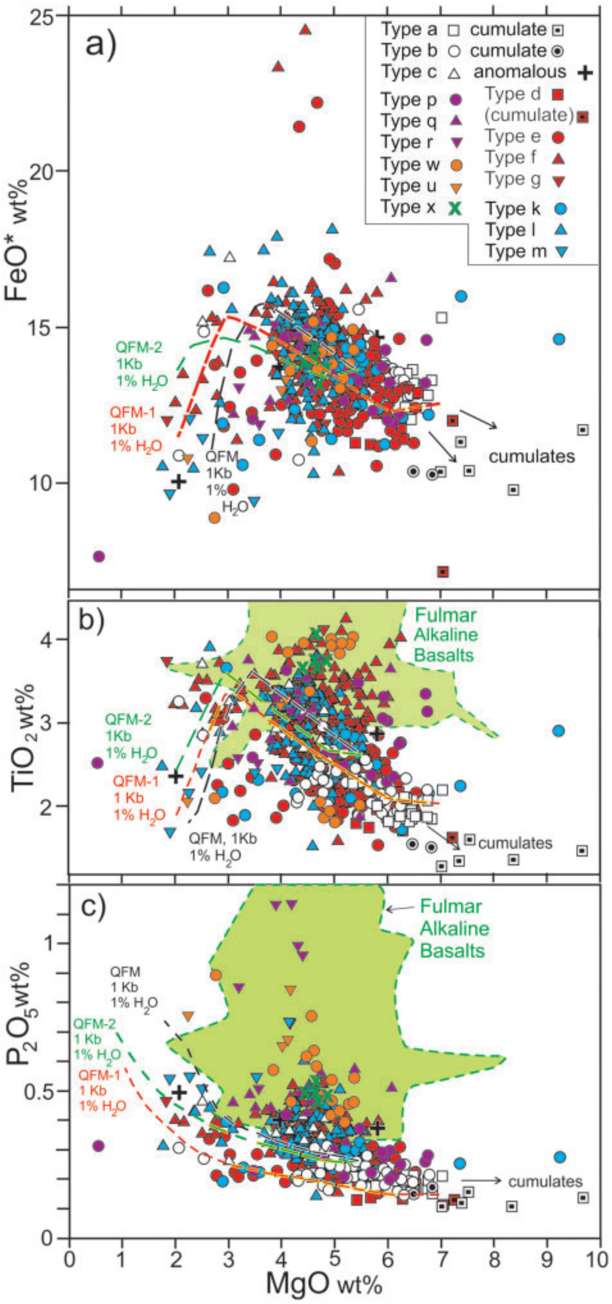

Fig. 4. (a) FeO*, (b) TiO_2 and (c) P_2O_5 vs MgO wt% (normalized volatile-free). FeO* is all iron as FeO. Curves are PELE (Boudreau, 1999) pure fractional crystallization models showing the liquid line of descent (LLD) at different values of pressure, water content and fO_2 (relative to the quartz–fayalite–magnetite buffer; QFM) applied to two parental melt compositions: an average of the most primitive HALIP basalts with 7 wt% MgO, and the average ($n = 26$) of the Hare Sill with 5·5 wt% MgO. The overall HALIP data trend is steeper than predicted by any individual LLD, and the range of TiO_2 and P_2O_5 exceeds what could result from varying crystallization conditions. Symbols with center dot represent probable mafic cumulate facies enriched in olivine, clinopyroxene and plagioclase. Green field delimits range of Fulmar Suite alkaline rocks (Bédard *et al.*, 2021) that overlaps with Types p, w and x. The very low-MgO p-type samples in this and subsequent figures are strongly altered and lost MgO, FeO* and CaO.

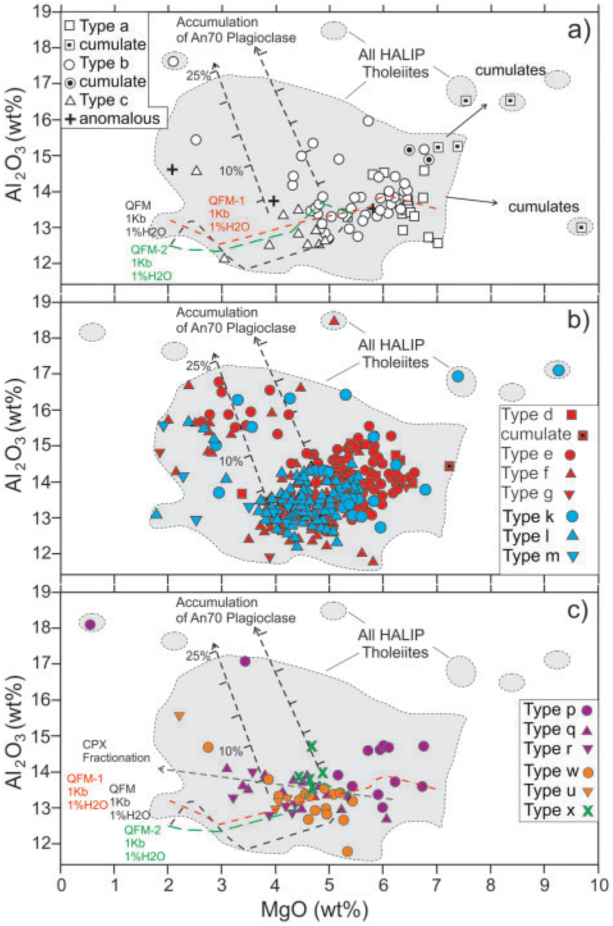

Fig. 5. Al_2O_3 vs MgO wt%: (a) Types a–b–c; (b) Types d–e–f–g and k–l–m; (c) Types p–q–r and w–u–x. Rocks showing Al_2O_3 enrichment are interpreted to have accumulated plagioclase. Higher-Sm/Yb_{NMORB} rocks (c) trend closer to a clinopyroxene (Cpx) dominated fractionation trend. Other comments as for Fig. 4.

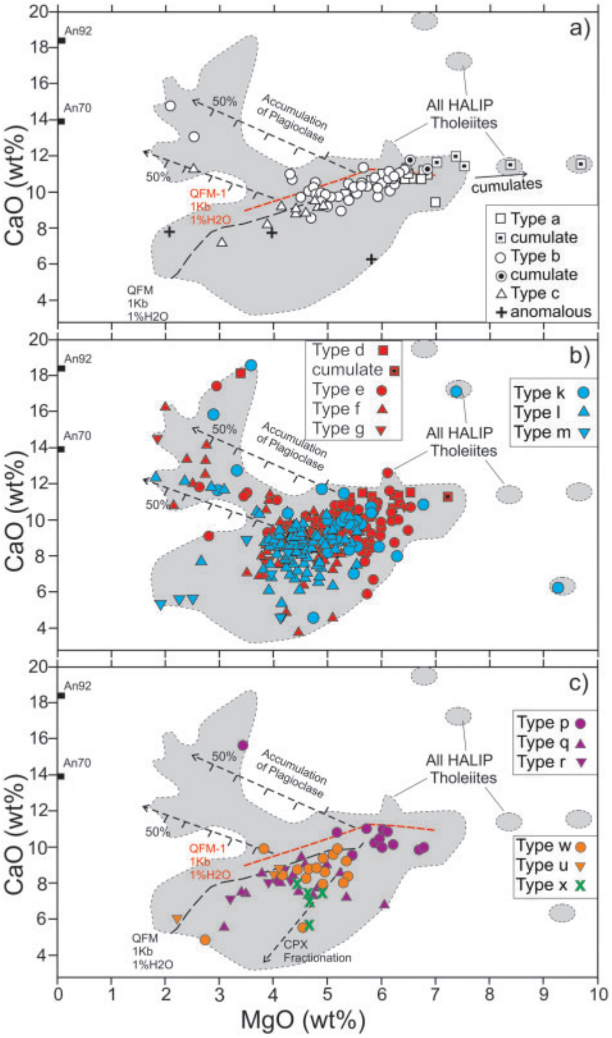

Fig. 6. CaO vs MgO wt%. Rocks showing CaO enrichment are interpreted to have accumulated plagioclase. The positions of end-member An_{70} and An_{92} plagioclase are indicated. Higher-Sm/Yb rocks (c) show a steeper evolution trend, suggesting a greater role for clinopyroxene fractionation. Other comments as for Fig. 4.

[Figs 5 and 7, Eu* = $\sqrt{(Sm_N \times Gd_N)}$, where subscript N indicates concentration in chondrite]. However, the higher-Sm/Yb tholeiite population (Types p–q–r and w–u–x) differs slightly in showing trends of CaO–Sc depletion (Figs 6c and 8c), slight Al_2O_3 enrichment (Fig. 5c), and a shallow decrease of Sr§ with decreasing MgO (Fig. 7c). Some intermediate-Sm/Yb tholeiites (Type d–e–f–g and k–l–m rocks) also show the latter trends (Figs 6b–8b).

Trace element data

The major element data for HALIP basalts show considerable dispersion, and are difficult to explain without considering trace element data (Figs 10–13), which we now use to define representative populations of HALIP basalts amenable to quantitative testing of petrogenetic mechanisms.

Rationale for division of HALIP tholeiites into types and series

We divided all HALIP subalkaline mafic rocks into 16 informal types and six series using the Ce vs Sm/Yb_{NMORB} diagram (Fig. 2), placing divisions at natural data minima where possible. Rocks from each type that we believe approximate liquid compositions were averaged (Table 2 and Supplementary Data Table S1), and will be used as model parents and daughters to test genetic relationships. The Ce vs Sm/Yb_{NMORB} plot was used as a binning tool because the ratio of Sm/Yb (or middle to heavy rare earth elements, MREE/HREE) is particularly sensitive to the depth-dependent mineralogy of the residual mantle from which its parental magmas separated (Gast, 1968; Lassiter & DePaolo, 1997; Dockman *et al.*, 2018), whereas abundances of highly incompatible elements such as Ce can reflect the degree of source enrichment, the degree of melting, the amount of subsequent crystallization, the amount of crustal contamination, and possible mixing or replenishment events in the crustal plumbing system. Grouping HALIP rocks in this way (Fig. 2) allows us to

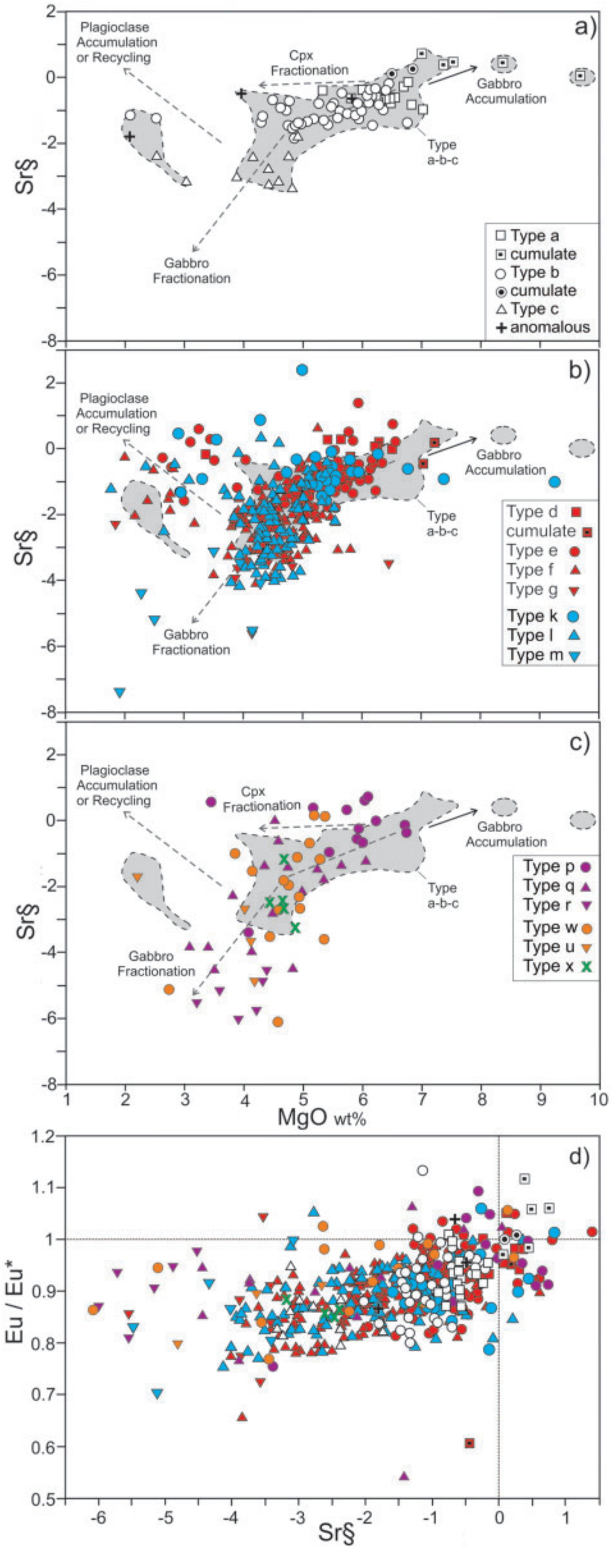

Fig. 7. (a–c) Sr§ vs MgO wt%. Sr§ = $Sr_N - (Pr_N + Nd_N)/2$, where subscript N indicates concentration in N-MORB. Sr§ measures the size of the Sr anomaly in N-MORB-normalized plots. Even Very High-Sm/Yb_{NMORB} tholeiites show progressive Sr§ decrease, implying plagioclase fractionation. Some low-MgO samples have anomalously high Sr§, suggesting plagioclase accumulation. (d) Eu/Eu* vs Sr§. Eu* = $\sqrt{(Sm_N \times Gd_N)}$, where subscript N indicates concentration in chondrite from Sun & McDonough (1989).

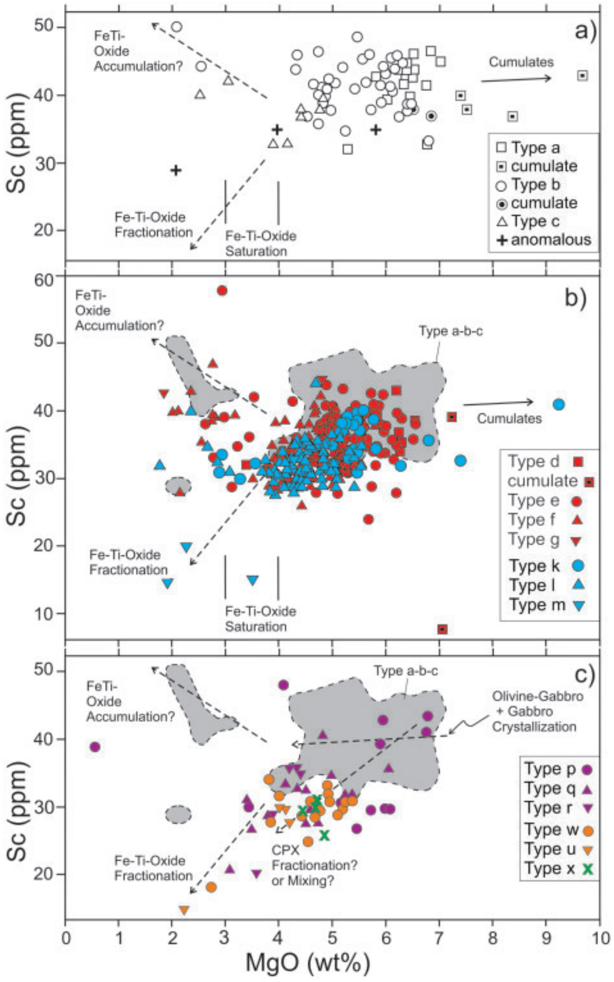

Fig. 8. Sc (ppm) vs MgO (wt%). Some low-MgO samples have anomalously high Sc. As plagioclase does not have high ^{Sc}D, this implies accumulation of a phase with high ^{Sc}D, probably an Fe–Ti-oxide mineral. We infer that saturation in Fe–Ti-oxide occurred between 3 and 4 % MgO based on position of inflection points and PELE modeling (Fig. 4b). Other low-MgO samples show decreases in Sc, suggesting fractionation of a high-^{Sc}D phase. Same comments as for Figs 4–7.

compare magmas with similar levels of enrichment in Ce but different Sm/Yb ratios to gauge the plausibility of depth of melting as a source of geochemical variation; whereas comparison of magmas with similar Sm/Yb ratios but varying Ce contents allows us to weigh the different possible mechanisms of incompatible element enrichment. The distinct distribution of HALIP rocks classed in this way in the diagrams we present in this paper confirms that our approach captures petrogenetically significant differences. Figure 10 shows a representative set of normalized incompatible element profiles for Types a, b and c (Series a–b–c). Complete sets of normalized profiles for all HALIP basalt types and series are shown in Supplementary Data Figs S3–S7. Figures 11 and 12 show the different type averages for each proposed HALIP tholeiitic differentiation series, which are compared with other CFB suites in Fig. 13. The large Pb peaks will not be considered quantitatively

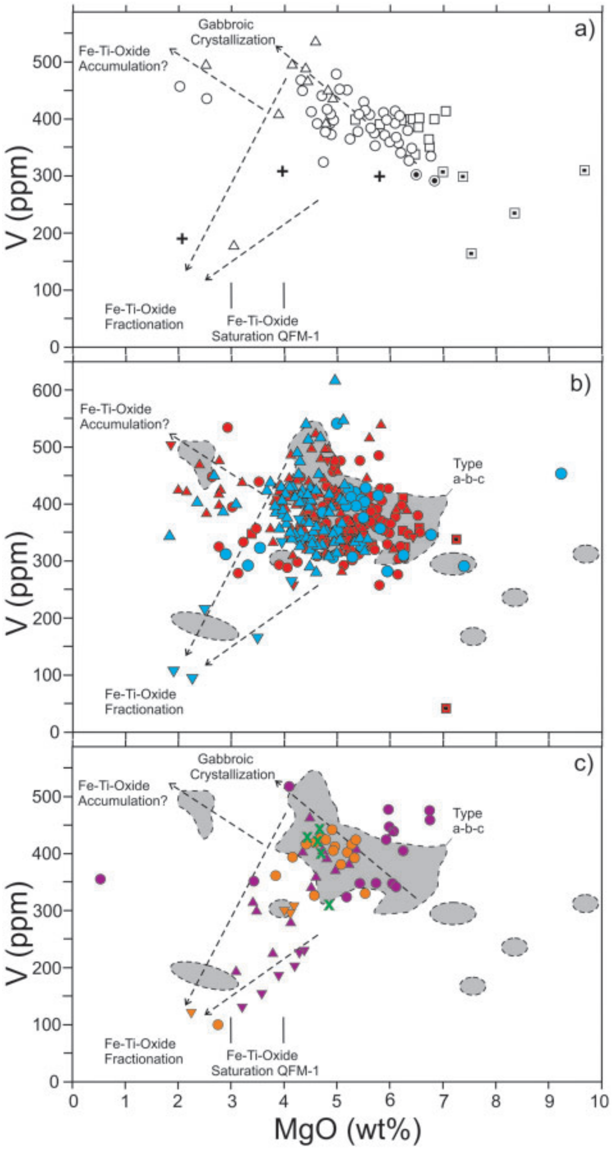

Fig. 9. V (ppm) vs MgO (wt%). Some low-MgO samples have anomalously high V, suggesting accumulation of a high-^{V}D phase, probably an Fe–Ti-oxide mineral. Same comments and legend as for Fig. 8.

in the following discussion, as HALIP basalts are hosted by Pb-rich sedimentary rocks, and Pb is notoriously mobile.

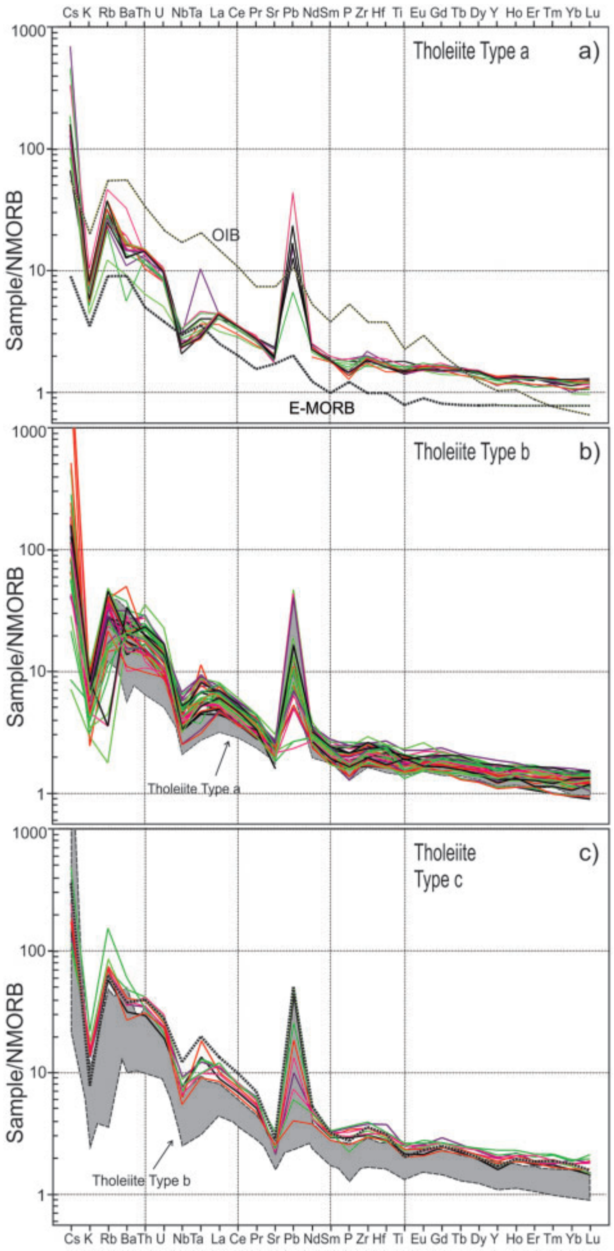

Fig. 10. Normalized incompatible element profile plots of Low-Sm/Yb$_{NMORB}$ HALIP tholeiitic basalts. (a) Type a; (b) Type b; (c) Type c. Data normalized to N-MORB of Sun & McDonough (1989) except for Rb = 1·6 ppm and Nb = 2·8 ppm (Viereck *et al.*, 1989), and K = 596 ppm (Jochum *et al.*, 1983). Other OIB, E-MORB and N-MORB data are from Sun & McDonough (1989) throughout this paper.

Low-Sm/Yb tholeiites of the a–b–c Series

Type a ($n = 23$) rocks occurs only as undated intrusive rocks. Among sub-alkaline HALIP non-cumulate mafic rocks, Type a have the lowest incompatible element abundances (Ce $<$ 0·55 ppm, Figs 2 and 10a, Tables 1 and 2), the highest concentrations of MgO (av. 6·39 wt%, Figs 4–9), Cr and Ni (Tables 1 and 2), and together with Type b have the shallowest slopes for normalized HREE–Y (Sm/Yb$_{NMORB}$ $<$ 1·87, av. = 1·41) and the least-enriched light REE (LREE) profile segments (av. La/Sm$_{NMORB}$ = 2·295). The large ion lithophile elements (LILE) and alkalis (Cs–Rb–K–Ba) are modestly enriched relative to adjoining REE in normalized incompatible trace element profiles, with a large K trough (common to all HALIP basalts) and a weak Ba trough (Fig. 10a). Alteration and contamination effects create scatter among LILE in some samples (Supplementary Data Fig. S2). Type a rocks are markedly enriched for all incompatible elements except Nb and Ta in comparison with enriched mid-ocean ridge basalts (E-MORB; Fig. 10a), with ubiquitous strong negative Nb–Ta

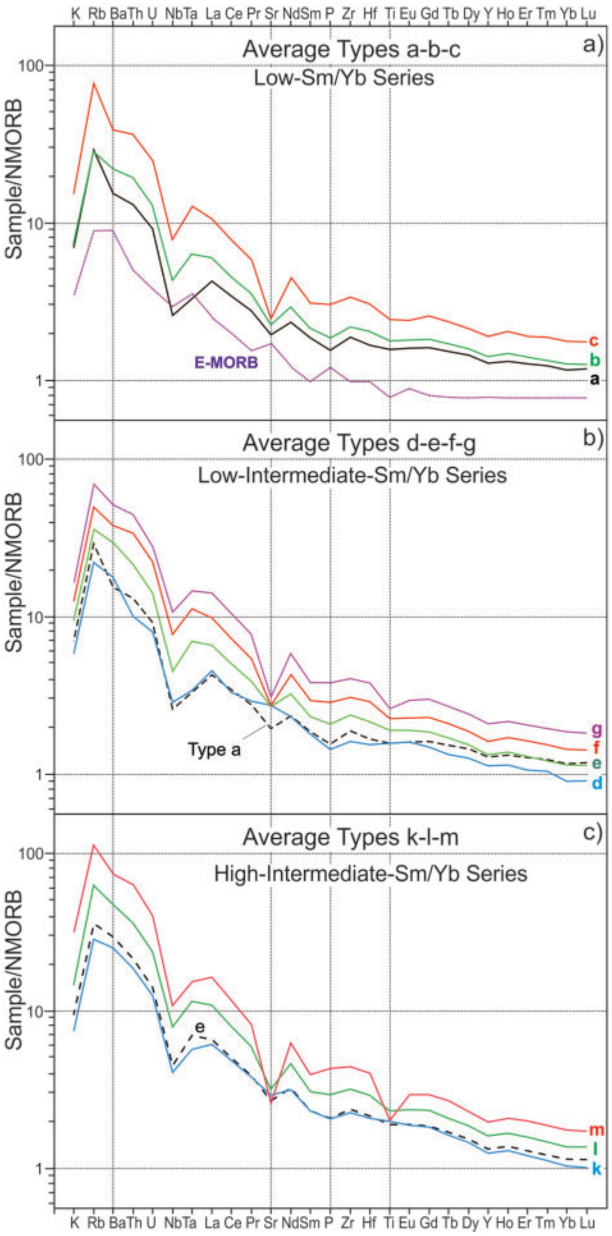

Fig. 11. Normalized incompatible element profile plots of average HALIP basalt types (see Table 2 for values). (a) Low-Sm/Yb_{NMORB} Types a–b–c compared with E-MORB; (b) Low–intermediate-Sm/Yb_{NMORB} Types d–e–f–g compared with Type a; (c) High–intermediate-Sm/Yb_{NMORB} Types k–l–m compared with Type e.

anomalies, distinct negative P anomalies, and weak negative Ti–Sr anomalies.

Five samples yielded unusually low incompatible trace element abundances (Supplementary Data Fig. S3a) and, compared with quasi-liquid (i.e. non-cumulative) Type a rocks, have generally higher contents of MgO (7–9·7 wt%), Al_2O_3, CaO (white squares with black centers in Figs 4–6) and Cr (250–346 ppm). Trace element modeling (Supplementary Data Fig. S3a) shows how these five rocks can be reproduced as mixes of average Type a liquid and 25–40 % equilibrium olivine + plagioclase + clinopyroxene in cotectic proportions. We infer these five depleted magnesian rocks to be mafic cumulates.

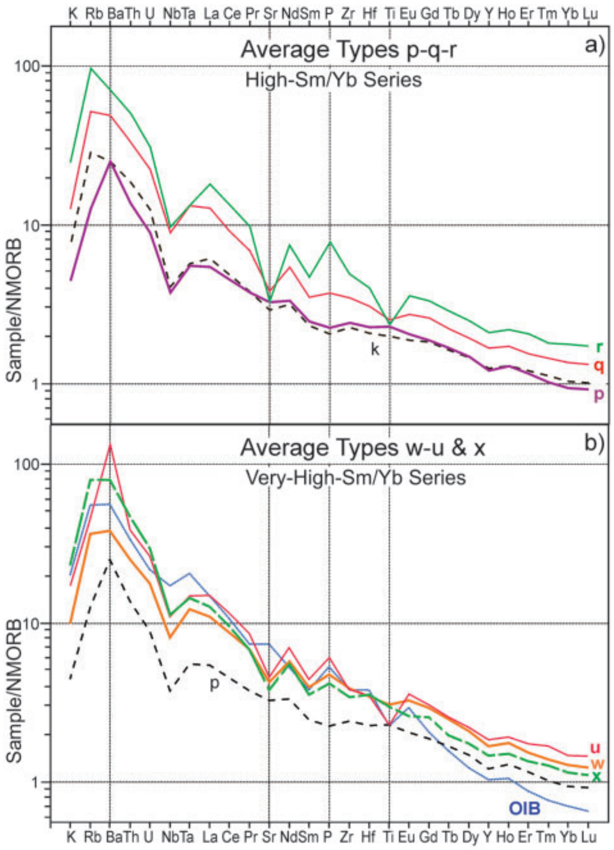

Fig. 12. Normalized incompatible element profile plots of average HALIP basalt types (see Table 2 for values). (a) High-Sm/Yb_{NMORB} Types p–q–r compared with Type k; (b) Very High-Sm/Yb_{NMORB} Types w–u and x compared with Type p and OIB.

Type b ($n = 44$) basalts occur in both the Isachsen and Strand Fiord eruptive units, but Type b rocks are most commonly intrusive. Type b rocks generally have lower Cr, Ni, and MgO (av. MgO = 5·37 wt%: Fig. 4, Tables 1 and 2) than Type a. Type b basalts are (like Type a) constrained to have HREE–Y segments with shallow slopes (Fig. 2, av. Sm/Yb_{NMORB} = 1·591), and there is considerable compositional overlap between Types a and b for LILE, the moderately incompatible high field strength elements (HFSE: Ti–P–Zr–Hf), and the MREE–HREE (Fig. 10b). Like Type a, Type b basalts have strong negative Nb–Ta anomalies and weak negative Sr–Eu anomalies (Figs 7 and 10b), and although small negative Ti–P anomalies are common, they are not ubiquitous. Although there is overlap, Type b has systematically steeper LREE slopes (av. La/Sm_{NMORB} = 2·808), and distinctly higher abundances of LREE (Ce is higher by definition), very incompatible HFSE (U–Th–Nb–Ta), and some LILE. Notably, the most incompatible elements show higher b/a enrichment factors (*ef*) (where b/a indicates av. Type b/av. Type a) than less incompatible elements. Specifically, the b/a *ef* is ∼1·7 for Nb, ∼1·4 for Ba, ∼1·5 for Th, ∼1·3 for Ce, ∼1·2 for Zr, ∼1·2 for P, ∼1·1 for Ti, and ∼1·1 for MREE–HREE.

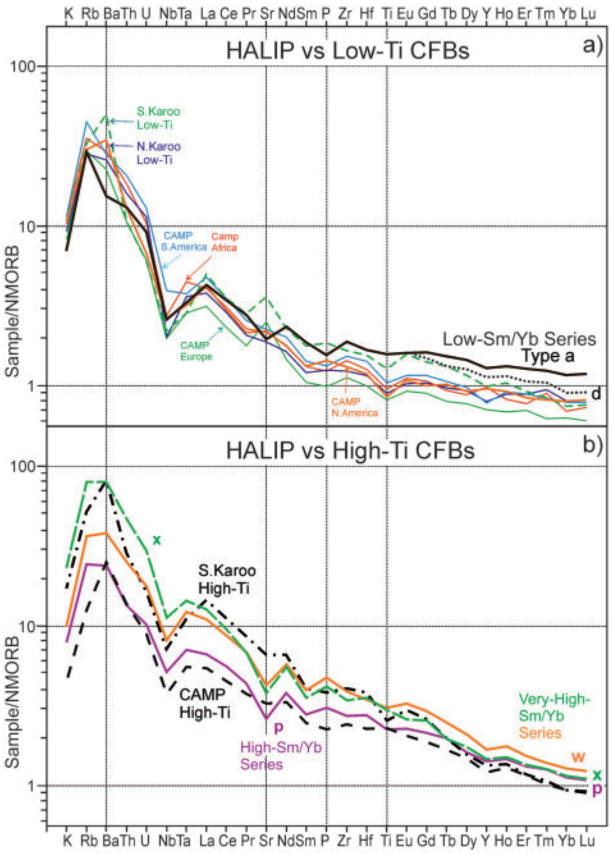

Fig. 13. Normalized incompatible element profile plots comparing HALIP basalts with other CFBs. (a) Average HALIP Type a and the HREE segment of Type d compared with Low-Ti CFBs from the Karoo and central Atlantic magmatic province (CAMP). (b) Average HALIP Types p, w and x compared with High-Ti CFBs from the Karoo and CAMP. CAMP data are from Callegaro *et al.* (2013, 2014); Karoo data are from Luttinen *et al.* (2015).

Type c rocks ($n = 10$) constitute the high-Ce, low-MgO end-member of the proposed a–b–c Series and occur in both volcanic formations and as rare intrusions. Overall, Type c rocks have normalized trace element profiles very similar in shape to those of the most enriched Type b rocks (Fig. 10c), with weak negative P–Ti anomalies and increasingly prominent negative Sr–Eu anomalies (Fig. 7a and d). The c/b enrichment factors are highest (~1·8) for very incompatible elements (U–Th–Nb–Ta), decrease to ~1·7 for LREE, to ~1·5 for Nd–Sm–Zr–Hf and to ~1·37 for MREE–HREE (Gd–Lu).

We interpret two unusually magnesian samples from Dostal & MacRae (2018) as cumulative based on their higher MgO, Al_2O_3, and CaO (white circles with black centers in Figs 4–6), higher Cr and Ni contents, and depleted REE profiles; but we could not unambiguously relate them to Type b liquids (Supplementary Data Fig. S3b). A few low-MgO Type b and c samples are enriched in Al_2O_3–CaO–Sr§–Co–Sc–V–Cr–Ni (Figs 4a–7a; Supplementary Data Table S1).

Three samples from Dockman *et al.* (2018) with low Sm/Yb ratios are shown as black '+' symbols in variation diagrams (e.g. Fig. 2). They have relatively flat HREE profiles that show many resemblances to Types a and b (Supplementary Data Fig. S3d), but are anomalous in having prominent positive peaks for P–Zr–Hf–Ti. Whether this is an unrecognized analytical problem or whether these are a truly distinct low-Sm/Yb HALIP magma subtype cannot be determined with certainty. Sample DMD160 yielded a 120·3 ± 0·8 Ma U–Pb zircon age (Dockman *et al.*, 2018).

Intermediate-Sm/Yb tholeiites of the volumetrically dominant d–e–f–g and k–l–m Series

Type d–e–f–g rocks have slightly steeper normalized HREE–Y segments than Type a–b–c rocks for equivalent values of Ce (Figs 2 and 11b; Supplementary Data Fig. S4). The very high Ce values of Type g have no equivalent in the Low-Sm/Yb_{NMORB} a–b–c Series (Fig. 2). Type k–l–m rocks have still steeper HREE segments than Type d–e–f–g rocks (Fig. 11c; Supplementary Data Fig. S5). Notably, there are no rocks that have both Ce $<$ 27 ppm and $Sm/Yb_{NMORB} > 2{\cdot}15$, such that there is no equivalent to Type d in the k–l–m Series (Fig. 2). It is for this reason that a threshold between Series d–e–f–g and k–l–m was set at $Sm/Yb_{NMORB} = 2{\cdot}41$, just above the highest value for Type d, although we emphasize that the d–e–f–g/k–l–m division is artificial, as there is a continuous distribution of data between the two suites. A subset of low-MgO Type d–e–f–g and k–l samples are enriched in Al_2O_3–CaO–Sr§–Sc–V–Cr–Ni–Co (Figs 4b–7b; Supplementary Data Table S1).

Type d rocks ($n = 9$) are mostly intrusive, with one Isachsen Formation volcanic sample, and have average MgO = 5·7 wt%. Although Type d rocks differ from Type a in having steeper HREE profiles by definition (Fig. 2) they have similar ranges of LILE–HFSE–La–Sm, and have prominent negative Nb–Ta anomalies and modest negative P anomalies (Fig. 11b; Supplementary Data Fig. S4a). A few Type d rocks show slight positive Sr–Eu anomalies. Two Type d samples with very low incompatible trace element abundances are tentatively interpreted as cumulates (Supplementary Data Fig. S3c).

Type e ($n = 113$) rocks occur as intrusive rocks and in both volcanic formations. Type e rocks mostly have lower MgO–Al_2O_3–CaO–Sr§–Sc–V–Cr–Ni contents (av. MgO = 5·19 %, Figs 4–9, Tables 1 and 2) than Type d. One sulfide-bearing Type e sample from the Hare Sill (H in Fig. 1b), in direct contact with S-rich host shales, is anomalously Ni-rich (180 ppm). Negative P–Ti anomalies are common although not ubiquitous (Fig. 11b; Supplementary Data Fig. S4b). Most samples show negative Sr–Eu anomalies, but a few are enriched in Sr and Eu (Figs 7b, d and 11b). Type e rocks share the sloping HREE–Y patterns of Type d rocks but are more enriched in most incompatible elements (Fig. 11b; Supplementary Data Fig. S4b), with steeper LREE slopes (av. $La/Sm_{NMORB} = 2{\cdot}84$) and higher e/d enrichment factors (*ef*) for highly incompatible elements (e/d *ef* Ba–Pr∼1·7) vs the MREE and HFSE (e/d *ef* Nd–Ti∼1·37) and HREE–Y (e/d *ef* Gd–Lu∼1·23).

Type f ($n = 124$) rocks are common intrusive rocks and occur in both volcanic formations. They are generally more evolved (av. MgO = 4·46 wt%) than Type e, but there is much overlap (Figs 4–9). Profile shapes are similar to those of Type e overall, but at higher concentrations (Fig. 11b; Supplementary Data Fig. S4c), with steeper LREE slopes (av. La/Sm$_{NMORB}$ = 3·35), and higher f/e enrichment factors for the most highly incompatible elements (f/e *ef* K–Pr∼1·48), compared with MREE and HFSE (f/e *ef* Nd–Ti∼1·3) and HREE–Y (f/e *ef* Gd–Lu∼1·24). A few samples have prominent negative or small positive P–Ti anomalies, and all show prominent negative Sr–Eu anomalies (Figs 7b, d and 11b; Supplementary Data Fig. S4c).

Type g ($n = 8$) rocks are exclusively intrusive, with many samples representing coarser gabbros from the interiors of larger intrusions with more evolved compositions (av. MgO = 4·26 wt%). Profile shapes are similar to those of Type f overall, but at higher concentrations (Fig. 11b; Supplementary Data Fig. S4d), with slightly steeper LREE slopes (av. La/Sm$_{NMORB}$ = 3·67), but with only modest relative fractionation (g/f *ef*) of highly vs moderately incompatible elements. Small negative or positive P–Ti anomalies are common, and all have negative Sr–Eu anomalies (Figs 7b, d and 11b; Supplementary Data Fig. S4d), but only very evolved sample 15WJA-B008-B1 shows deep P–Ti troughs (Supplementary Data Fig. S4d).

Type k ($n = 29$) rocks are occur in both volcanic formations and as intrusive rocks. They have steeper HREE segments compared with Type e rocks (by definition, Fig. 2), but are otherwise very similar (Fig. 5c; Supplementary Data Fig. S6a), with av. MgO = 5·33 wt%. Negative P–Ti–Sr anomalies are common.

Type l ($n = 89$) are common as intrusive rocks and in the Strand Fiord Fm., with fewer occurrences in the Isachsen Fm. They are generally more evolved than Type k, with lower MgO–Cr–Ni contents (av. MgO = 4·42 wt%, Tables 1 and 2). Type l rocks show overall trace element enrichment compared with Type k rocks (Fig. 5c; Supplementary Data Fig. S6b), with higher l/k enrichment factors for the most highly incompatible elements compared with MREE–HREE. Prominent negative P–Ti–Sr–Eu anomalies are common. Type l have steeper HREE segments compared with Type f rocks (Fig. 2) but are otherwise very similar.

Type m rocks ($n = 7$) are evolved (av. MgO = 3·23 wt%) gabbros from the cores of intrusions. Type m rocks show overall incompatible trace element enrichment compared with Type l rocks (Fig. 11c; Supplementary Data Fig. S6c), but with only modest relative fractionation (m/l *ef*) of highly vs moderately incompatible elements. Prominent negative Ti-Sr anomalies (and Eu for most samples) seem to deepen as the overall abundance of incompatible elements increases, but P can show positive or negative anomalies (Fig. 11c; Supplementary Data Fig. S6c). Except for their steeper HREE segments, Type m are very similar to Type g rocks (Supplementary Data Fig. S6c).

High- and very High-Sm/Yb tholeiites of the p–q–r, w–u, and x Series

The dominant Intermediate-Sm/Yb$_{NMORB}$ subalkaline rocks grade into a sparser population of High- and Very High-Sm/Yb$_{NMORB}$ basalts (Figs 2 and 12; Supplementary Data Figs S6 and S7). Types p–q–r and w–u rocks have the same geographical distribution as lower-Sm/Yb HALIP basalts (Supplementary Data Fig. S1), but Type x rocks occur only along the northern coast of Ellesmere Island (Supplementary Data Fig. S1d) and are spatially associated with HALIP alkaline rocks (Estrada *et al.*, 2016, 2018; Bédard *et al.*, 2021; Naber *et al.*, 2021), to which they show many resemblances (Supplementary Data Figs S8 and S9).

Type p rocks ($n = 14$) occur as rare intrusions, but most ($n = 11$) are flows belonging to both members of the Isachsen Formation. No Type p rocks have yet been reported from the Strand Fiord Formation. Type p rocks have av. MgO = 5·31 wt% and they exhibit slightly more humped trace element profiles (concave downward, Fig. 12a; Supplementary Data Fig. S6a) compared with Type k rocks. Type p rocks typically have small positive Sr peaks and small negative P anomalies, with no obvious Ti anomalies. Two Type p rocks have unusually low MgO and high Al_2O_3–CaO–Sr§–Sc–V–Cr–Ni–Co (Figs 4c–7c; Supplementary Data Table S1).

Type q rocks ($n = 15$) are mostly intrusive, with a single extrusive example from the Walker Island Member of the Isachsen Formation. Compared with Type p, MgO is lower (av. = 4·48 wt%) but contents of TiO_2, P_2O_5 and FeO* (FeO* = total iron as FeO) are in the same range (Fig. 4, Tables 1 and 2). Type q MREE–HREE profiles are not as humped (Fig. 12a; Supplementary Data Fig. S6b) as Type p because of a strong relative enrichment of very highly incompatible elements (av. La/Sm$_{NMORB}$ = 3·64). The most highly incompatible elements have enrichment factors (q/p *ef* Ba-to-Ce ∼2–2·5) that are much higher than those of the MREE–HFSE (q/p *ef* for Nd–Sm–P ∼1·5) and Zr–Hf–HREE–Y (q/p *ef* ∼1·3). Prominent negative Sr anomalies deepen as the overall abundance of incompatible elements increases, but P and Ti can show either positive or negative anomalies (Figs 7c and 12a; Supplementary Data Fig. S6b).

Type r rocks ($n = 6$) are all intrusive with evolved compositions (av. MgO = 3·95 wt%) with low Sc and V (Figs 8 and 9). They have higher Zr/Ti ratios than most other tholeiites (Fig. 3) but remain sub-alkaline (Supplementary Data Fig. S2). Incompatible trace element abundances are systematically higher than for Type q (Fig. 12a; Supplementary Data Fig. S6c), but there is little relative fractionation of incompatible elements. All profiles have prominent positive P and negative Ti–Sr anomalies (Figs 7c and 12a; Supplementary Data Fig. S6c). Type r rocks generally resemble Type m (Supplementary Data Fig. S6c), the main differences being the strong positive P anomaly, a slightly steeper HREE segment, and marginally higher LREE contents.

Type w rocks (*n* = 16) are all intrusive, and are more evolved than Type p, with av. MgO = 4·69 wt%. They are transitional-alkaline in the TAS diagram (Supplementary Data Fig. S2), but sub-alkaline in the Zr/Ti vs Nb/Y plot (Fig. 3). They differ from Type p and q rocks in having steeper HREE profiles and higher contents of very incompatible elements (Fig. 12b; Supplementary Data Fig. S8a), higher TiO_2 contents (Tables 1 and 2), and commonly prominent positive P anomalies (Fig. 6b). Their LILE and TiO_2 contents are similar to those of HALIP alkaline suites (Supplementary Data Fig. S9).

Type u (*n* = 4) transitional-alkaline basalts occur as intrusions, or as flows of the Isachsen Formation, Paterson Island Member (Fig. 3; Supplementary Data Fig. S2). Intrusive sample DMD124M was dated as being of Strand Fiord age (91·7 ± 1·1 Ma thermal ionization mass spectrometry on zircon; Dockman *et al.*, 2018). They are evolved rocks (av. MgO = 3·65 wt%), with lower TiO_2, Sc and V (Figs 4b, 8c and 9c) than Type w. The normalized profiles are parallel to those of Type w, but have positive P anomalies, strong negative Ti anomalies and are enriched in LILE and LREE, showing some similarities to Type r rocks (Fig. 12b; Supplementary Data Fig. S7c and d).

Type x rocks (*n* = 5) are transitional-alkaline basaltic intrusions (Fig. 3; Supplementary Data Fig. S2) with MgO contents (av. = 4·67 wt%) similar to those of Type w, from which they differ in having higher contents of LILE–Th–U–Nb (Fig. 12b; Supplementary Data Fig. S7b), whereas most other incompatible elements, including P and Ti (Fig. 4), are generally at the low end of the Type w range. The profile shape is more dish-shaped (convex), in comparison with the more concave shape of the Type w profiles, and there are no P or Ti anomalies (Fig. 12b).

Summary of trace element signatures

Like many other continental flood basalt suites, HALIP tholeiites show overall enrichment in LILE, Th, U, LREE and Pb compared with E-MORB and have common negative Ta, Nb and Ti anomalies (Figs 10–13). The highest-MgO, Low- and Intermediate-Sm/Yb HALIP tholeiites (Types a and d), have incompatible element abundances similar to those of other low-TiO_2 CFBs (Fig. 13a), but HALIP basalt HREE segments are more enriched. The highest-MgO samples of the High- and Very High-Sm/Yb_{NMORB} HALIP tholeiites (Types p, w and x) resemble high-TiO_2 CFBs (Fig. 13b), with highly incompatible trace element contents approaching those of OIB, but with generally flatter HREE profiles (Figs 12 and 13b). The highest-Sm/Yb HALIP tholeiites (Types w and x) overlap compositionally with, and are probably gradational into, coeval OIB-like HALIP alkaline basalts (Fig. 3d; Supplementary Data Figs S8 and S9; see Bédard *et al.*, 2021). The large Pb peaks are problematic, but will not be considered quantitatively in the following discussion, as we suspect they may be the result of alteration.

Within a given Sm/Yb_{NMORB} bracket (among HALIP tholeiites), as the Ce contents increase, concentrations of compatible elements generally decrease (Figs 7–9) and negative Ti–Sr–Eu anomalies develop and deepen (Figs 10–12). These systematic geochemical patterns suggest that, within a given Sm/Yb_{NMORB} bracket, higher-Ce basaltic melts are descended from lower-Ce, more primitive parents, and so constitute magmatic differentiation series.

Radiogenic isotopes

Previously published and new Nd–Sr isotopic data (Fig. 14) show that Low-Sm/Yb Type a basalts, which are the least evolved and least enriched HALIP magmas, mostly plot at high εNd_{90} values, and represent some of the least crustally contaminated HALIP tholeiites. Most HALIP tholeiites (including Isachsen and Strand Fiord Formation flows) define an array that scatters around Curve 2 of Estrada *et al.* (2016), which is a mixture of OIB-like basalt and a fertile continental crustal component. Extensive deviation of HALIP tholeiites from the mantle array towards this continental crustal contaminant is consistent with a near-ubiquitous input of continental crust into HALIP tholeiites. There are no isotopic data for Type x rocks, but two analyses of Type w rocks plot squarely in the mantle array at high εNd_{90}, and are probably not strongly contaminated.

DISCUSSION

There is much debate about the source of the HALIP CFBs and of the enriched signatures that characterize them. In addition to two different isotopically defined crustal contaminants (Fig. 14), Estrada (2015) and Estrada *et al.* (2016) identified several mantle components: a dominant source component with an OIB-mantle composition, a subordinate OIB-like component they identified as deeply recycled oceanic crust, and possibly an enriched component interpreted as subcontinental lithospheric mantle (SCLM) metasomatized by ancient subduction or carbonatite metasomatism. Kingsbury *et al.* (2016) accepted the idea of widespread crustal assimilation in generating HALIP tholeiites, and also argued for a dominant plume head source for the HALIP basalts, but attributed increases in Ba/Th and Ba/Nb in Isachsen Formation basalts to contamination of plume basalts with mantle that had been polluted by subducted sediment. Shephard *et al.* (2016) and Dostal & MacRae (2018) rejected crustal contamination altogether, instead favouring melting of SCLM metasomatically enriched by ancient subduction processes between 0·7 and 0·9 Ga. Because of complexities with timing and spatial distribution, Dockman *et al.* (2018) rejected a role for melting of fertile veins and metasomes in the SCLM, and questioned the predominant

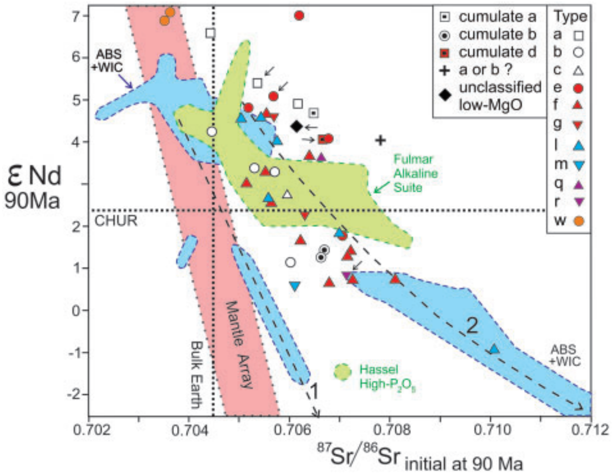

Fig. 14. Radiogenic isotope data for HALIP tholeiites. εNd_{90} and $^{87}Sr/^{86}Sr$ initial ratio values calculated for reference age of 90 Ma for all samples. New data are indicated by small arrows. Dashed arrow trends are from Estrada *et al.* (2016, fig. 14) with curve 1 indicating mixing between an OIB-like source mantle and a contaminant similar to granulite-facies lower crustal rocks, and curve 2 indicating mixing with a fertile upper crustal composition similar to Pearya succession 1 orthogneisses. Pale blue field is for Audhild Bay Suite (ABS) and Wootton Intrusive Complex (WIC) alkaline rocks; green field for Fulmar Suite alkali basalts and Hassel High-P_2O_5 volcanic rocks (from data compilation of Bédard *et al.*, 2021).

role of a plume in the younger (95–80 Ma) HALIP magmatism. Instead, they posited variable degrees of polybaric melting of ambient æsthenospheric mantle affected by edge-driven convection during rifting (King & Anderson, 1998; Kaislaniemi & van Hunen, 2014). Clearly, the CFB source debate is reproduced in microcosm by HALIP continental tholeiites.

Forward fractionation and assimilation–fractional crystallization modeling

We now develop a series of first-order tests of potential genetic relationships using a fractional crystallization and assimilation–fractional crystallization (AFC) approach, with the average HALIP magma types (Table 2 and Supplementary Data Table S1) acting as model sources and targets. The trace element modeling aims to test whether fractional crystallization can explain the compositional range of the HALIP tholeiites, or whether AFC processes are needed.

Constraints on fractionating assemblages

Petrographic observations (Estrada, 2015; Estrada *et al.*, 2016; Kingsbury, 2016; Kingsbury *et al.*, 2016; Bédard *et al.*, 2018, 2019; Dostal & MacRae, 2018; Naber *et al.*, 2021) show most HALIP tholeiites have sparse (5–15 %) phenocrysts, antecrysts and glomerocrysts of plagioclase, clinopyroxene and olivine, and are close to being (frozen) liquid compositions. Typical HALIP basalts with MgO < 7 wt% crystallize these phases in PELE models (Boudreau, 1999), and HALIP data mostly scatter along this three-phase cotectic (Figs 4–6). Values of CaO, Al_2O_3, Sc, Cr, Ni, Sr§ and Eu/Eu* generally decrease with MgO (Figs 5–8), consistent with extensive extraction of plagioclase, pyroxene and olivine. Consequently, our models initially focus on extraction of olivine gabbro and gabbro assemblages, with crystal extract modes guided by multiple PELE runs, which yielded average wehrlite (olivine:clinopyroxene 48:52 or 60:40), troctolite (olivine:plagioclase 36:64), and olivine gabbro (olivine:plagioclase:clinopyroxene 0·197:0·488:0·315) crystal extracts (also known as cumulates).

Values of FeO* and TiO_2 decrease in the lowest-MgO HALIP tholeiites (Fig. 4a and b), suggesting that melts became Fe–Ti-oxide saturated at about 3–4 wt% MgO, consistent with PELE (Boudreau, 1999) and MELTS (Naber *et al.*, 2021) modeling, and with marked decreases in Sc and V at low MgO (Figs 8 and 9). The most successful fits to the FeO* and TiO_2 inflection (Fig. 4a and b) were obtained at $H_2O = 1$ wt%, pressure = 1 kbar, and an fO_2 of QFM – 1 (where QFM is the quartz–fayalite–magnetite oxygen buffer); so we used these values in subsequent models. Petrographic data suggest that olivine disappears from the mineral paragenesis in the more evolved HALIP gabbros. To reflect the changes in the fractionating assemblage, we modeled the more evolved HALIP types with *ad hoc* crystal extracts of ilmenite- or magnetite-gabbro to achieve rough fits for negative Ti and Sr anomalies in those models.

Many High- and Very High-Sm/Yb_{NMORB} tholeiites (Types p–q–r and w–u–x), show trends of CaO–Sc depletion (Figs 5c and 8c), slight Al_2O_3 enrichment (Fig. 6c), and a shallow decrease of Sr§ with decreasing MgO (Fig. 7c), trends that are more consistent with clinopyroxene-rich fractionation assemblages. Some Type d–e–f–g and k–l–m rocks also show these trends, suggesting that although the volumetrically dominant Intermediate-Sm/Yb tholeiites experienced ubiquitous cotectic crystallization including extraction of plagioclase, there may be a cryptic, early, clinopyroxene-rich fractionation signature also. We will test hypothetical pyroxene-rich fractionation assemblages when modeling the higher-Sm/Yb Series.

Elimination of cumulates

It is important to ensure that the type averages represent liquid compositions amenable to our modeling approach. Higher-MgO rocks (Figs 4–9, symbols with dark cores) scatter towards higher Al_2O_3, CaO, Sr§ and Eu/Eu* (Figs 5–7), consistent with a gabbroic cumulate assemblage. As these rocks also exhibit marked depletion in incompatible trace element concentrations (Supplementary Data Figs S3a–c), we consider them to represent rare occurrences of intra-sill mafic cumulates, and exclude them from the quantitative modeling that follows.

Some low-MgO HALIP basalts have unusually high Al_2O_3–CaO–Sr§ (Figs 5–7), and scatter along vectors suggesting that they contain up to 30 % excess plagioclase. These rocks also show marked relative enrichment in Sc, V, Cr, Co, and Ni (Figs 8 and 9, Supplementary Data Table S1); which may indicate co-accumulation of an Fe–Ti-oxide mineral with high *D* values for these elements (e.g. Klemme *et al.*, 2006; Sievwright *et al.*, 2017). The absence of marked Fe enrichment of the low-MgO samples we interpret as plagioclase + oxide cumulates (Fig. 4a) suggests that the fractionated/accumulated oxide phase was usually ilmenite. We suspect that this plagioclase + ilmenite ± magnetite cumulus signature (PMIC; Supplementary Data Table S1) is the flip side of the decrease in Sr–Ti–V–Sc of other, quasi-liquid low-MgO rocks (Figs 4b and 7–9), possibly recording post-emplacement, intra-sill redistribution of strongly fractionated, ilmenite-saturated interstitial melts (Philpotts *et al.*, 1996; Latypov, 2003; Bédard *et al.*, 2007; Hayes *et al.*, 2015). Type averages including and excluding these PMIC variants are presented in Supplementary Data Table S1. For most type averages, the differences are insignificant. Where there was a significant difference, type averages excluding the anomalously PMIC-enriched samples were used in the modeling (Supplementary Data Table S1), and these PMIC-free average compositions are distinguished by an asterisk (e.g. p*).

Modeling crystallization and AFC

Instead of the analytical equations for Rayleigh distillation and end-member AFC (DePaolo, 1981), we applied the equilibrium crystallization equation (Hansen, 1980) in a stepwise fashion in 0·5 % increments (where $F_{1\text{–}0}$ is fraction of melt remaining in the system) with the results of each equilibrium crystallization step acting as the parent for the next crystallization step. To compensate for the progressive change of total mass of this shrinking model system and to make the stepwise model results congruent with results of the Rayleigh distillation equation, we gradually increased ΔF with a truncated expansion series [$\Delta F_n = \Delta F_{n\text{–}1} + (\Delta F_{n\text{–}1})^2$], where $\Delta F_{n\text{–}1}$ is the value of the previous crystallization increment, with $\Delta F_{\text{initial}} = 0{\cdot}005$. Assimilation was constrained to fixed *r* factors (where *r* is mass assimilated/mass crystallized) similarly to DePaolo (1981). Trial and error showed that $r = 0{\cdot}5$ yielded the best fits (Supplementary Data Fig. S13; see Ashwal, 2021), so most models shown are for that value. This may be partly a function of our chosen contaminants. Use of more enriched contaminants would have yielded lower *r* values. Model contaminants tested include generic continental crust (CC, Rudnick, 1995), and a variety of Sverdrup Basin host rock compositions from our unpublished data (Supplementary Data Table S2 and Fig. S10). These include: SBS (Sverdrup Basin Sedimentary), which is the average of 50 fine-grained sedimentary rock analyses from the Triassic Blaa Mountain Group and the Jurassic Heiberg Formation, mostly mudstones and siltstones; PMH (Phosphoritic Murray Harbour), representing the average of four phosphoritic siltstones from the Murray Harbour Formation; SMH (Siliciclastic Murray Harbour), the average of 20 organic-rich Murray Harbour Formation mudstones and siltstones, excluding calcareous and phosphatic facies; and GOF (Gypsiferous Otto Fiord), the average of four stratiform gypsum–anhydrite evaporites of the Carboniferous Otto Fiord Formation.

Values of *D* (Supplementary Data Table S3) were calculated using the parameterizations from Bédard (2005, 2006, 2014, and unpublished compilations for Fe–Ti oxides), constrained using average phenocryst mineral and whole-rock analyses from the Hare Sill (5·5 wt% MgO; Bédard *et al.*, 2018, 2019, unpublished data) as input parameters, with temperature (1115 °C) and other intensive parameters inferred from PELE models.

Figures 15–19 (and Supplementary Data Figs S11–S17) summarize representative model results. Normalization to model parental melts and linear scales are used because they directly reflect the daughter/parent enrichment factors (compare Supplementary Data Figs S11 and S12). The elements Cs, Rb, K and Pb were left out because they are particularly sensitive to alteration effects. The modeling constrains changes in fractionation assemblages with progressive differentiation, and with changing Sm/Yb. We believe these first-order quantitative models are sufficient to eliminate impossible hypotheses and offer plausible scenarios for relationships between HALIP type averages.

Model results

Low-Sm/Yb_{NMORB} Series

We begin with the Low-Sm/Yb_{NMORB} Series a–b–c. Figure 15a and Supplementary Data Figs S11 and S12 show the results of extracting various crystal assemblages from the average Type a basalt. The models show that closed-system fractional crystallization cannot reproduce the higher enrichment factors of the most highly incompatible elements of target compositions b and c (LREE), while also satisfying the less incompatible elements (HREE). Models involving extraction of pure clinopyroxene and wehrlite yield the ‘least-worst’ closed-system fractional crystallization results (Supplementary Data Fig. S12c and e), but are still failures, and are inconsistent with major and minor element variations (Figs 4–9) and petrographic data. Conversely, a much better fit to Type b (Fig. 15b, Supplementary Data Fig. S13) is obtained through AFC processes involving assimilation of either average continental crust (CC) or SBS (both with $r = 0{\cdot}5$) during 7·5–12·5 % crystallization of olivine gabbro. Similarly, 25–30 % AFC of Type a (or 20–25 % AFC of Type b) with CC or SBS contaminants yield reasonable matches to Type c (Fig. 15b and d; Supplementary Data Fig. S13). Use of a lower *r* factor (0·25) does not reproduce the very incompatible element enrichments as well (Supplementary Data Fig. S13). The apparent Nb–Ta enrichment of Type b and c compared with Type a shown in Fig. 15 reflects the fact that, on average, Type a basalts have a deeper Nb–Ta anomaly than Types b or c.

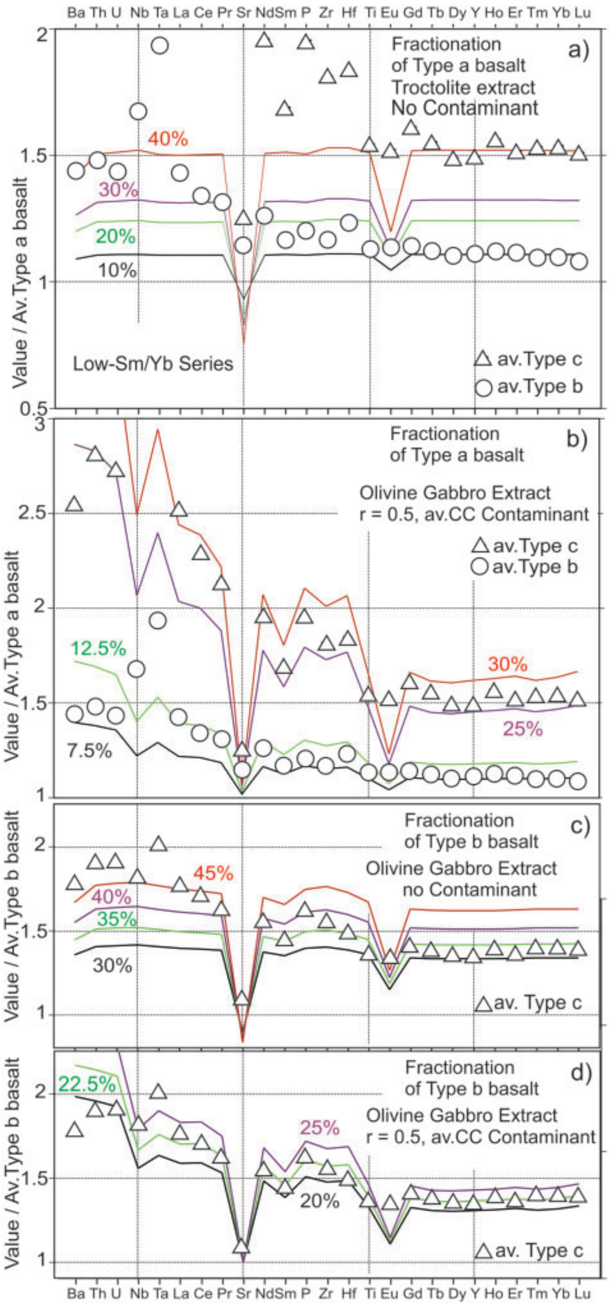

Fig. 15. Incompatible element profile plots of fractionation models normalized (linear scale) to model parent magmas (see Figs 2 and 3 for symbol codes). (a, b) Average Type a basalt from Table 2, with (a) troctolite crystal extract, no contaminant, and (b) olivine gabbro crystal extract, with contaminant = continental crust (CC, $r = 0{\cdot}5$). (c, d) Average Type b basalt parent (note the change in relative enrichment factors of Type c average because it is now normalized to Type b parent basalt), with (c) olivine gabbro crystal extract, no contaminant, and (d) same crystal extract but with CC contaminant ($r = 0{\cdot}5$).

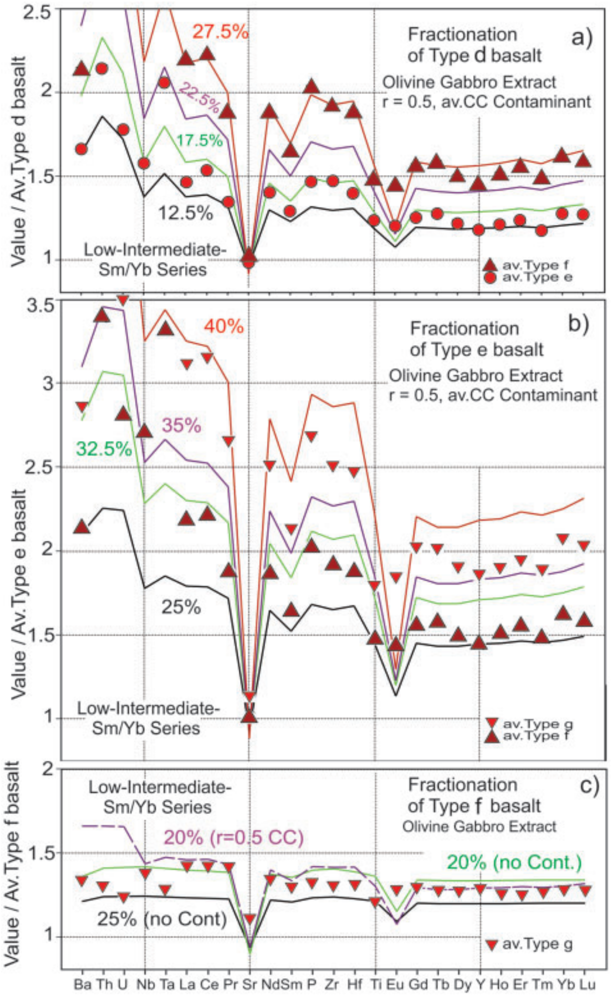

Fig. 16. Incompatible element profile plots of fractionation models normalized (linear scale) to model parent magma, olivine gabbro crystal extract. (a) Average Type d basalt parent, CC contaminant ($r = 0{\cdot}5$); (b) average Type e basalt parent, CC contaminant ($r = 0{\cdot}5$); (c) average Type f basalt parent showing two closed-system models, and an open-system model (purple) with a CC contaminant ($r = 0{\cdot}5$).

Low-Intermediate Sm/Yb$_{NMORB}$ Series

Attempts to model evolution from Type d parents to Type e and f daughters by closed-system fractionation of olivine gabbro also failed (Supplementary Data Fig. S14), whereas open-system AFC models seem able to generate Type e melts from Type d parents after 12·5–17·5 % AFC (CC contaminant, $r = 0{\cdot}5$, Fig. 16a), and Type f melts from Type e parents by 25–35 % AFC (Fig. 16b). Conversely, open-system processes may not be needed to generate Type g magmas from Type f parents (Fig. 16c), as 20–25 % closed-system crystallization yields reasonable fits. It should be noted that these calculations do not reproduce the small negative Ti anomalies of the Type f and g targets, suggesting that additional minor amounts of ilmenite crystallization must also have been involved in generating Types f and g.

High-Intermediate Sm/Yb$_{NMORB}$ Series

Internal variations among the k–l–m Series are analogous to those of the d–e–f–g Series. Closed-system models fail to generate Type l magmas from Type k parents (Supplementary Data Fig. S15a), whereas open-system AFC models yield much better fits (Fig. 17a). As

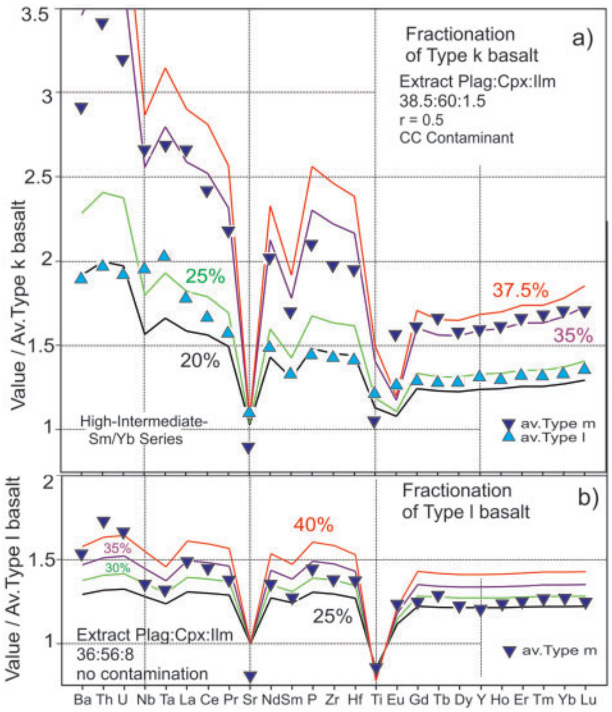

Fig. 17. Incompatible element profile plots of fractionation models normalized (linear scale) to model parent magma, feldspathic ilmenite clinopyroxenite crystal extract. (a) Average Type k basalt parent, CC contaminant ($r = 0{\cdot}5$); (b) average Type l basalt parent, no contaminant.

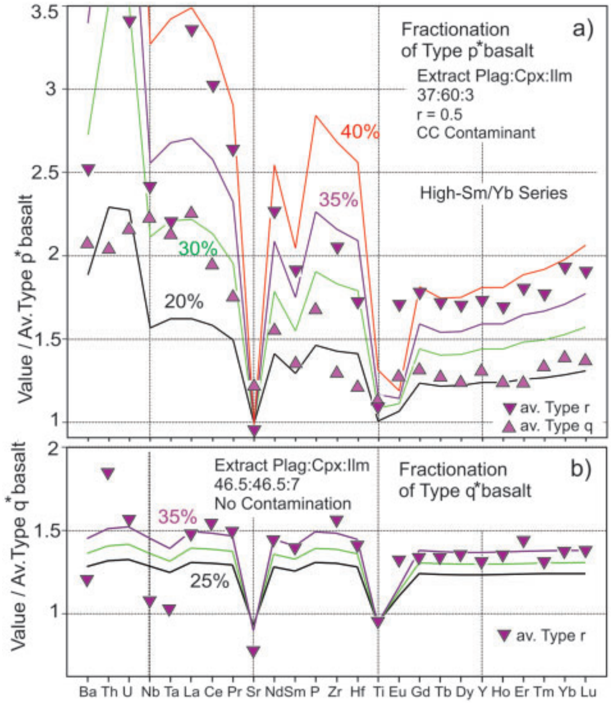

Fig. 18. Incompatible element profile plots of fractionation models normalized (linear scale) to model parent magma. (a) Average Type p* basalt parent, feldpathic ilmenite clinopyroxenite extract, CC contaminant ($r = 0{\cdot}5$); (b) average. Type q* basalt parent, ilmenite gabbro extract, no contaminant.

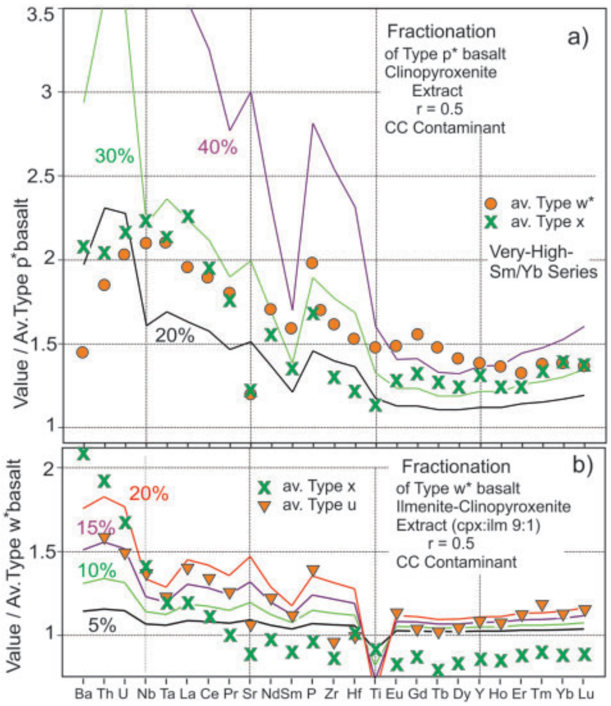

Fig. 19. Incompatible element profile plots of fractionation models normalized (linear scale) to model parent magma. (a) Average Type p* basalt parent, clinopyroxenite extract, CC contaminant ($r = 0{\cdot}5$); (b) average Type w* basalt parent, ilmenite clinopyroxenite extract, CC contaminant ($r = 0{\cdot}5$).

for Type g, open-system processes are probably not generally needed to produce Type m magmas from Type l parents (Fig. 17b), although the very high enrichment factors for Ba–Th–U suggest that there may have been some open-system behaviour.

High- and Very High-Sm/Yb$_{NMORB}$ Series

Internal variations among the p–q–r Series are in some ways analogous to those of the Intermediate-Sm/Yb k–l–m and d–e–f–g Series. Closed-system fractionation models fail (Supplementary Data Fig S16), whereas open-system AFC models better fit the Type q target (Fig. 18a). The fit is poor for the most incompatible elements, however, suggesting that *r* factors greater than 0·5 or a different contaminant may have been involved. The major difference from the models for lower-Sm/Yb Series is that the most successful p–q–r Series models require crystal extracts with more ilmenite and higher clinopyroxene/plagioclase ratios. The modeling suggests that open-system processes are probably not needed to produce Type r magmas from Type q parents (Fig. 18b), although getting from q to r requires higher plagioclase/clinopyroxene ratios than the p-to-q models, and abundant ilmenite extraction is needed to reproduce the deep Ti troughs of Type r. The models do not predict the deep negative Nb–Ta signatures of the Type r rocks, which may be the result of using $^{\text{Nb–Ta}}D_{\text{ilmenite}}$ values that are too small.

Because of clinopyroxene's high $^{Yb}D/^{Sm}D$ (Bédard, 2014; see Supplementary Data Table S3), extraction of this phase should increase the Sm/Yb ratio of residual melts, suggesting the possibility that some Very High-Sm/Yb rocks (Types w, u and x) could have had p-Type parental melts. Attempts to model this hypothesis with closed-system wehrlite and gabbro (not shown) crystallization models failed. Fits to Type w and x targets were only slightly better for models involving abundant clinopyroxene extraction (Fig. 19a; Supplementary Data Fig. S17b and c), with AFC processes worsening the fit, so providing no support for any putative p-to-w or p-to-x differentiation relationships.

A reasonably good fit to a Type u target melt (Fig. 19b) was obtained by AFC processes acting on a Type w parent with an ilmenite-clinopyroxenite crystal extract and a CC contaminant. We therefore tentatively consider Type u rocks to be open-system fractionation residua of Type w magmas, defining a w-to-u differentiation series. The Type x rocks show considerable major and minor element overlap with Type w (Figs 2 and 4–9c), but have distinct incompatible trace element signatures (Fig. 12b). We could not generate Type x residua from Type w parents with any of the crystallizing assemblages or contaminants we tested (Fig. 19b; Supplementary Data Fig. S17), and so Type x rocks are interpreted to represent a magma lineage distinct from the w–u Series.

Inverse fractionation and AFC modeling

Although no olivine-rich HALIP tholeiites are known in Canada, it seems likely that most HALIP basalts experienced early olivine-dominated fractionation after their primary melts separated from the mantle, a sequence typical of dry tholeiites (e.g. Herzberg & Asimow, 2008; Dockman *et al.*, 2018). For a first reconnaissance estimate, we restored the lowest-Ce, highest-MgO HALIP type averages (Types a, d, k and p) to equilibrium with a mantle containing Fo_{89} olivine, by adding equilibrium olivine in 1 % steps, using an Fe = Mg exchange coefficient of 0·3 (Roeder & Emslie, 1970), and assuming that 10 % of the iron in the melt was present in the Fe^{3+} state. Back-fractionation of incompatible trace elements was calculated using the same *D* values as for the forward models (Supplementary Data Table S3), except for compatible elements in olivine (Cr, Ni and Co), which were calculated with variable *D* values from Bédard (2005). Serving as a first-order approximation, these calculations show that about 40 % olivine back-fractionation is needed to obtain equilibrium with Fo_{89} mantle, yielding model parental melts a′, d′, k′ and p′ with 16–17 wt% MgO (Supplementary Data Table S4).

As open-system AFC processes seem to have affected almost all Canadian HALIP tholeiitic basalts, we posit that open-system behaviour probably also characterizes the unexposed primitive (>7 wt% MgO) part of the HALIP tholeiite suite. To model this, we extrapolated our AFC calculations (see above for method) backwards by progressively removing crustal contaminants as we added olivine, yielding more primitive and less contaminated open-system parental melts a", d", k" and p" (Supplementary Data Table S4). These decontaminated model parental melts have less prominent CFB signatures and more closely approach oceanic E-MORB compositions (Fig. 20).

Interpretation of model results

Results of the modeling are summarized in Figs 21 and 22. The Ce vs Sm/Yb_{NMORB} plot (Fig. 21) shows that open- and closed-system models yield predominantly steep Ce enrichment vectors with limited change of Sm/Yb, even for extensive crystal fractionation and AFC. As the CC and SBS contaminants have Ce contents that are lower than those of many HALIP basalts (Supplementary Data Table S2), such bulk contaminants are ineffective engines for absolute LREE enrichment through assimilation, although their low HREE abundances (Supplementary Data Fig. S10) cause important LREE/HREE fractionation (compare Fig. 15a and b).

The modeling implies that progressive incompatible trace element enrichment of HALIP basalts and synchronous clockwise rotation of the normalized

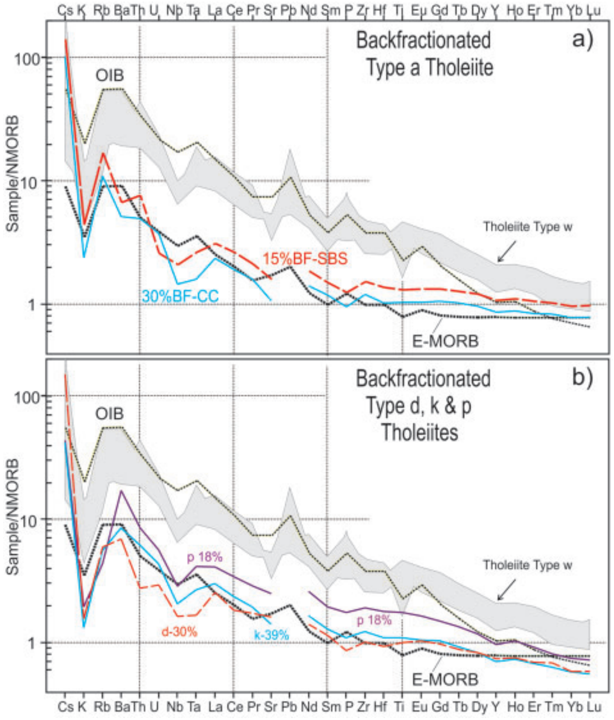

Fig. 20. Incompatible trace element profile plots normalized to N-MORB showing open-system back-fractionation models. All models added olivine (Fe = Mg $K_d = 0{\cdot}3$) with concomitant extraction of the model contaminant at each step ($r = 0{\cdot}5$). (a) Average Type a basalt starting point, comparing solutions for SBS and CC contaminants (Table 2). Similarity of decontaminated parental melts to highly incompatible part of the E-MORB spectrum should be noted. (b) Types d, k and p basalts with CC contaminant inversions. Similarity of decontaminated p-Type parent to shape of weakly contaminated Type w profiles should be noted.

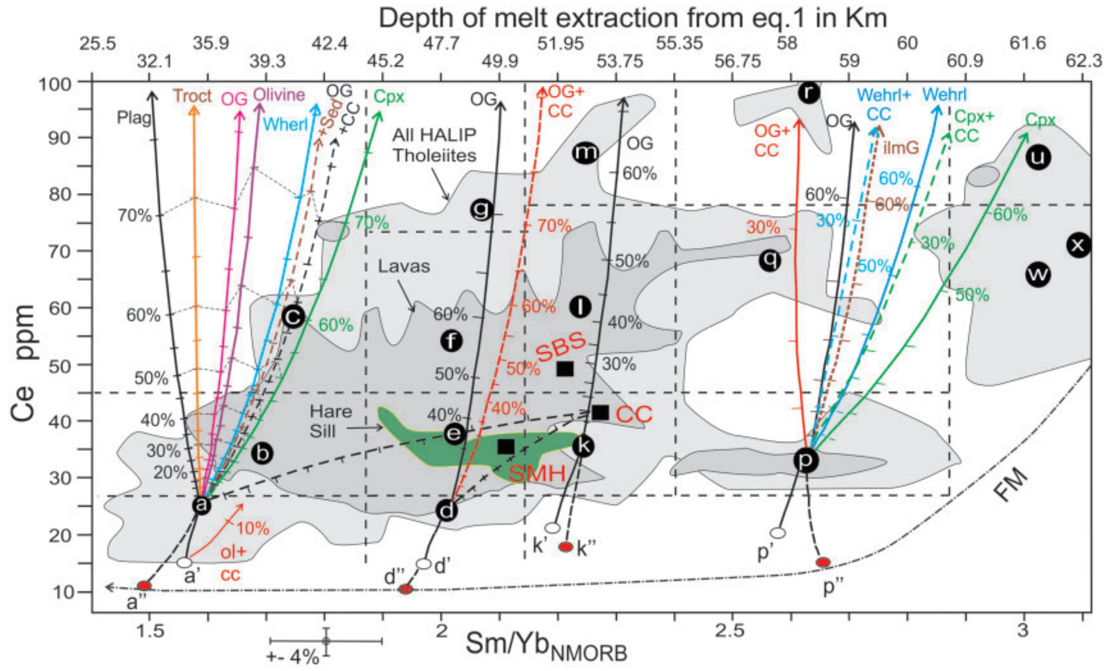

Fig. 21. Ce (ppm) vs Sm/Yb$_{NMORB}$. Grey field labelled 'lavas' encloses analyses of Strand Fiord and Isachsen Formation volcanic rocks. Paler grey background field encloses all HALIP tholeiites. Green field shows data from the Hare Sill (26 analyses). The Hare intra-sill scatter resembles range predicted by 4 % analytical uncertainty. Depth of melting in kilometers shown on the upper *x*-axis was calculated with equation (1). Bold white letters in black circles are averages of the tholeiitic types from Table 2. White ovals marked a', d', k' and p' are olivine back-fractionated parents restored to equilibrium with Fo$_{89}$ mantle (Supplementary Data Table S4). Red ovals marked a", d", k" and p" show end-result of inverse AFC paths (see text; Supplementary Data Table S4) involving progressive removal of the CC contaminant ($r = 0{\cdot}5$). Up-arrows emerging from the model parents show stepwise fractional crystallization models with ticks at 5 % intervals. Dashed arrows show AFC models, with $r = 0{\cdot}5$ for all models shown here. Labels indicate fractionating assemblage: Plag, plagioclase; Troct, troctolite; OG, olivine gabbro; Wehrl, wehrlite; Cpx, clinopyroxenite; IlmG, ilmenite gabbro; ol, olivine. Model contaminants are shown as black squares: CC, average continental crust; SBS and SMH, averages of Sverdrup Basin and Murray Harbour fine-grained siliciclastic rocks respectively (Supplementary Data Table S2 and Fig. S10). For the models with Type a parents, two very similar open-system olivine gabbro (OG) fractionation models involving CC and SBS contaminants are shown (both with $r = 0{\cdot}5$). Models with lower *r* values are not shown. They plot between these $r = 0{\cdot}5$ models and the closed-system model for the same extract assemblage. Dashed ticked lines linking average CC and average Type a and d tholeiites are bulk mixing curves (ticks at 10 % intervals). Dash-dot curve labeled FM is hypothetical fractional melting path of primary HALIP tholeiites.

incompatible trace element profiles (Figs 15–19) require open-system differentiation of a spectrum of lower-Ce higher-MgO magmas (a, d, k, p, w and x), involving contaminants resembling upper continental crust. For the Low and Intermediate-Sm/Yb$_{NMORB}$ Series, olivine gabbro extracts successfully reproduce the first stage of this evolution (a–b–c and d–e: Figs 15b, d and 16a), whereas variations among more evolved basalts (e–f–g and l–m: Figs 18b and 19b) are better fitted by gabbro and ilmenite gabbro extracts, consistent with major and minor element variations (Figs 4–9) and petrographic data. Variations of Al_2O_3, CaO, Sr§ and Sc vs MgO (Figs 5–8) are consistent with a more important role for early clinopyroxene fractionation in the higher-Sm/Yb Series (p–q–r and w–u), although the modeling also requires synchronous crustal assimilation, with fractionation of ilmenite and abundant plagioclase in the more evolved higher-Sm/Yb basalts. The most evolved basalt types (g, m and r), could have developed from their respective parental lineages by a final stage of near-closed-system intra-sill crystallization (Figs 16c, 17b and 18b), consistent with their typical occurrence as evolved gabbroic cores to larger intrusions.

As an improvement on plots of individual REE and their ratios, O'Neill (2016) proposed a polynomial parameterization of the REE profile of rocks with various shape coefficients. The $\lambda1$ shape coefficient reflects the linear slope of the chondrite-normalized REE profile, such that negative values imply LREE $<$ HREE whereas positive values indicate LREE $>$ HREE. The $\lambda2$ coefficient reflects the quadratic curvature of the chondrite-normalized REE profile, such that negative values indicate concave (humped) shapes, whereas positive values imply convex (dish- or bowl-shaped) profiles. In a $\lambda2$ vs $\lambda1$ plot (Fig. 22a), HALIP tholeiites scatter from compositions typical of evolved ocean floor basalts (OFB) to compositions resembling those of coeval HALIP alkaline rocks. In this plot, the HALIP tholeiitic series we defined above form linear arrays that are reproduced by our model AFC paths (Fig. 22b). Although magma Types w and x are indistinguishable in the Ce vs Sm/Yb$_{NMORB}$ plot (Fig. 2), they are clearly

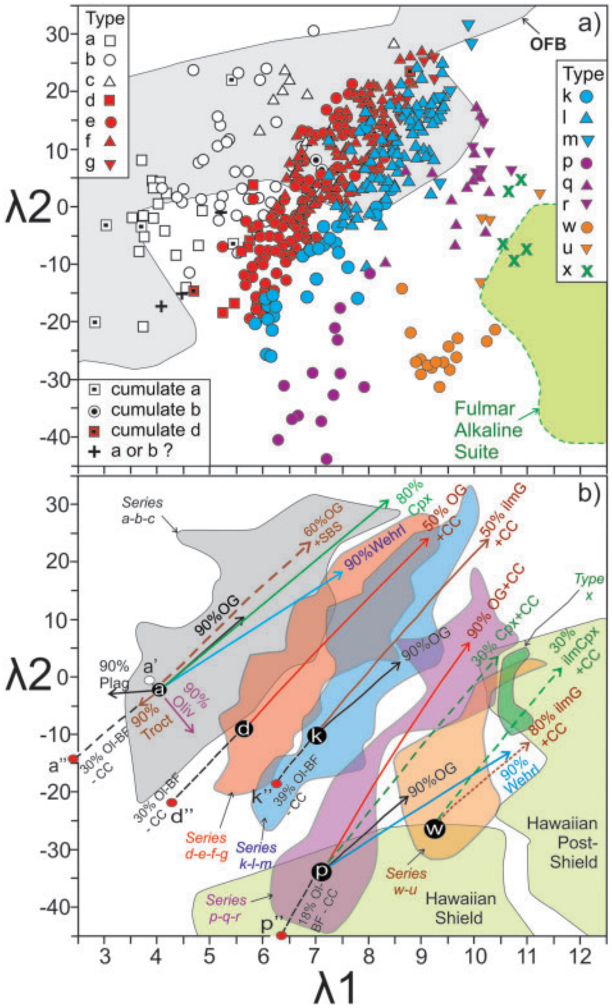

Fig. 22. λ_1– λ_2 plots calculated according to O'Neill (2016). (a) HALIP tholeiite types. It should be noted how the proposed HALIP series and types exhibit distinct ranges. Series a–b–c rocks overlap the field of ocean floor basalts (grey field marked OFB; from O'Neill, 2016), whereas Very High-Sm/Yb$_{\mathrm{NMORB}}$ types approach the range of the HALIP Fulmar Suite alkali basalts (green field) from Bédard *et al.* (2021). (b) Coloured translucent fields showing range of different proposed HALIP tholeiite series from (a), excluding cumulates. White lower-case letters in black circle are averages of the least evolved tholeiitic types (a, d, k, p, w). Dashed arrows show AFC models ($r = 0{\cdot}5$ for all models shown here) involving contaminants CC and SBS (Supplementary Data Table S2). Labels indicate fractionating assemblage: Plag, plagioclase; Troct, troctolite; OG, olivine gabbro; Wehrl, wehrlite; Cpx, clinopyroxenite; ilmCpx, ilmenite clinopyroxenite; Gb, gabbro; ilmG, ilmenite gabbro; Oliv, olivine; Ol-BF, olivine-back-fractionated. It should be noted how ineffective olivine fractionation is in creating variation in this diagram; and that closed-system differentiation models cannot explain intra-series ranges. Conversely, our open-system AFC models reproduce the magnitude and orientation of HALIP intra-series variations. Green fields for Hawaii are from O'Neill (2016). White oval marked a′ is an olivine back-fractionated parent restored to equilibrium with Fo$_{89}$ mantle (Table 3). Red ovals marked a", d", k" and p" are open-system back-fractionation models (see Fig. 20; Supplementary Data Table S4) involving progressive extraction of a continental crustal contaminant.

distinguished in the λ2–λ1 plot (Fig. 22a), which better integrates the REE spectrum.

Influence of polybaric mantle melting on geochemical signatures of HALIP tholeiites

All previous workers concur that the flat HREE profiles of most HALIP tholeiites reflect dominant spinel peridotite melting ($F \sim 10$–$15\,\%$: Estrada, 2015; Kingsbury *et al.*, 2016; Dostal & MacRae, 2018; Dockman *et al.*, 2018), whereas HALIP alkaline rocks with steeper HREE profiles mostly record lower-degree, higher-pressure, garnet-facies mantle melting (Estrada, 2015; Estrada *et al.*, 2016; Dockman *et al.*, 2018; Bédard *et al.*, 2021). The steps to higher λ1 as the HALIP tholeiites grade from the Low- to the Very High-Sm/Yb Suites mirrors the steepening HREE profiles (Fig. 21), with the decrease in λ2 indicating an increasingly humped profile shape (e.g. Fig. 12a). This shift is plausibly related to an increase in melting pressure and increasing involvement of residual garnet in the source mantle (O'Neill, 2016). Dockman *et al.* (2018) proposed that changes in Sm/Yb among HALIP magmas reflect both the pressure at which the parental melts separated from their mantle sources, and variable contributions from early, low-degree, high-pressure melt increments that separated from garnet peridotite residues. They formalized the Sm/Yb constraint on the depth of separation from the melting column with polybaric REE inversion models based on the approach of White & McKenzie (1995) and Gibson & Geist (2010), as applied to back-fractionated compositions of their least-contaminated samples. Using the Kaleidograph® fitting function, we parameterized the relationship proposed by Dockman *et al.* (2018, fig. 10) between Sm/Yb$_{\mathrm{PM}}$ and depth of melt separation, which they inferred equals lithospheric thickness, yielding

$$\begin{aligned}\text{depth in km} = {} & \left[133{\cdot}02\left(\frac{\mathrm{Sm}}{\mathrm{Yb_{PM}}}\right)\right] - \left[45{\cdot}343\left(\frac{\mathrm{Sm}}{\mathrm{Yb_{PM}}}\right)^2\right] \\ & + \left[6{\cdot}9628\left(\frac{\mathrm{Sm}}{\mathrm{Yb_{PM}}}\right)^3\right] \\ & - \left[0{\cdot}39713\left(\frac{\mathrm{Sm}}{\mathrm{Yb_{PM}}}\right)^4\right] - 84{\cdot}345\end{aligned} \tag{1}$$

where Sm/Yb$_{\mathrm{PM}}$ is normalized to primitive mantle of Sun & McDonough (1989). The inferred depth of separation from the melting column obtained with equation (1) was applied to the larger database we have assembled (Fig. 23). Taken at face value, these results imply that most HALIP tholeiites separated from their sources at depths between 45 and 55 km, but smaller volumes of HALIP magma formed at greater (up to ~72 km for alkaline magmas) and lesser (as shallow as ~27 km) depths.

A possible mechanism that could change Sm/Yb in HALIP tholeiites and mimic changes in melting pressure is a period of AFC prior to cosaturation in plagioclase. Figure 21 shows how olivine-back-fractionated model parent a′ would evolve in response to forward AFC processes involving assimilation of continental crust

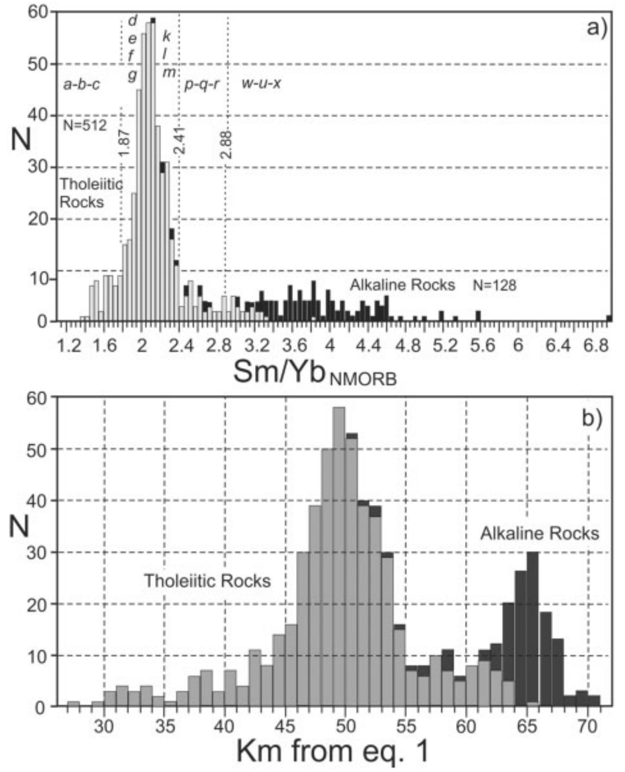

Fig. 23. Histograms of (a) Sm/Yb_{NMORB} and (b) depth of origin in kilometers calculated using equation (1) (this paper) from Sm/Yb_{PM} (normalized to primitive mantle; see Dockman *et al.*, 2018). It should be noted that crustal contamination has only a small effect on basalt Sm/Yb.

(CC, $r = 0{\cdot}5$). Whereas this open-system crystallization process enriches Ce back to the starting value after only 15 % crystallization (vs 44 % olivine back-fractionation to generate a′ from a), it causes a variation of Sm/Yb_{NMORB} of only 0·1 unit, clearly inadequate to explain the difference between Low-Sm/Yb Type a and Intermediate-Sm/Yb Type d, for example. Clinopyroxene crystallization also has the potential to change Sm/Yb, but even AFC ($r = 0{\cdot}5$) coupled with pure pyroxenitic crystal extracts cannot account for the wide range of Sm/Yb_{NMORB} observed in HALIP basalts (Fig. 21). Only bulk mixing yields significant change in Sm/Yb (e.g. thin dashed lines between average basalt a or e and average continental crust CC, Fig. 21). However, extensive bulk mixing with continental crust is inconsistent with the high FeO*, TiO_2 and P_2O_5 (Fig. 4) of magma Types b, e and k, for example, and could not explain enrichment in Sm/Yb_{NMORB} beyond the modest values (∼2·2–2·3) of a continental crustal contaminant in any case (CC in Fig. 21).

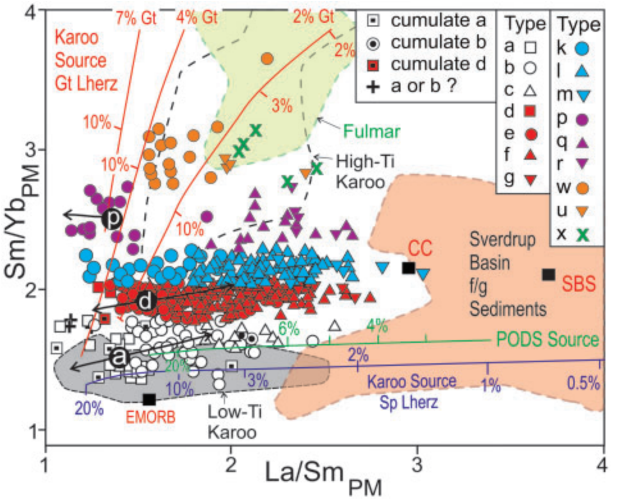

Fig. 24. Sm/Yb_{PM} vs La/Sm_{PM}. Data normalized to primitive mantle of Sun & McDonough (1989). Black squares marked CC and SBS are continental crust and Sverdrup Basin Siliciclastic contaminants (respectively) from Supplementary Data Table S2. Grey field shows range of Low-Ti Karoo tholeiites; dashed black line shows range of High-Ti Karoo tholeiites (Jourdan *et al.*, 2007, 2009). Melting paths are from Jourdan *et al.* (2007, 2009), computed using the equilibrium non-modal melting equation of Shaw (1970) with partition coefficients from McKenzie & O'Nions (1991). Melting path of Karoo low-TiO_2 best-fit spinel lherzolite (dark blue line) is from Jourdan *et al.* (2009) (source La = 1·10, Sm = 0·67, Yb = 0·55 ppm, initial mode olivine:orthopyroxene:clinopyroxene:spinel = 55:15:28:2; melting mode = 20:20:55:5). The Proterozoic Okavango dyke swarm (PODS) melting path (green line; from Jourdan *et al.*, 2009) was computed in the same way, but with a more enriched source (La = 1·80, Sm = 0·75, and Yb = 0·55 ppm). Garnet lherzolite (Gt Lherz, red lines) melting paths are from Jourdan *et al.* (2007), with source La = 1·35, Sm = 0·62, and Yb = 0·45 ppm; a melting mode (olivine:orthopyroxene:clinopyroxene:garnet = 16:12:81:15) modified from Walter (1998); and a range of source modal compositions (olivine:orthopyroxene:clinopyroxene:garnet = 69–64:20:9:2–7), with initial per cent garnet a function of pressure. Green field shows range of Fulmar Suite alkali basalts from Bédard *et al.* (2021), which overlap the Very High Sm/Yb basalt compositions. Black circles with white letters show average Type a, d and p tholeiites. Black arrows pointing left from these averages show open-system back-fractionation of olivine while removing a crustal contaminant (arrows end at position of a", d", p"). Black arrows pointing right are 30 % olivine gabbro crystallization coupled with CC assimilation ($r = 0{\cdot}5$). The close match with intra-series variations should be noted. Felsic rocks are excluded for clarity.

The contrasting effects of garnet- vs spinel-field mantle melting are illustrated in the Sm/Yb_{PM} vs La/Sm_{PM} plot (Fig. 24), which compares HALIP data with mantle melting paths computed by Jourdan *et al.* (2007, 2009) to explain the Karoo basalts. The different HALIP tholeiite series and types we have defined above form a set of extended arrays in this plot (Fig. 24), with the lower-MgO higher-Ce types scattering towards the right with increasing differentiation and contamination. As closed-system crystallization yields near-negligible variations of La/Sm_{PM}, the wide range of La/Sm_{PM} observed in HALIP basalts requires an open-system process, and our AFC models successfully reproduce the observed trends (Fig. 24). In this plot (Fig. 24) the least fractionated Type a HALIP tholeiites (and model open-system parent a") overlap the upper part of the Karoo low-Ti basalt field and have very low Sm/Yb_{PM}, corresponding to spinel lherzolite melting of mantle peridotite. HALIP basalts in general are more enriched and fractionated than the voluminous low-Ti rocks of the Central Atlantic Magmatic Province (CAMP) and Karoo CFBs (Fig. 13a).

The dominant population of HALIP basalts (Intermediate-Sm/Yb Series d–e–f–g and k–l–m) have Sm/Yb_{PM} significantly above the spinel peridotite melting paths computed for many other low-Ti CFBs (Fig. 24). This is consistent with either greater contributions from garnet-field melting increments, as proposed by Dockman *et al.* (2018), or a markedly more enriched source compared with other low-Ti CFBs and the Low-Sm/Yb HALIP CFBs. The High- and Very High-Sm/Yb_{NMORB} HALIP tholeiites plot along steep garnet-lherzolite melting curves (Fig. 24), indicating minimal spinel-field melting, and overlap with compositions of High-Ti Karoo and High-Ti CAMP basalts (Figs 13b and 24). High-Ti Karoo basalts are also interpreted to be high-pressure melts of fertile source mantle (e.g. Ashwal, 2021).

As a fractional crystallization linkage between HALIP Types p and w or x seems unlikely (Figs 19a and 21; Supplementary Data Figs S16 and S17), we consider it is more probable that Very High-Sm/Yb Types w and x are independently generated, lower-degree, higher-pressure melts transitional into the alkaline HALIP suites (see Supplementary Data Figs S8 and S9) discussed by Bédard *et al.* (2021). Comparison with the model melting paths of Fig. 24 suggests that High-Sm/Yb Type p magmas could represent >10% melting at depths corresponding to 4% garnet in the source; or ≫10% melting of a source at depths corresponding to 7% garnet. Very High-Sm/Yb Type w could then represent 8–10% melting at depths corresponding to a 4% garnet source; or 5–7% melting of a source with 2% garnet. In this scheme, Type x would record about 5% melting of a 2% garnet source.

When relatively unfractionated HALIP melts with similar Ce contents but differing Sm/Yb are compared (Figs 11 and 12), they differ mainly in the slope of the HREE pattern, whereas La/Sm varies little (Fig. 24 compares Types b, d, k and p, which have similar Ce contents). The close similarity of LILE and LREE of different HALIP basalt types is consistent with a similar degree of contamination or similar sources, but the systematic shift in HREE slope (Sm/Yb) is most simply explained as representing an increasing proportion of melt increments from a garnet peridotite source. Higher-Sm/Yb_{NMORB} HALIP magma series are also characterized by a stronger clinopyroxene and a weaker plagioclase fractionation signal (Figs 5c, 6c, 8c, 17, 18 and 21), which is consistent with a shift in phase topology caused by the higher alkali/silica ratios characteristic of lower degree or higher pressure melts (Sack *et al.*, 1987; Irving & Green, 2008; Green, 2015). A possible scenario to reconcile these observations is that many High-Sm/Yb_{NMORB} HALIP basalts (and some Intermediate- Sm/Yb_{NMORB} basalts also) experienced a stage of clinopyroxene-rich fractionation at depth, but that low-pressure gabbroic assemblages were subsequently extracted as the magmas rose through the crust. This is consistent with the well-known shrinkage of the clinopyroxene liquidus field with decreasing pressure (Bender *et al.*, 1978; Sack *et al.*, 1987; Bartels *et al.*, 1991).

The most evolved HALIP tholeiitic types (c, g, m, r and u) share a LILE–LREE signal and have the strongest negative Ti–Sr anomalies (Figs 11 and 12) and the lowest Sr§–Eu/Eu* values (Fig. 7). The shared LILE–LREE signal is consistent with a shared history after separation from the mantle, involving ubiquitous crustal contamination. Negative Ti anomalies and decreasing V imply common saturation in an Fe–Ti oxide mineral as melts evolved (Figs 4, 9, 11 and 12), whereas decreasing Al_2O_3–Sr§–Eu/Eu* (Figs 5 and 7) imply ubiquitous and extensive plagioclase fractionation. These geochemical signatures strongly support the notion that the most evolved rock types (c, g, m, r and u) are end-products of extended open-system differentiation histories that overprint a spectrum of parental melts ascending from various mantle depths. The growing positive P anomalies in the higher-Sm/Yb Series are more difficult to explain (Fig. 12). These P anomalies could indicate that some of these rocks are apatite cumulates, but they might also reflect a signature inherited from a heterogeneous mantle source containing apatite-rich pyroxenite (see Bédard *et al.*, 2021).

Given the inability of shallow magmatic fractionation or assimilation processes to change melt Sm/Yb significantly (Figs 21 and 24), we conclude that the gradation from Low- to Very High-Sm/Yb basalts in HALIP most probably reflects a polybaric partial melting process, much as proposed by Dockman *et al.* (2018). Early, low-degree, near-fractional melts generated at the highest pressures (Fig. 23) would dominate the highest-Sm/Yb HALIP magmas, which separated at greater depths and so experienced less spinel-field melting. In contrast, extensive shallow melting would have diluted high-pressure trace element signals to a larger extent in the lower-Sm/Yb Series. However, as previously pointed out (e.g. Lassiter & DePaolo, 1997; Jourdan *et al.*, 2009; Luttinen, 2018), it is difficult to untangle the combined effects of depth, source fertility, and melting dynamics. These intertwined uncertainties make it difficult to assess whether early garnet-field melt increments were added disproportionately as a result of melting dynamics in the case of the High-Sm/Yb HALIP basalts, or whether the bulk mantle source for higher-Sm/Yb HALIP tholeiites was inherently more fertile than the source of lower-Sm/Yb basalts. More detailed forward melting models involving composite sources will be needed to discriminate between these possibilities.

Dockman *et al.* (2018) argued that the depth of the lithosphere–asthenosphere transition at the HALIP rifted margin was an important control on basalt geochemistry, as this lid effect can constrain the depth at which decompression melting ceases, and may thus control the total extent of melting (Ellam, 1992; Niu *et al.*, 2011). Dockman *et al.* (2018) speculated that a stepped lithospheric depth profile created by rifting and thermal erosion controlled the depth of formation of HALIP tholeiites and alkaline magmas, yielding abundance peaks at ∼45 and ∼65 km, respectively. Application of their model [our equation (1)] to the more extensive HALIP dataset confirms a tholeiitic abundance peak between depths of 46 and 54 km, with a tail as shallow as 27 km for Low-Sm/Yb Series a–b–c tholeiites (Fig. 23). These shallow depths imply extensive decompression melting, which requires considerable lithospheric thinning. If the Dockman *et al.* (2018) approach is valid and the calculated depths are correct, then the Series a–b–c HALIP tholeiites indicate mantle decompression to depths that are shallower than the currently observed Moho beneath the Sverdrup Basin (Schiffer & Stephenson, 2018). Either the mantle lithosphere was substantially thickened by subsequent Eurekan orogenesis, which seems unlikely given the thin-skinned deformation style of the Eurekan Orogeny (Thorsteinsson & Tozer 1970; Piepjohn *et al.*, 2007, 2016; Piepjohn & von Gosen, 2018 ; Ruppel *et al.*, 2018; Stephenson *et al.*, 2018), or HALIP tholeiites flowed laterally (see Ernst & Baragar, 1992; Magee *et al.*, 2016; Beard *et al.*, 2017; Townsend *et al.*, 2017) from a more strongly extended and thinned continental margin to the north and west (e.g. White & McKenzie, 1989).

The Th/Yb vs Nb/Yb plot (Pearce, 2008) provides useful constraints on the relative roles played by crustal contamination and the fertility of the mantle source (Fig. 25). In this plot basalts from modern ocean ridges (MORB) and ocean islands (OIB) define an oblique band with a slope defined by melt/mantle residue partition coefficients. The position of any given liquid located in this band reflects the integrated melting and refertilization history of the mantle from which it was extracted. Basalts enriched in incompatible elements such as OIB come from the enriched end of the band at high Th/Yb and Nb/Yb because they reflect low-degree melts of fertile source mantle, whereas basalts depleted in incompatible elements such as N-MORB require higher melting degrees and separate from more refractory mantle. It is difficult to generate basaltic compositions outside this band by high-temperature, intra-mantle magmatic processes, but easy to do so by addition of an out-of-system component such as continental crust or sedimentary rocks, which have very different Th/Yb and Nb/Yb.

As only a handful of HALIP tholeiites plot within the OIB–MORB array (Fig. 25), the systematic offset to higher Th/Yb reflects ubiquitous addition of crustal components (see Pearce, 2008), either en route to the surface by crustal assimilation or, alternatively, by addition of crustal components to the mantle source prior to melting. Low-Sm/Yb Type a basalts plot at the lowest Nb/Yb (Fig. 25a), and would come from the most depleted mantle in the HALIP (between N- and E-MORB), but they still show marked deviation from the mantle array, indicating that even the most depleted and primitive HALIP tholeiites probably contain a continental crustal component. Types b and c do not show systematic offsets from Type a towards higher Th/Yb, but exhibit roughly similar deviation from the OIB–MORB array (Fig. 25a). Although some Intermediate-Sm/Yb Type e and f basalts show local clustering that suggests a steep AFC trend (Fig. 25b), overall, Types d–e–f–g show fairly similar offset from the mantle array, as do Types k–l–m and p–q–r. The Type w basalts overlap the range of Type q basalts, but show less deviation from the mantle array than most HALIP tholeiites (Fig. 25c). The transitional-alkaline Type x rocks overlap the field of HALIP Fulmar Suite alkaline basalts (green field in Fig. 25c). Open-system back-fractionation can bring HALIP tholeiites back into the center of the MORB–OIB field (Fig. 25) and makes the highly incompatible element spectrum of these decontaminated model parent melts more similar to that of E-MORB (Fig. 20; Supplementary Data Fig. S19). Forward AFC models effectively reproduce the observed HALIP compositional spectrum (Fig. 25).

Estrada *et al.* (2016) argued that two types of crustal contaminants were involved in HALIP basalts, pointing out that most HALIP tholeiites show Nd–Sr isotopic variations that fall along mixing lines with Pearya basement gneisses (equivalent to upper fertile crust; Fig. 14). The larger isotopic dataset, together with results of our AFC modeling, supports this interpretation. Because of uncertainties with respect to the composition of the underlying basement, most of our trace element models used a generic continental crust contaminant (Supplementary Data Table S2) that is not radically dissimilar to our fine-grained Sverdrup Basin siliclastic sediment average (SBS; Supplementary Data Fig. S10 and Table S2). Similarly, Naber *et al.* (2021) found that the tholeiitic lavas at the Hansen Point section (23 in Fig. 1b) define a tight trend in the Th/Yb vs Nb/Yb plot that can be explained by AFC processes involving average upper continental crust. However, it must be remembered that ascending mantle melts will never encounter average continental crust, but are more likely to react with a wide variety of lithologies and may preferentially mix with enriched partial melts of host rocks (e.g. Duffield & Ruiz, 1998; Troll *et al.*, 2005; Meade *et al.*, 2014), so all such theoretical predictions are necessarily simplified.

Dostal & MacRae (2018) rejected a role for common crustal contamination in HALIP tholeiites because of the observed Fe–Ti–V enrichment of differentiated HALIP basalts; and because elemental (e.g. Th/La) and radiogenic isotope ratios are poorly correlated with indices of differentiation such as SiO_2. We feel that neither argument precludes the possibility of extensive crustal assimilation in HALIP tholeiites. First, when the much larger global HALIP dataset is considered, the Fe–Ti–V enrichment trends are not as regular as would be expected from simple closed-system fractional crystallization processes, and we consider the major and minor element distributions of HALIP basalts to be too diffuse (Figs 4–9) to constitute a solid argument against crustal contamination scenarios. Addressing the second point raised by Dostal & MacRae (2018), poor correlations of melt SiO_2 with the extent of assimilation are a predicted consequence of the phase topology of tholeiitic basalts located on the plagioclase–clinopyroxene–

olivine and plagioclase–pyroxene cotectics, which buffer melt to near-constant SiO_2 during assimilation (Bowen, 1928; O'Hara & Herzberg, 2002). The inevitable heterogeneity of assimilated crustal compositions would cause additional geochemical dispersion. Moreover, there are local examples in the Canadian HALIP (e.g. the Hansen Point Tholeiitic Suite) where basaltic andesite was shown to be linked directly to associated basalts by AFC processes (Naber *et al.*, 2021). The multiple plagioclase antecryst populations in some HALIP rocks (Bédard *et al.*, 2018, 2019) and the chaotic volcanostratigraphy (see below) lead us to favour complex open-system differentiation models involving repeated replenishment events (Fig. 25d), which would further randomize correlations between incompatible trace elements, radiogenic isotopes and SiO_2 (see Duffield & Ruiz 1998; Troll *et al.*, 2005). The existence of such a periodically replenished open-system

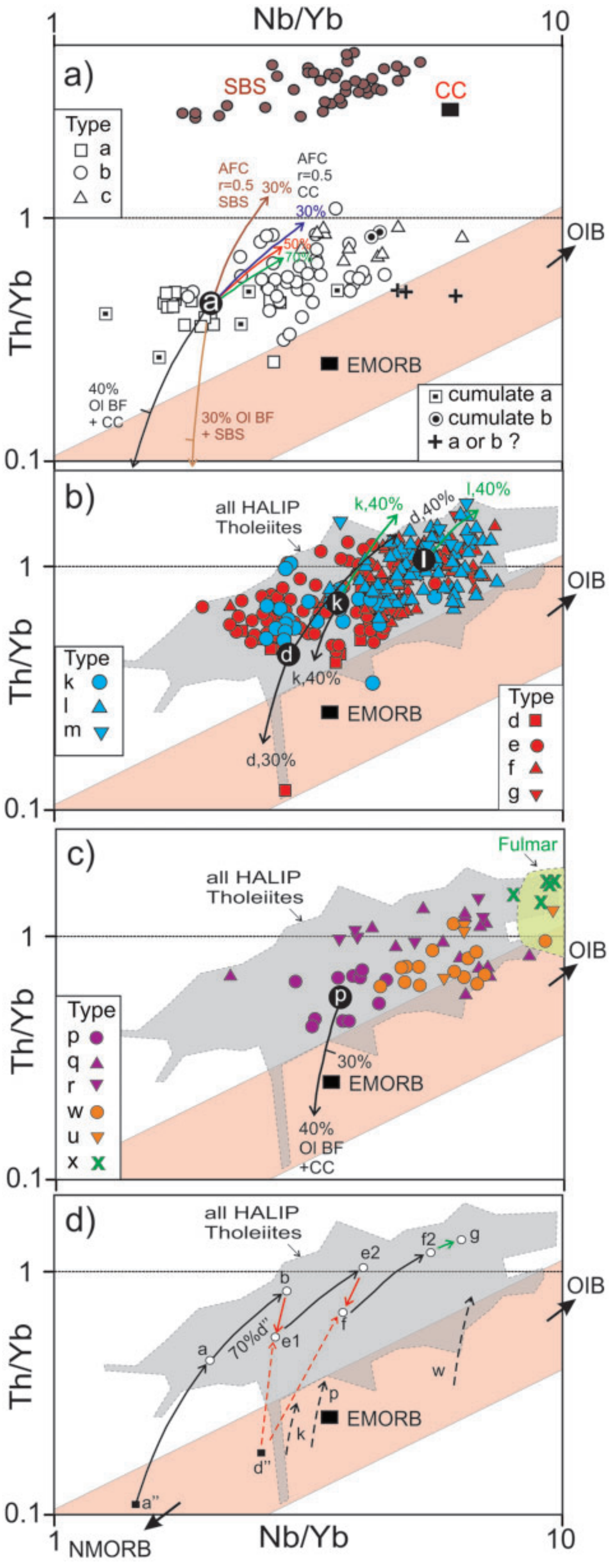

Fig. 25. Th/Yb vs Nb/Yb plot of HALIP tholeiitic rocks, adapted from Pearce (2008). Oblique beige field envelops modern OIB–MORB. E-MORB are from Sun & McDonough (1989). Brown circles are fine-grained siliciclastic rocks from the Sverdrup Basin (SBS; unpublished data); black square marked CC is average continental crust (Supplementary Data Table S2). (a) Series a–b–c tholeiites. Black circle with white 'a' is average Type a basalt, and is starting point for models. Down-trending arrows track back-fraction (BF) of equilibrium olivine while simultaneously removing contaminants ($r = 0{\cdot}5$) and bring Th/Yb values to the middle of mantle field. Black arrow marked 40% Ol BF + CC corresponds to removal of CC, whereas brown arrow marked 30% Ol BF + SBS reflects extraction of SBS during inverse AFC. The higher Th/Yb of SBS gives this calculation more leverage. Arrows pointing to upper right are forward AFC paths. Brown arrow shows effect of assimilating SBS while crystallizing 30% olivine gabbro ($r = 0{\cdot}5$), whereas navy blue arrow shows effect of the CC contaminant for similar r and %AFC. Red and green arrows show effect of smaller r values ($r = 0{\cdot}25$ red; $r = 0{\cdot}1$ green) for the CC contaminant and OG crystal extract. (b) Series d–e–f–g (red) and k–l–m (blue) tholeiites. Black circles with white letters are average Types d, k and l, and are starting points for models. Cumulates are not shown. Pale grey field encloses all HALIP tholeiites. Down-trending arrows shows result of back-fractionating equilibrium olivine from average Types d and k while simultaneously removing CC contaminant ($r = 0{\cdot}5$). Arrows pointing to upper right are forward AFC paths. Arrows labelled 'd , 40%', 'k , 40%', and 'l , 40%' show effect of 40% AFC with gabbroic crystal extracts and CC contaminant ($r = 0{\cdot}5$) from average Type d, k and l tholeiites, respectively. (c) Series p–q–r and w–u–x tholeiites. Black circle with white p shows average Type p basalt. Down-trending arrow shows result of back-fractionating equilibrium olivine while simultaneously removing CC contaminant ($r = 0{\cdot}5$). The overlap of Type x with Fulmar Suite alkali basalts (green field), from Bédard *et al.* (2021), should be noted. (d) Schematic illustration of one of many possible stochastic open-system differentiation paths for HALIP basalts in context of an AFC + RTX type plumbing system. For example, initial near-primary magma a" separates from mantle, and initially assimilates continental crust while crystallizing about 40% olivine, until melt reaches composition a (average Type a), where it co-saturates in plagioclase and clinopyroxene. An additional 30% AFC involving CC and an olivine gabbro crystal extract brings melt to b (typical Type b tholeiite), which could erupt or be stored in a sill system. Replenishment of this sill system by a Type d" primary magma now occurs. The red arrow shows effect of adding 30% of the d" parent to b, creating a new magma e1, which then evolves by AFC to e2. Again, this magma could erupt or be stored. Another replenishment by the same d" magma occurs, creating magma f, which experiences more AFC to generate f2. Local intra-sill closed-system fractionation then generates small amounts of Type g residual melt, which did not erupt. It should be noted that other types of replenishing melt could be added (Types k, p, w, ...) and mixing between any of the evolved products and hybrids can and probably did occur within the complex plumbing system.

magma chamber (AFC + RTX, where RTX means replenish tap crystallize; O'Hara, 1977; O'Hara & Mathews, 1981; Wooden *et al.*, 1993; O'Hara & Herzberg, 2002; O'Neill & Jenner, 2012; Potter *et al.*, 2018) could help explain (1) the limited spread to higher Th/Yb of HALIP tholeiites (Fig. 25d), (2) the contrast between the modest rate of decrease of MgO within any given series (Figs 4–9) and the extensive crystallization predicted by trace element modeling (Figs 15–19), and (3) steep FeO*–TiO_2 enrichment trends that do not match a single liquid line of descent (Fig. 4b and c).

Another school of thought attributes enriched signatures in CFBs to a fertile crustal component that resides in the mantle (Hawkesworth *et al.*, 1984, 1992; Turner *et al.*, 1996; Puffer, 2001; Wang *et al.*, 2016). Shephard *et al.* (2016) and Dostal & MacRae (2018) favoured melting of SCLM metasomatically enriched by ancient subduction processes to explain the CFB signature of HALIP basalts. Kingsbury *et al.* (2016) argued that increases in Ba/Th and Ba/Nb (Fig. 26) in Isachsen Formation basalts are best explained by a model involving a rising plume head that intersected a mantle domain polluted by subducted Ba-rich sediment. Kingsbury *et al.* (2016) further argued that the source of the younger Strand Fiord Formation magmas did not interact with this subduction-enriched material. However, when the larger HALIP dataset is examined, we see that although a few Isachsen Formation data do have markedly higher Ba/Th and Ba/Nb (Fig. 26), these extreme compositions are uncommon, and also occur in Strand Fiord age rocks. Ubiquitous involvement of a Ba-rich sediment-modified source mantle seems inconsistent with the dominant Ba-poor trend shown by most HALIP tholeiites (Fig. 27a). Taken together with the evidence for progressive contamination implied by our modeling (Figs 15–21), we conclude that the geochemical signatures of HALIP tholeiitic basalts probably do not reflect regionally extensive prior enrichment of their mantle source through fossil sediment subduction, but more probably record near-ubiquitous crustal contamination within the plumbing system after separation from the mantle.

Kingsbury *et al.* (2016) also argued that the high Th content of many HALIP tholeiites, together with the distribution of HALIP tholeiite data with respect to model mixing lines (their figs 16–19), implied that Sverdrup Basin sedimentary rocks were the most common shallow HALIP contaminant. HALIP tholeiites show a broad variation in Th/La (Fig. 26), but our AFC models (Figs 15–19, 21–22 and 24–26) show that the Th/La range of HALIP basalts can generally be explained by moderate extents of AFC involving a generic CC contaminant, as do plots of Rb vs Ba (Fig. 27a), and of Rb/Nb and Ba/Nb vs Nb/La (Fig. 28). However, there are a few HALIP samples with much higher concentrations of Ba, K, U, Th and Rb that cannot be explained in this way (Figs 26 and 27). There is no correlation between the extreme enrichment in Rb, Rb/Nb, Th/Nb or U/Nb of these anomalous HALIP tholeiites and LOI, suggesting that this enrichment is not primarily the result of late alteration. Nor are the highest Rb/Nb, Th/Nb or U/Nb values caused by inaccuracies in the denominator (Nb). We suspect that the rare HALIP basalts with very strong K–Rb–U–Th enrichment do indeed record intense localized interaction with sedimentary host rocks, as suggested by Kingsbury *et al.* (2016), but accounting for extreme Ba enrichment is more difficult. Sverdrup Basin phosphoritic sediments have high Ba (av. GOF Ba = 1531 ppm or $\mu g\,g^{-1}$; Supplementary Data Table S2); but the admixture of >30 % phosphorite sediment needed to generate high Ba/Nb (Fig. 26) would yield high P_2O_5 contents and good correlations between Ba and P_2O_5, neither of which are observed (Fig. 27b). Mixtures with gypsum or anhydrite (also common in the Sverdrup Basin) would be ineffective because of their low Ba contents (Fig. 26; Supplementary Data Table S2). On the other hand, many Sverdrup Basin fine-grained sedimentary rocks have Ba contents (e.g. SBS Ba = 845 $\mu g\,g^{-1}$ SMH Ba = 1216 $\mu g\,g^{-1}$; Supplementary Data Table S2) much higher than generic CC (Ba = 390 $\mu g\,g^{-1}$), and their ingestion could have strongly affected magmatic Ba contents. However, these Ba-rich sedimentary rocks all have high K–Rb–Th–U values, such that bulk assimilation would inevitably generate coupled enrichment trends that are not seen for HALIP Ba-rich rocks (Figs 26–28).

Data from the Hare Sill (Fig. 1b), emplaced into Ba-rich Murray Harbour Formation strata, provide an interesting reality check on speculation about the nature of Ba enrichment in HALIP magmatic rocks. Rocks from this fine-grained, weakly differentiated sill show almost exactly the same Ba/Th and Ba/Nb variations as used by Kingsbury *et al.* (2016) to argue for a fossil mantle sediment component (Fig. 26). However, apart from strong localized enrichment in Ba (Fig. 27a), U and S (Deegan *et al.*, 2018*b*), the Hare Sill data do not reveal the concomitant depletion of TiO_2 (Supplementary Data Fig. S18b), and enrichment of K_2O, Rb, Rb/Nb (Fig. 28a), or Th/La (Fig. 26) expected from extensive bulk contamination with adjoining wallrocks. Petrographic and field evidence implies the Ba-rich samples from the Hare Sill represent domains that were affected by late influx of sulfur-rich fluids, and our unpublished geochemical and experimental work suggests that syn- or post-emplacement transfer of H–C–S volatile species derived from contact metamorphism of the organic-rich host strata may have transported Ba in particular (Bédard *et al.*, 2016, 2018; Deegan *et al.*, 2018*a*, 2018*b*). We do not mean to imply that all Ba-rich HALIP tholeiites acquired their Ba in this way, but localized fluid-driven Ba enrichment from wallrocks must be considered a viable hypothesis for some.

An alternative possibility for unusual Ba or P_2O_5 enrichment of HALIP basalts is a heterogeneously distributed Ba- or P_2O_5-rich minor phase in the source mantle (see Embry & Osadetz, 1988; Kontak *et al.*, 2001; Estrada, 2015), with only the lowest degree melts among the tholeiites manifesting this source signature,

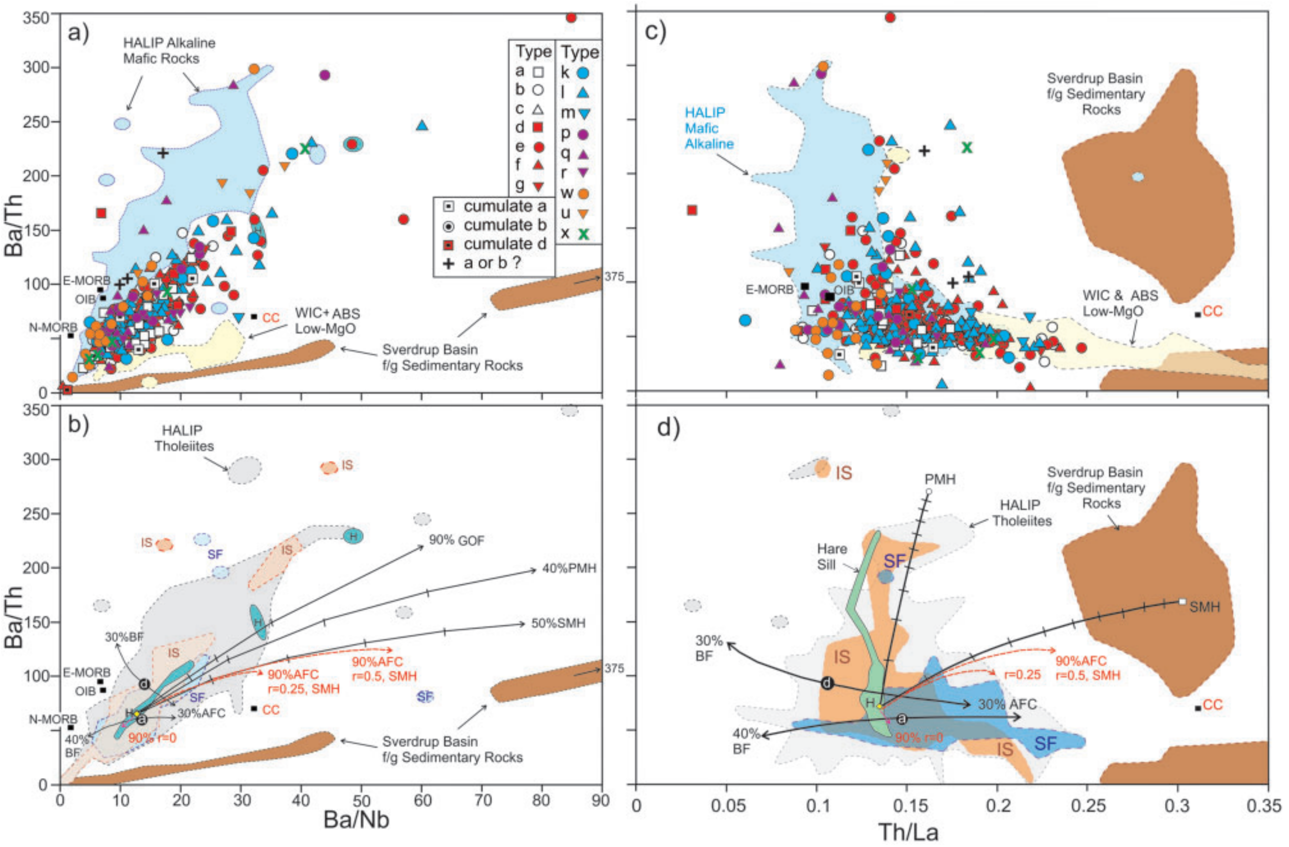

Fig. 26. (a) Ba/Th vs Ba/Nb and (c) Ba/Th vs Th/La for HALIP tholeiites. Sverdrup Basin fine-grained siliciclastic rocks are shown as a brown field, with many more samples plotting along this trend to much higher values of Ba/Th, Ba/Nb (to 375), and Th/La. Felsic rocks from the Wootton Intrusive Complex (WIC) and Audhild Bay Suite (ABS) are shown as a pale yellow field. The blue field shows the range of HALIP alkaline rocks (Bédard *et al.*, 2021). (b) Ba/Th vs Ba/Nb and (d) Ba/Th vs Th/La for model results. (Same scale as upper panels.) Here, rocks of the Strand Fiord Formation (blue field marked SF) and Isachsen Formation (orange field marked IS) volcanic rocks (and age-correlative intrusions) are distinguished as coloured fields. Some of the volcanic rocks have MgO $<$ 2 wt% and are not shown. Average Tholeiite Types a and d are shown as white letters in black circles. Open-system back-fractionation paths (black arrows labelled BF) trend left, away from average continental crust (CC), for tholeiite Type a (40 %BF) and d (30 %BF). Black arrows trending to the right show the effect of 30 % AFC involving a CC contaminant ($r = 0{\cdot}5$). Green fields marked H show distribution of Hare Sill rocks. Average low-Ba/Th Hare Sill intrusive rock (yellow diamond) was mixed with various local contaminants (Supplementary Data Table S2) to generate arrowed mixing lines with 10 % tick marks. These show the effect of adding 50 % Murray Harbour Formation siltstones and mudrocks (SMH), 40 % phosphorite from the same section (PMH), or 90 % Otto Fiord Formation gypsum evaporite (GOF, ticks $<$60 % are not shown). The small red arrow indicates 90 % gabbroic crystallization of the average low-Ba Hare Sill rock with no contamination (ratios decrease because Ba is less incompatible than Th or Nb during plagioclase extraction), whereas the dashed red arrows show result of AFC with $r = 0{\cdot}25$ and 0·5 involving the same SMH contaminant. Reproducing the extreme high-Ba/Th values of some HALIP tholeiites by contamination would require unrealistically large amounts of contamination or mixing, inconsistent with other geochemical signatures (Figs 4–9). The Hare Sill trend is not reproduced by bulk mixing or AFC involving its wallrocks (Murray Harbour Formation siltstones and mudrocks; SMH), and 60 % mixing with phosphorites (PMH) is inconsistent with the near-absence of variation in P_2O_5 and Rb shown by the Hare Sill data (Fig. 27b).

as discussed more extensively by Bédard *et al.* (2021). Variations of P_2O_5 vs TiO_2 and Zr in HALIP tholeiites (Supplementary Data Fig. S18) are less diffuse than P_2O_5 vs K_2O or Ba variations (e.g. Fig. 27b), suggesting that most HALIP tholeiites originated from a source having fairly uniform bulk P_2O_5/Zr and P_2O_5/TiO_2, which could represent either an ascending plume or a fairly homogeneous passive margin mantle upwelling zone. On the other hand, some HALIP tholeiites show unusual positive P peaks that may indicate the presence of apatite-bearing subordinate lithologies in their sources (Fig. 12; Supplementary DataFigs S6 and S7). Bédard *et al.* (2021) argued that apatite-bearing pyroxenites contributed P_2O_5, Ba and Eu to HALIP alkaline magmas, so we cannot exclude the possibility that the highest-Sm/Yb HALIP tholeiites may also have sampled such enriched source components.

HALIP flood basalt plumbing system and eruptions

The presence of multiple antecryst populations in HALIP tholeiites (Bédard *et al.*, 2018, 2019), when combined with the picture emerging from the data and discussion above, suggests a multiplicity of small magma chambers that frequently intersected, mixing magmas with differing antecedents (see Thompson *et al.*, 1972, 1980; Bédard *et al.*, 2007, 2012; Hayes *et al.*, 2015). For

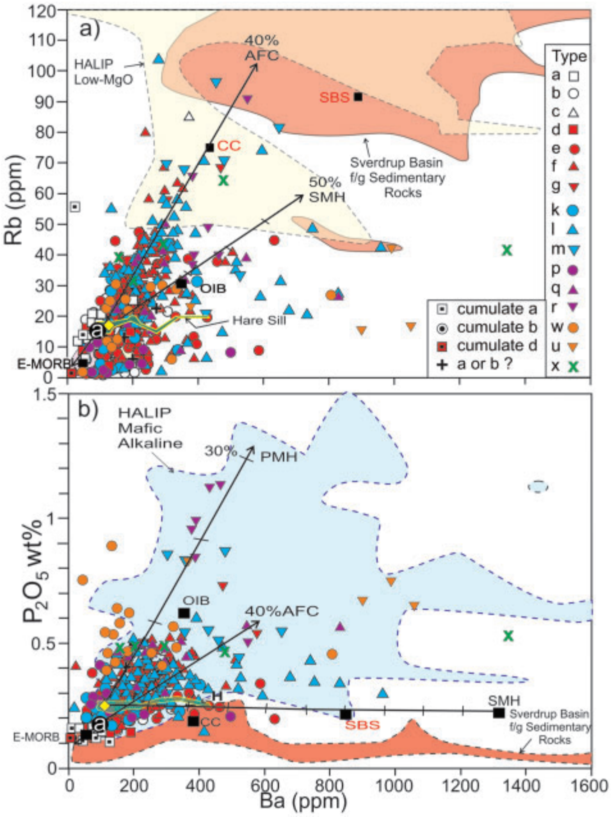

Fig. 27. (a) Rb vs Ba (ppm). Most HALIP tholeiites are collinear, forming a diffuse trend consistent with open-system fractional crystallization. Average Type a tholeiite parent is shown as white 'a' in a black circle, with the downward arrow showing the open-system ($r = 0{\cdot}5$, CC contaminant) back-fractionation path (40 %), whereas the long arrow pointing up shows the effect of 40 % olivine gabbro AFC ($r = 0{\cdot}5$, CC contaminant). A few data scatter to higher Ba, a trend clearly unrelated to assimilation of Rb-rich CC or SBS. Black arrow with 10 % tick marks shows effect of adding 50 % SMH (Supplementary Data Table S2; the phosphorite mixing trend is similar) to average low-Ba/Th Hare Sill rock (yellow diamond). The low Rb content of Hare Sill rocks precludes significant bulk addition of sedimentary host rock as an explanation for their high Ba contents. (b) P_2O_5 wt% vs Ba ppm. HALIP tholeiites form a diffuse cloud. Average Type a tholeiite parent is shown as white a in a black circle. The leftward arrow shows the open-system ($r = 0{\cdot}5$, CC contaminant) back-fractionation path (40 %), whereas the long arrow pointing diagonally up to the right shows the effect of 40 % olivine gabbro AFC ($r = 0{\cdot}5$, CC contaminant). Some High-Sm/Yb tholeiites (Types u and x) have exceptionally high Ba contents, suggesting either assimilation of very Ba-rich sedimentary rocks or a high Ba component in their source. Two black mixing curves with 10 % tick marks link average low-Ba/Th Hare Sill composition (yellow diamond in green field marked H) to local sedimentary rocks. The absence of P_2O_5 variation in Hare Sill rocks precludes phosphorite (PMH) mixing as an explanation for increasing Ba in that body. Addition of 25 % Murray Harbour sedimentary rock (SMH) would be needed to reproduce the highest-Ba Hare Sill sample, which is inconsistent with the narrow range of U/Nb, Th/La (Fig. 26) and Rb/Nb (Fig. 28a) of the Hare Sill data.

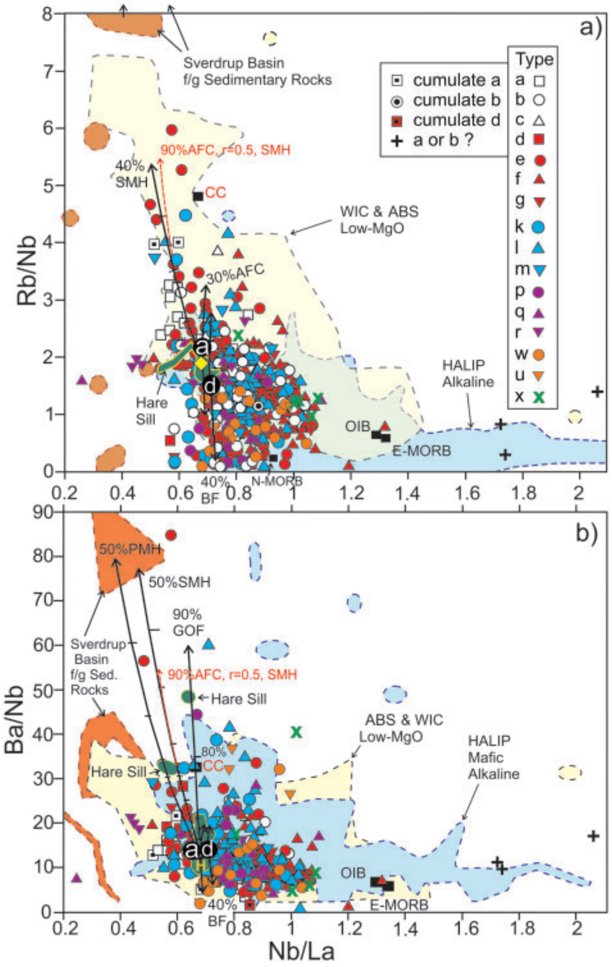

Fig. 28. (a) Rb/Nb and (b) Ba/Nb vs Nb/La. Most HALIP tholeiites have Rb/Nb < 3 and Ba/Nb < 25 with Nb/La (<0·8) lower than typical E-MORB. Only rare examples scatter to higher Rb/Nb and Ba/Nb, with values that approach or exceed average continental crust (black square marked CC), and overlap the lower range of Sverdrup Basin fine-grained siliciclastic rocks (brown fields). The SBS and SMH sedimentary rock averages have Rb/Nb >10 and Ba/Nb >100 (Supplementary Data Table S2). Pale yellow field is range of low-MgO felsic rocks from the Audhild Bay Suite (ABS) and Wootton Intrusive Complex (WIC) that indicate plausible local crustal contamination trends. White letters in black circles show average tholeiite Types a and d, with down-pointing black arrows showing open-system ($r = 0{\cdot}5$, CC contaminant) back-fractionation paths (40 %). Up-pointing black arrows show modest effect of 30 % olivine gabbro AFC ($r = 0{\cdot}5$, CC contaminant). Tholeiites with extreme Rb/Nb and Ba/Nb could reflect stronger interactions with sedimentary rock, but the Hare Sill data (green field) show marked Ba/Nb increase with a near-absence of Rb/Nb variation. Black arrowed lines with ticks show predicted effect of bulk addition of SMH, GOF and PMH (Supplementary Data Table S2) to average low-Ba/Th Hare Sill rock (yellow diamond); whereas dashed red lines shows result of 90 % AFC at $r = 0{\cdot}5$ involving an SMH contaminant. Enriched mantle sources that yield E-MORB, OIB (black rectangles), and coeval HALIP alkaline rocks (blue fields), extend to higher Nb/La (>2), but at uniformly low Rb/Nb and Ba/Nb, implying that the dominant enriched HALIP mantle component does not resemble common sedimentary rocks.

the HALIP there is field evidence for such convoluted plumbing systems, as Evenchick *et al.* (2015) mapped swarms of saucer-shaped sills on Ellef Ringnes Island; and Saumur *et al.* (2021) documented zones of cross-cutting and concordant sub-volcanic intrusions, most notably the ~20 km^2 zone at Middle Fiord and in localized portions of the 100 km-scale Schei Sill belt in Eastern Axel Heiberg Island.

Application of our interpreted tholeiitic basalt typology (Fig. 21) to sampled volcanic sections provides insight into the plumbing system that fed the HALIP flood basalt eruptions. For example, the volcanic section sampled by Dostal & MacRae (2018) shows no systematic geochemical trend vs stratigraphic height (Fig. 29), with a diversity of basalt types and series being erupted. Such a pattern is clearly inconsistent with a continuously differentiating evolving body of magma residing in a unique chamber. On the contrary, the lavas in this section seem to have randomly sampled several different reservoirs that contained melts derived from the mantle at different pressures, that were at different stages of evolution, and that had experienced variable extents of crustal contamination (Figs 21, 22 and 24). Other sampled HALIP volcanic sections show similar chaotic alternations of basalt types, with each section showing a different eruption sequence that cannot be correlated. For example, the Strand Fiord Formation has a b–b–e–f sequence at Arthaber Creek, f–e–e–f–e–l–e at Bastion Ridge, b–l–e–e–f–b at Celluloid Creek, and e–e–l–l–l–f–l–f–e–k at Twisted Ridge (section locations are shown in Fig. 1). This stochastic pattern suggests that multiple, probably small, independent magma reservoirs expelled their contents simultaneously to form these lava fields (Fig. 30). The presence of high-MgO spikes and low-pressure tholeiite types near the base and top of several sections, including the East Fiord section of Dostal & MacRae (2018, Fig. 29), further suggests that evacuation of the shallow reservoirs was triggered by entry of primitive replenishment pulses at the base or flank of the plumbing system (Fig. 30; see Bédard *et al.*, 2012).

The progressive elemental fractionations and enrichment of highly incompatible elements among the HALIP tholeiites (Figs 15–19, 21, 22 and 24) require open-system processes involving substantial ingestion of a contaminant resembling average continental crust. We infer that primary melts evolved by 30–40 % coupled olivine fractionation and crustal assimilation after separation from the mantle (Figs 20, 21 and 25). This first stage may have occurred in a Moho-level sill system (e.g. Cox, 1980; Francis *et al.*, 1981), but we cannot establish this from our data. We speculate that lower-crustal high-velocity zones (Schiffer & Stephenson, 2018; Stephenson *et al.*, 2018) may correspond to the ultramafic cumulates related to this level of HALIP evolution. This was followed by extensive cotectic-AFC/RTX differentiation in the crustal plumbing system, generating the observed range of incompatible element enrichment of HALIP basalts. Although co-eruption of lavas with different Sm/Yb ratios implies that the compartmentalized crustal plumbing system was ineffective at homogenizing ascending mantle melts, the progressive increase of the contamination signature as HALIP basalts evolved implies that there were frequent and cumulative opportunities for interaction with host rocks. The shallow inferred depth of separation from the mantle of most HALIP tholeiites (Fig. 23) implies that many HALIP basalts travelled laterally from a more strongly extended continental margin. Much mixing between different HALIP types and series could have occurred in the crustal plumbing system when partly solidified older conduits were reinjected by newly arriving magma (Fig. 30).

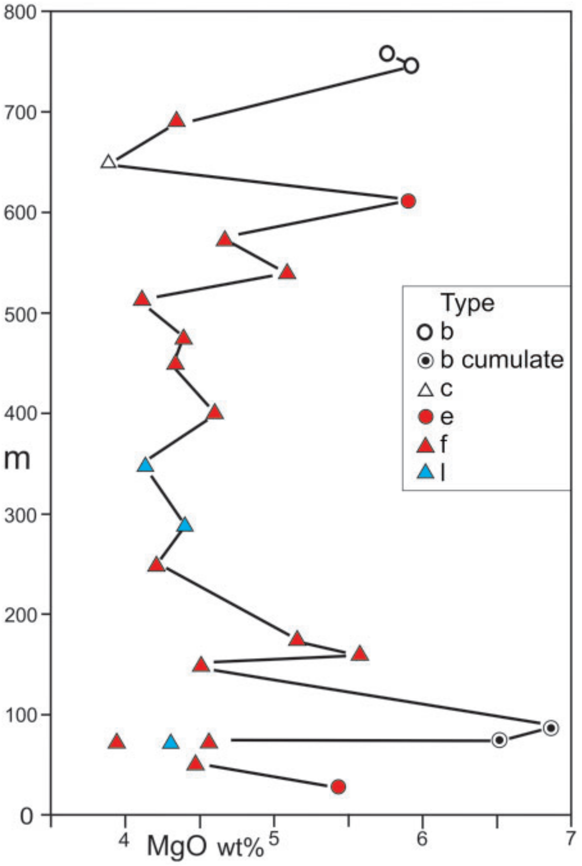

Fig. 29. Strand Fiord Formation volcanic section sampled by Dostal & MacRae (2018) showing the MgO content and HALIP typology we applied to these samples. Noteworthy features are the presence of early and late primitive Low-Sm/Yb magmas (Type b), an absence of regular progressions or regressions in MgO in the bulk of the eruption, and the alternation of flows belonging to three different Sm/Yb_{NMORB} Series.

CONCLUSIONS

HALIP tholeiites are enriched in incompatible trace elements compared with most low-Ti continental flood basalts. HALIP tholeiite types and differentiation series were defined using Ce vs Sm/Yb_{NMORB} distributions. Comparison with model melting curves implies that High-Sm/Yb HALIP basalts record low degrees of melting and separated from garnet-bearing sources. Conversely, Low-Sm/Yb tholeiites formed by extensive melting in the spinel-peridotite field. Intermediate-Sm/Yb tholeiites, which are the dominant HALIP population, experienced extensive spinel-field melting, but contain significant early garnet-field melt increments also.

Within a given Sm/Yb_{NMORB} range, Ce increases in HALIP basalts are associated with a systematic

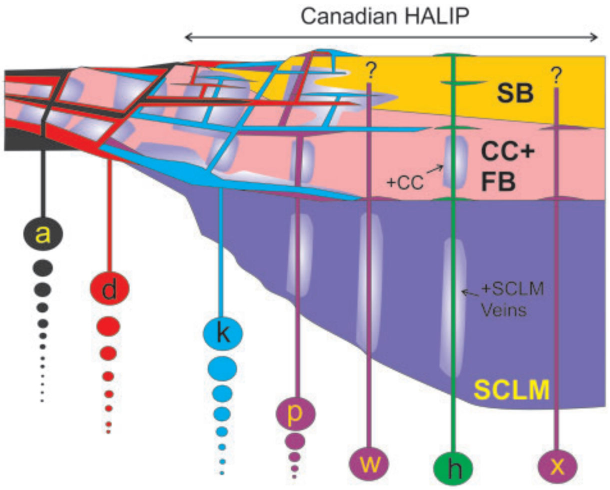

Fig. 30. Schematic view of the model we propose for the extended Arctic continental margin and HALIP magmatism. Low-Sm/Yb$_{\mathrm{NMORB}}$ melts such as Type a correspond to extremely thinned lithosphere dominated by extensive shallow melting. Higher-Sm/Yb magmas started melting at increasingly greater depths and experienced less shallow melting, making the deep melting signature more prominent. Some High-Sm/Yb tholeiitic magmas (Type p) and alkaline magmas such as the Hassel Formation basalts (Type h) may have preferentially scavenged SCLM components, whereas others (Type w) did not. Intermediate- and Low-Sm/Yb magmas (Types k, d and a) that formed under a thinned continental margin were injected laterally to create a dyke–sill network in the crust under and within the Sverdrup Basin sedimentary rocks. Crustal contamination probably occurred where the dyke–sill network was densest. Because intrusions often re-exploited pre-existing conduits, there was ubiquitous mixing associated with replenishment. When late Low-Sm/Yb melts such as Type a were injected into the sill system, the resulting over-pressure triggered eruption from multiple shallow reservoirs, creating the stochastic eruption pattern (e.g. Fig. 29).

clockwise rotation of normalized trace element profiles. Our systematic trace element modeling approach shows that this cannot be due to closed-system fractional crystallization, but requires progressive incorporation of continental crustal components. Such a progressive increase of the crustal contamination signature is inconsistent with a fossil source-enrichment model. The trace element and PELE models imply that HALIP basalts crystallized olivine initially, with Low-Sm/Yb HALIP basalts producing olivine gabbro assemblages after MgO reaches ~7 wt%. Ilmenite appeared in evolved melts with MgO < 3–4 wt%. In contrast, higher-Sm/Yb$_{\mathrm{NMORB}}$ basalts that fractionated greater proportions of clinopyroxene and ilmenite appeared earlier, but plagioclase fractionation is still needed to explain increasingly negative Sr–Eu anomalies.

The geochemical data and models indicate that Canadian HALIP tholeiites are strongly fractionated magmas that experienced near-ubiquitous crustal contamination, and that the dominant contaminant resembled continental crust. Back-fractionation models require about 40 % addition of olivine to achieve equilibrium with Fo$_{89}$ mantle. Open-system back-fractionation modeling shrinks the CFB signature, making the decontaminated model parental melts more similar to E-MORB. Unusually extensive assimilation of Sverdrup Basin sedimentary rocks may have caused localized over-enrichment in K–Rb–Th–U, but cannot explain uncorrelated Ba enrichment, which may record involvement of a Ba-rich lithospheric mantle component, or reflect fluid transfer of Ba from sedimentary host rocks. We conclude that the geochemical and isotopic signatures of HALIP tholeiitic basalts probably do not reflect regionally extensive prior enrichment of their mantle source through fossil sediment subduction, but more probably record near-ubiquitous crustal contamination within the plumbing system after separation from the mantle.

ACKNOWLEDGEMENTS

We thank the Polar Continental Shelf Project and its outstanding pilots for efficient logistical support, and staff at Resolute Base and Eureka Station for their generous hospitality. M.-C. Williamson, T. Hadlari and J. Galloway contributed samples and valuable discussions. É. Girard and F. Aucoin helped generate the location maps and assisted with data management. B. Cousens provided isotopic calculation spreadsheets. J. Dostal, C. Kingsbury and S. Estrada kindly provided data spreadsheets and discussion. Editor T. Waight, A. A. Sappin, V. Salters, S. H. Zhang and three anonymous reviewers are thanked for their valuable comments. This is NRCan-ESS-GSC contribution number 20210092.

FUNDING

Work by J. Bédard, B. Saumur, S. Grasby, K. Dewing and C. Evenchick was funded through the Geological Survey of Canada's GEM2 program. B. Saumur was funded via a Visiting Fellowship from the National Science and Engineering Research Council of Canada. Funding to V. Troll and F. Deegan was also provided by the Swedish Research Council (Vetenskapsrådet grants 2016-04838 and 2018-04933) and the Swedish Polar Institute. C. Tegner's fieldwork is an outcome of the joint Geological Survey of Canada and German Federal Institute for Geosciences and Natural Resources (BGR) Pearya Project: Circum-Arctic Structural Events expedition no. 19 (CASE 19) in 2017, led by K. Piepjohn and Stephen Grasby. C. Tegner acknowledges funding from the Danish National Research Foundation Niels Bohr Professorship grant 26-123/8 and BGR.

SUPPLEMENTARY DATA

Supplementary data are available at *Journal of Petrology* online.

REFERENCES

Anderson, D. L. (1979). The upper mantle TZ: eclogite? *Geophysical Research Letters* **6**, 433–436.

Anderson, D. L. (1994). The sublithospheric mantle as the source of continental flood basalts; the case against the continental lithosphere and plume head reservoirs. *Earth and Planetary Science Letters* **123**, 269–280.

Anderson, D. L. (2005). Large igneous provinces, delamination and fertile mantle. *Elements* **1**, 271–275.

Anderson, D. L. & Natland, J. H. (2014). Mantle updrafts and mechanisms of oceanic volcanism. *Proceedings of the National Academy of Sciences of the USA* **111**, E4298–E4304.

Arndt, N. T., Czamanske, G. K., Wooden, J. L. & Fedorenko, V. A. (1993). Mantle and crustal contributions to continental flood volcanism. *Tectonophysics* **223**, 39–52.

Ashwal, L. D. (2021). Sub-lithospheric mantle sources for overlapping southern African Large Igneous Provinces. *South African Journal of Geology* **124**, 421–442.

Balkwill, H. R. (1978). Evolution of Sverdrup Basin, Arctic Canada. *AAPG Bulletin* **62**, 1004–1028.

Bartels, K. S., Kinzler, R. H. & Grove, T. L. (1991). High-pressure phase relations of primitive high-alumina basalts from Medicine Lake volcano, northern California. *Contributions to Mineralogy and Petrology* **108**, 253–270.

Beard, C. D., Scoates, J. S., Weis, D., Bédard, J. H. & Dell'Oro, T. A. (2017). Geochemistry and origin of the Neoproterozoic Natkusiak flood basalts and related Franklin sills, Victoria Island, Arctic Canada. *Journal of Petrology* **58**, 2191–2220.

Bédard, J. H. (2005). Partitioning coefficients between olivine and silicate melts. *Lithos* **83**, 394–419.

Bédard, J. H. (2006). Trace element partitioning in plagioclase feldspar. *Geochimica et Cosmochimica Acta* **70**, 3717–3742.

Bédard, J. H. (2014). Parameterizations of calcic clinopyroxene–melt trace element partition coefficients. *Geochemistry, Geophysics, Geosystems* **15**, 303–336.

Bédard, J. H., Marsh, B. D., Hersum, T. G., Naslund, H. R. & Mukasa, S. B. (2007). Large-scale mechanical redistribution of orthopyroxene and plagioclase in the Basement Sill, Ferrar dolerites, McMurdo Dry Valleys, Antarctica: Petrological, mineral-chemical and field evidence for channelized movement of crystals and melt. *Journal of Petrology* **48**, 2289–2326.

Bédard, J. H., Naslund, H. R., Nabelek, P., Winpenny, A., Hryciuk, M., MacDonald, W., Hayes, B., Steigerwaldt, K., Hadlari, T., Rainbird, R., Dewing, K. & Girard, É. (2012). Fault-mediated melt ascent in a Neoproterozoic continental flood basalt province, the Franklin sills, Victoria Island, Canada. *Geological Society of America Bulletin* **124**, 723–736.

Bédard, J. H., Troll, V. R. & Deegan, F. M. (2016). HALIP intrusions, contact metamorphism, and incipient diapirism of gypsum-carbonate sequences. In: Williamson, M.-C. (ed.) *Report of Activities for High Arctic Large Igneous Province (HALIP)—GEM 2 Western Arctic Region Project: Bedrock Mapping and Mineral Exploration. Geological Survey of Canada Open File* **7950**, pp. 3–13 doi.org/10.4095/297783

Bédard, J. H., Troll, V. R. & Deegan, F. M. (2018). Evidence for differentiation of High Arctic Large Igneous Province basalt at depth. In*: International Conference on Arctic Margins* **VIII**, Stockholm, 11–14 June, Abstract. Bolin Center for Climate Research, Stockholm, Sweden. https://icamviii.geo.su.se/en.

Bédard, J. H., Deegan, F. M., Troll, V. R., Dewing, K., Grasby, S. E. & Saumur, B. M. (2019). High Arctic Large igneous province magmatism in Canada: geochemical and petrologic constraints on petrogenesis. In: *American Geophysical Union Chapman Conference, Large-scale Volcanism in the Arctic: The Role of the Mantle and Tectonics, October 13–18, 2019, Selfoss, Iceland, Abstracts*. AGU. https://agu.confex.com/agu/19chapman3.

Bédard, J. H., Saumur, B. M., Williamson, M.-C., Tegner, C., Troll, V. R., Deegan, F. M., Evenchick, C. A., Grasby, S. E. & Dewing, K. (2020). Geochemical database of Cretaceous High Arctic Large Igneous Province magmatic rocks, Arctic Canada. *Geological Survey of Canada Open File* **8759**, 7 pp.

Bédard, J. H., Troll, V. R., Deegan, F. M., Tegner, C., Saumur, B.-M., Evenchick, C. A., Grasby, S. E. & Dewing, K. (2021). High Arctic Large Igneous Province alkaline rocks in Canada: evidence for multiple mantle components. *Journal of Petrology* in press, doi.org/10.1093/petrology/egab042/5295685

Bender, J. F., Hodges, F. N. & Bence, A. E. (1978). Petrogenesis of basalts from the project FAMOUS area: experimental study from 0 to 15 kbars. *Earth and Planetary Science Letters* **41**, 277–302.

Bhattacharya, S. K., Ma, G. S.-K. & Matsuhisa, Y. (2013). Oxygen isotope evidence for crustal contamination in Deccan Basalts. *Geochemistry* **73**, 105–112.

Boudreau, A. E. (1999). PELE—a version of the MELTS software program for the PC platform. *Computers & Geosciences* **25**, 201–203.

Bowen, N. L. (1928). *Evolution of the Igneous Rocks*. Princeton, NJ: Princeton University Press, 334 pp.

Buchan, K. L. & Ernst, R. E. (2006). Giant dyke swarms and the reconstruction of the Canadian Arctic Islands, Greenland, Svalbard and Franz Josef Land. In: Hanski, E., Mertanen, S., Rämö, T. & Vuollo, J. (eds.) *Dyke Swarms: Time Markers of Crustal Evolution*. London: Taylor & Francis; Rotterdam: Balkema, pp. 27–48.

Buchan, K. L. & Ernst, R. E. (2018). A giant circumferential dyke swarm associated with the High Arctic Large Igneous Province (HALIP). *Gondwana Research* **58**, 39–57.

Callegaro, S., Marzoli, A., Bertrand, H., Chiaradia, M., Reisberg, L., Meyzen, C., Bellieni, G., Weems, R. E. & Merle, R. (2013). Upper and lower crust recycling in the source of CAMP basaltic dykes from southeastern North America. *Earth and Planetary Science Letters* **376**, 186–199.

Callegaro, S., Rapaille, C., Marzoli, A., Bertrand, H., Chiaradia, M., Reisberg, L., Bellieni, G., Martins, L., Madeira, J., Mata, J., Youbi, N., De Min, A., Azevedo, M. R. & Bensalah, M. K. (2014). Enriched mantle source for the Central Atlantic magmatic province: new supporting evidence from southwestern Europe. *Lithos* **188**, 15–32.

Chernykh, A., Glebovsky, V., Zykov, M. & Korneva, M. (2018). New insights into tectonics and evolution of the Amerasia Basin. *Journal of Geodynamics* **119**, 167–182.

Cox, K. G. (1980). A model for flood basalt vulcanism. *Journal of Petrology* **21**, 629–650.

Deegan, F. M., Bédard, J. H., Troll, V. R., Dewing, K., Grasby, S. E., Sanei, H., Harris, C., Yakymchuck, C., Sheih, S. R., Freda, C., Misiti, V., Mollo, S., Geiger, H. & Evenchick, C. A. (2018a). Impact of basaltic sills on sedimentary host rocks in the High Arctic Large Igneous Province. *Geophysical Research Abstracts* **20**, EGU2018-17845.

Deegan, F. M., Bédard, J. H., Troll, V. R., Whitehouse, M. J., Hagerfors, E. & Geiger, H. (2018b). Sulphur mobilisation from sedimentary host rocks in the High Arctic Large Igneous Province. Poster. International Conference on Arctic Margins VIII, Stockholm, 11–14 June.

DePaolo, D. J. (1981). Trace element and isotopic effects of combined wallrock assimilation and fractional crystallization. *Earth and Planetary Science Letters* **53**, 189–202.

Dewing, K. & Embry, A. F. (2007). Geological and geochemical data from the Canadian Arctic Islands. Part I: Stratigraphic tops from Arctic Islands' oil and gas exploration boreholes. *Geological Survey of Canada Open File Report* **5442** (CD-ROM).

Dockman, D. M., Pearson, D. G., Heaman, L. M., Gibson, S. A. & Sarkar, C. (2018). Timing and origin of magmatism in the Sverdrup Basin, Northern Canada—implications for lithospheric evolution in the High Arctic Large Igneous Province (HALIP). *Tectonophysics* **742–743**, 50–65.

Døssing, A., Jackson, H. R., Matzka, J., Einarsson, I., Rasmussen, T. M., Olesen, A. V. & Brozena, J. M. (2013). On the origin of the Amerasia Basin and the High Arctic Large Igneous Province: results of new aeromagnetic data. *Earth and Planetary Science Letters* **363**, 219–230.

Dostal, J. & MacRae, A. (2018). Cretaceous basalts of the High Arctic large igneous province at Axel Heiberg Island (Canada): Volcanic stratigraphy, geodynamic setting, and origin. *Geological Journal* **53**, 2918–2934.

Duffield, W. A. & Ruiz, J. (1998). A model that helps explain Sr-isotope disequilibrium between feldspar phenocrysts and melt in large-volume silicic magma systems. *Journal of Volcanology and Geothermal Research* **87**, 7–13.

Ellam, R. M. (1992). Lithospheric thickness as a control on basalt geochemistry. *Geology* **20**, 153–156.

Ellam, R. M. & Cox, K. G. (1991). An interpretation of Karoo picrite basalts in terms of interaction between asthenospheric magmas and mantle lithosphere. *Earth and Planetary Science Letters* **105**, 330–342.

Embry, A. F. (1991). Mesozoic history of the Arctic Islands. In: Trettin, H. P. (ed.) *Geology of the Innuitian Orogen and Arctic Platform of Canada and Greenland. Geological Survey of Canada, Geology of Canada No. 3*, 371–433.

Embry, A. F. & Beauchamp, B. (2019). The Sverdrup Basin. In: Miall, A. D. (ed.) *Sedimentary Basins of the United Stated and Canada*, 2nd edn. Amsterdam: Elsevier, pp. 559–592

Embry, A. F. & Osadetz, K. G. (1988). Stratigraphy and tectonic significance of Cretaceous volcanism in the Queen Elizabeth Islands, Canadian Arctic Archipelago. *Canadian Journal of Earth Sciences* **25**, 1209–1219.

Ernst, R. E. (2014). *Large Igneous Provinces*. Cambridge: Cambridge University Press, 653 pp.

Ernst, R. E. & Baragar, W. R. A. (1992). Evidence from magnetic fabric for the flow pattern of magma in the Mackenzie giant radiating dyke swarm. *Nature* **356**, 511–513.

Ernst, R. E. & Buchan, K. L. (2010). *Geochemistry database of Proterozoic mafic–ultramafic magmatism in Canada. Geological Survey of Canada Open File* **6016** (CD-ROM).

Estrada, S. (2015). Geochemical and Sr–Nd isotope variations within Cretaceous continental flood-basalt suites of the Canadian High Arctic, with a focus on the Hassel Formation basalts of northeast Ellesmere Island. *International Journal of Earth Sciences* **104**, 1981–2005.

Estrada, S. & Henjes-Kunst, F. (2004). Volcanism in the Canadian High Arctic related to the opening of the Arctic Ocean. *Zeitschrift der Deutschen Gesellschaft für Geowissenschaften* **154**, 579–603.

Estrada, S. & Henjes-Kunst, F. (2013). ^{40}Ar–^{39}Ar and U–Pb dating of Cretaceous continental rift-related magmatism on the northeast Canadian Arctic margin. *Zeitschrift der Deutschen Gesellschaft für Geowissenschaften* **164**, 107–130.

Estrada, S. & Piepjohn, K. (2018). Early Cretaceous magmatism and post-Early Cretaceous deformation on Ellef Ringnes Island, Canadian High Arctic, related to the formation of the Arctic Ocean. In: Piepjohn, K., Strauss, J. V., Reinhardt, L. & McClelland, W. C. (eds) *Circum-Arctic Structural Events: Tectonic Data Evolution of the Arctic Margins and Trans-Arctic Links with Adjacent Orogens. Geological Society of America, Special Papers* **541**, 303–323. 10.1130/2018.2541(15)

Estrada, S., Damaske, D., Henjes-Kunst, F., Schreckenberger, B., Oakey, G. N., Piepjohn, K., Eckelmann, K. & Linnemann, U. (2016). Multistage Cretaceous magmatism in the northern coastal region of Ellesmere Island and its relation to the formation of Alpha Ridge—evidence from aeromagnetic, geochemical and geochronological data. *Norwegian Journal of Geology* **96**, 65–95.

Estrada, S., Mende, K., Gerdes, A., Gärtner, A., Hofmann, M., Spiegel, C., Damaske, D., Estrada, S., Mende, K., Gerdes, A., Gärtner, A., Hofmann, M., Spiegel, C., Damaske, D. & Koglin, N. (2018). Proterozoic to Cretaceous evolution of the western and central Pearya Terrane (Canadian High Arctic). *Journal of Geodynamics* **120**, 45–76.

Evenchick, C. A., Davis, W. J., Bédard, J. H., Hayward, N. & Friedman, R. M. (2015). Evidence for protracted High Arctic Large Igneous Province magmatism in the central Sverdrup Basin from stratigraphy, geochronology, and paleodepths of saucer-shaped sills. *Geological Society of America Bulletin* **127**, 1366–1390.

Foulger, G. R., Natland, J. H. & Anderson, D. L. (2005). A source for Icelandic magmas in remelted Iapetus crust. *Journal of Volcanology and Geothermal Research* **141**, 23–44.

Francis, D. M., Hynes, A. J., Ludden, J. N. & Bédard, J. H. (1981). Crystal fractionation and partial melting in the petrogenesis of a Proterozoic high-MgO volcanic suite, Ungava, Quebec. *Contributions to Mineralogy and Petrology* **78**, 27–36.

Fukao, Y., Obayashi, M., Nakakuki, T. & the Deep Slab Project Group (2009). Stagnant slab: a review. *Annual Review of Earth and Planetary Sciences* **37**, 19–46.

Gast, P. W. (1968). Trace element fractionation and the origin of tholeiitic and alkaline magma types. *Geochimica et Cosmochimica Acta* **32**, 1057–1086.

Gibson, S. A. & Geist, D. (2010). Geochemical and geophysical estimates of lithospheric thickness variation beneath Galápagos. *Earth and Planetary Science Letters* **300**, 275–286.

Gibson, S. A., Thompson, R. N., Dickin, A. P. & Leonardos, O. H. (1995). High-Ti and low-Ti mafic potassic magmas: Key to plume–lithosphere interactions and continental flood-basalt genesis. *Earth and Planetary Science Letters* **136**, 149–165.

Grantz, A., Hart, P. E. & Childers, V. A. (2011). Geology and tectonic development of the Amerasia and Canada Basins, Arctic Ocean. In: Spencer, A. M., Embry, A. F., Gautier, D. L., Stoupakova, A. V. & Sørensen, K. (eds) *Arctic Petroleum Geology. Geological Society, London, Memoirs* **35**, 771–799.

Green, D. H. (2015). Experimental petrology of peridotites, including effects of water and carbon on melting in the Earth's upper mantle. *Physics and Chemistry of Minerals* **42**, 95–122.

Hadlari, T., MacLean, B. C., Galloway, J. M., Sweet, A. R., White, J. M., Thomson, D., Gabites, J. & Schröder-Adams, C. J. (2014). The flexural margin, the foredeep, and the orogenic margin of a northern Cordilleran foreland basin: Cretaceous tectonostratigraphy and detrital zircon provenance, northwestern Canada. *Marine and Petroleum Geology* **57**, 173–186.

Hadlari, T., Midwinter, D., Galloway, J. M., Dewing, K. & Durbano, A. M. (2016). Mesozoic rift to post-rift tectonostratigraphy of the Sverdrup Basin. *Marine and Petroleum Geology* **76**, 148–158.

Hadlari, T., Dewing, K., Matthews, W. A., Alonso-Torres, D. & Midwinter, D. (2018). Early Triassic development of a foreland basin in the Canadian high Arctic: implications for a Pangean Rim of Fire. *Tectonophysics* **736**, 75–84.

Hansen, G. N. (1980). Rare earth elements in petrogenetic studies of igneous systems. *Annual Review of Earth and Planetary Sciences* **8**, 371–406.

Hawkesworth, C. J., Marsh, J. S., Duncan, A. R., Erlank, A. J. & Norry, M. J. (1984). The role of continental lithosphere in the generation of the Karoo volcanic rocks: evidence from combined Nd- and Sr-isotope studies. In: Erlank, A. J. (ed.) *Petrogenesis of the Volcanic Rocks of the Karoo Province. Geological Society of South Africa, Special Publication* **13**, 341–354.

Hawkesworth, C., Gallagher, K., Kelley, S., Mantovani, M., Peate, D., Regelous, M. & Rogers, N. (1992). Paraná magmatism and the opening of the South Atlantic. In: Storey, B. C., Alabaster, T. & Pankhurst, R. J. (eds) *Magmatism and the Causes of Continental Break-up. Geological Society, London, Special Publications* **68**, 221–240.CrossRef] [10.1144/GSL.SP.1992.068.01.14]

Hayes, B., Bédard, J. H. & Lissenberg, C. J. (2015). Olivine slurry replenishment and the development of igneous layering in a Franklin Sill, Victoria Island, Arctic Canada. *Journal of Petrology* **56**, 83–112.

Heinonen, J. S., Luttinen, A. V. & Bohrson, W. A. (2016). Enriched continental flood basalts from depleted mantle melts: modeling the lithospheric contamination of Karoo lavas from Antarctica. *Contributions to Mineralogy and Petrology* **171**, 9.

Herzberg, C. & Asimow, P. D. (2008). Petrology of some oceanic island basalts: PRIMELT2.XLS software for primary magma calculation. *Geochemistry, Geophysics, Geosystems* **9**, doi: 10.1029GC002057

Hofmann, A. W. (1997). Mantle geochemistry: the message from oceanic volcanism. *Nature* **385**, 219–229.

Ionov, D. A., Dupuy, C., O'Reilly, S. Y., Kopylova, M. G. & Genshaft, Y. S. (1993). Carbonated peridotite xenoliths from Spitsbergen: implications for trace element signature of mantle carbonate metasomatism. *Earth and Planetary Science Letters* **119**, 283–297.

Irvine, T. N. & Baragar, W. R. A. (1971). A guide to the chemical classification of the common volcanic rocks. *Canadian Journal of Earth Sciences* **8**, 523–548.

Irving, A. J. & Green, D. H. (2008). Phase relationships of hydrous alkalic magmas at high pressures: production of nepheline hawaiitic to mugearitic liquids by amphibole-dominated fractional crystallization within the lithospheric mantle. *Journal of Petrology* **49**, 741–756.

Ivanov, A. V. & Litasov, K. D. (2013). The deepwater cycle and flood basalt volcanism. *International Geology Review* **56**, 1–14.

Ivanov, A., Demonterova, E., Rasskazov, S. & Yasnygina, T. (2008). Low-Ti melts from the southeastern Siberian Traps Large Igneous Province: evidence for a water-rich mantle source? *Journal of Earth System Science* **117**, 1–21.

Jochum, K. P., Hofmann, A. W., Ito, E., Seufert, H. M. & White, W. M. (1983). K, U and Th in mid-ocean ridge basalt glasses and heat production, K/U and K/Rb in the mantle. *Nature* **306**, 431–436.

Jourdan, F., Féraud, G., Bertrand, H., Watkeys, M. K. & Renne, P. R. (2007). Distinct brief major events in the Karoo large igneous province clarified by new ^{40}Ar/^{39}Ar ages on the Lesotho basalts. *Lithos* **98**, 195–209.

Jourdan, F., Bertrand, H., Féraud, G., Le Gall, B. & Watkeys, M. K. (2009). Lithospheric mantle evolution monitored by overlapping large igneous provinces: case study in southern Africa. *Lithos* **107**, 257–268.

Jowitt, S. M., Williamson, M.-C. & Ernst, R. E. (2014). Geochemistry of the 130 to 80 Ma Canadian High Arctic Large Igneous province (HALIP) event and implications for Ni–Cu–PGE prospectivity. *Economic Geology* **109**, 281–307.

Kaislaniemi, L. & van Hunen, J. (2014). Dynamics of lithospheric thinning and mantle melting by edge-driven convection: application to Moroccan Atlas Mountains. *Geochemistry, Geophysics, Geosystems* **15**, 3175–3189.

Kimura, J. I., Sakuyama, T., Miyazaki, T., Vaglarov, B. S., Fukao, Y. & Stern, R. J. (2018). Plume-stagnant slab–lithosphere interactions: origin of the late Cenozoic intra-plate basalts on the East Eurasia margin. *Lithos* **300–301**, 227–249.

King, S. D. & Anderson, D. L. (1998). Edge-driven convection. *Earth and Planetary Science Letters* **160**, 289–296.

Kingsbury, C. G. (2016). Hot rocks from cold places: a field, geochemical and geochronological study from the High Arctic Large Igneous Province (HALIP) at Axel Heiberg Island, Nunavut. PhD thesis, Carleton University, Ottawa, 199 pp.

Kingsbury, C. G., Ernst, R. E., Cousens, B. L. & Williamson, M.-C. (2016). The High Arctic LIP in Canada: trace element and Sm–Nd isotopic evidence for the role of mantle heterogeneity and crustal assimilation. *Norwegian Journal of Geology* **96**, 13–33.

Kingsbury, C. G., Kamo, S. L., Ernst, R. E., Söderlund, U. & Cousens, B. L. (2018). U–Pb geochronology of the plumbing system associated with the Late Cretaceous Strand Fiord Formation, Axel Heiberg Island. *Journal of Geodynamics* **118**, 106–117.

Klemme, S., Günther, D., Hametner, K., Prowatke, S. & Zack, T. (2006). The partitioning of trace elements between ilmenite, ulvospinel, armalcolite and silicate melts with implications for the early differentiation of the moon. *Chemical Geology* **234**, 251–263.

Kontak, D. J., Jensen, S. M., Dostal, J., Archibald, D. A. & Kyser, T. K. (2001). Cretaceous mafic dyke swarm, Peary Land, Northernmost Greenland: Geochronology and petrology. *Canadian Mineralogist* **39**, 997–1020.

Lassiter, J. C. & DePaolo, D. J. (1997). Plume/lithosphere interaction in the generation of continental and oceanic flood basalts: chemical and isotopic constraints. In: Mahoney, J. J. & Coffin, M. F. (eds) *Large Igneous Provinces: Continental, Oceanic and Planetary Flood Volcanism. American Geophysical Union, Geophysical Monograph* **100**, 335–355.

Latypov, R. M. (2003). The origin of basic-ultrabasic sills with S-, D-, and I-shaped compositional profiles by *in situ* crystallization of a single input of phenocryst-poor parental magma. *Journal of Petrology* **44**, 1619–1656.

Le Bas, M. J., Le Maitre, R. W., Streckeisen, A. & Zanettin, B., IUGS Subcommission on the Systematics of Igneous Rocks (1986). A chemical classification of volcanic rocks based on the total alkali–silica diagram. *Journal of Petrology* **27**, 745–750.

Lightfoot, P. C., Hawkesworth, C. J., Hergt, J., Naldrett, A. J., Gorbachev, N. S., Fedorenko, V. A. & Doherty, W. (1993). Remobilisation of the continental lithosphere by a mantle plume: major-, trace-element, and Sr-, Nd-, and Pb-isotope evidence from picritic and tholeiitic lavas of the Noril'sk District, Siberian Trap, Russia. *Contributions to Mineralogy and Petrology* **114**, 171–188.

Luttinen, A. V. (2018). Bilateral geochemical asymmetry in the Karoo large igneous province. *Scientific Reports* **8**, 5223.

Luttinen, A. V., Heinonen, J. S., Kurhila, M., Jourdan, F., Mänttäri, I., Vuori, S. K. & Huhma, H. (2015). Depleted mantle-sourced CFB magmatism in the Jurassic Africa–Antarctica Rift: petrology and ^{40}Ar/^{39}Ar and U/Pb chronology of the Vestfjella Dyke Swarm, Dronning Maud Land, Antarctica. *Journal of Petrology* **56**, 919–952.

MacDonald, G. A. (1968). Composition and origin of Hawaiian Lavas. In: Coats, R., Hay, R.L. & Anderson, C.A. (eds) . *Studies in Volcanology. Geological Society of America, Memoirs* **116**, 477–522.

Maher, H. D. J. (2001). Manifestations of the Cretaceous High Arctic Large Igneous Province in Svalbard. *Journal of Geology* **109**, 91–104.

Magee, C., Muirhead, J. D., Karvelas, A., Holford, S. P., Jackson, C. A. L., Bastow, I. D., Schofield, N., Stevenson, C. T. E., McLean, C., McCarthy, W. & Shtukert, O. (2016). Lateral magma flow in mafic sill complexes. *Geosphere* **12**, 809–841.

Maruyama, S. & Okamoto, K. (2007). Water transportation from the subducting slab into the mantle transition zone. *Gondwana Research* **11**, 148–165.

Marzoli, A., Callegaro, S., Dal Corso, J., Davies, J. H. F. L., Chiaradia, M., Youbi, N., Bertrand, H., Reisberg, L., Merle, R. & Jourdan, F. (2018). The Central Atlantic Magmatic Province: a review. In: Tanner, L. H. (ed.) *The Late Triassic World*. Berlin: Springer, pp. 91–125.

McKenzie, D. & O'Nions, R. K. (1991). Partial melt distributions from inversion of rare earth element concentrations. *Journal of Petrology* **32**, 1021–1091.

Meade, F. C., Troll, V. R., Ellam, R. M., Freda, C., Font, L., Donaldson, C. H. & Klonowska, I. (2014). Bimodal magmatism produced by progressively inhibited crustal assimilation. *Nature Communications* **5**, 4199.

Merle, R., Marzoli, A., Reisberg, L., Bertrand, H., Nemchin, A., Chiaradia, M., Callegaro, S., Jourdan, F., Bellieni, G., Kontak, D., Puffer, J. & McHone, J. G. (2014). Sr, Nd, Pb and Os isotope systematics of CAMP tholeiites from Eastern North America (ENA): evidence of a subduction-enriched mantle source. *Journal of Petrology* **55**, 133–180.

Murphy, J. B. & Dostal, J. (2007). Continental mafic magmatism of different ages in the same terrane: constraints on the evolution of an enriched mantle source. *Geology* **35**, 335–338.

Naber, T. V., Grasby, S. E., Cuthbertson, J. P., Rayner, N. & Tegner, C. (2021). Tracing the extension of the Alpha Ridge onto Ellesmere Island, Canada: New constraints on the age and geochemistry of High Arctic Large Igneous Province magmatism. *Geological Society of America Bulletin, 133, 1695–1711*, doi.org/10.1130/B35792.1.

Niu, Y., Wilson, M., Humphreys, E. R. & O'Hara, M. J. (2011). The origin of intra-plate ocean island basalts (OIB): the lid effect and its geodynamic implications. *Journal of Petrology* **52**, 1443–1468.

O'Hara, M. J. (1977). Geochemical evolution during fractionation crystallization of a periodically refilled magma chamber. *Nature* **266**, 503–507.

O'Hara, M. J. & Herzberg, C. (2002). Interpretation of trace element and isotope features of basalts: Relevance of field relations, petrology, major element data, phase equilibria, and magma chamber modeling in basalt petrogenesis. *Geochimica et Cosmochimica Acta* **66**, 2167–2191.

O'Hara, M. J. & Mathews, R. E. (1981). Geochemical evolution in an advancing, periodically replenished, periodically tapped, continuously fractionated magma chamber. *Journal of the Geological Society, London* **138**, 237–277.

O'Neill, H. S. C. (2016). The smoothness and shapes of chondrite-normalized rare earth element patterns in basalts. *Journal of Petrology* **57**, 1463–1508.

O'Neill, H. S. C. & Jenner, F. E. (2012). The global pattern of trace-element distributions in ocean floor basalts. *Nature* **491**, 698–704.

Osadetz, K. G. & Moore, P. R. (1988). *Basic volcanics in the Hassel Formation (Mid-Cretaceous) and associated intrusives, Ellesmere Island, District of Franklin, Northwest Territories. Geological Survey of Canada Paper* **87-21**, 19 pp.

Pearce, J. A. (2008). Geochemical fingerprinting of oceanic basalts with applications to ophiolite classification and the search for Archean oceanic crust. *Lithos* **100**, 14–48.

Pearce, J. A. (2014). Immobile element fingerprinting of basalts. *Elements* **10**, 101–108.

Philpotts, A. R., Carroll, M. & Hill, J. M. (1996). Crystal-mush compaction and the origin of pegmatitic segregation sheets in a thick flood-basalt flow in the Mesozoic Hartford basin. *Journal of Petrology* **37**, 811–836.

Piepjohn, K. & von Gosen, W. (2018). Structural transect through Ellesmere Island (Canadian Arctic): superimposed Palaeozoic Ellesmerian and Cenozoic Eurekan deformation. In: Pease, V. & Coakley, B. (eds) *Circum-Arctic Lithosphere Evolution. Geological Society, London, Special Publications* **460**, 33–56.

Piepjohn, K., von Gosen, W., Estrada, S. & Tessensohn, F. (2007). Deciphering superimposed Ellesmerian and Eurekan deformation, Piper Pass area, northern Ellesmere Island (Nunavut). *Canadian Journal of Earth Sciences* **44**, 1439–1452.

Piepjohn, K., von Gosen, W. & Tessensohn, F. (2016). The Eurekan deformation in the Arctic: an outline. *Journal of the Geological Society, London* **173**, 1007–1024.

Potter, K. E., Shervais, J. W., Christiansen, E. H. & Vetter, S. K. (2018). Evidence for cyclical fractional crystallization, recharge, and assimilation in basalts of the Kimama drill core, Central Snake River Plain, Idaho: 5·5 million years of petrogenesis in a mid-crustal sill complex. *Frontiers in Earth Science* **6**, 1–17.

Puffer, J. H. (2001). Contrasting high field strength element contents of continental flood basalts from plume versus reactivated-arc sources. *Geology* **29**, 675–678.

Ricketts, B. D., Osadetz, K. G. & Embry, A. F. (1985). Volcanic style in the Strand Fiord Formation (Upper Cretaceous), Axel Heiberg Island, Canadian Arctic Archipelago. *Polar Research* **3**, 107–122.

Roeder, P. L. & Emslie, R. F. (1970). Olivine–liquid equilibrium. *Contributions to Mineralogy and Petrology* **29**, 275–289.

Rooney, T. O., Nelson, W. R., Ayalew, D., Hanan, B., Yirgu, G. & Kappelman, J. (2017). Melting the lithosphere: Metasomes as a source for mantle-derived magmas. *Earth and Planetary Science Letters* **461**, 105–118.

Rudnick, R. L. (1995). Making continental crust. *Nature* **378**, 571–578.

Ruppel, A., Damaske, D. & Piepjohn, K. (2018). Aeromagnetic high-resolution survey over the Vendom Fiord Region, Ellesmere Island, Canadian High Arctic. In: Piepjohn, K., Strauss, J. V., Reinhardt, L. & McClelland, W. C. (eds) *Circum-Arctic Structural Events: Tectonic Evolution of the Arctic Margins and Trans-Arctic Links with Adjacent Orogens. Geological Society of America, Special Papers* **541**, 1–18, doi.org/10.1130/2018.2541(17)

Sack, R. O., Walker, D. & Carmichael, I. S. E. (1987). Experimental petrology of alkali lavas: Constraints on cotectics of multiple saturation in natural basic liquids. *Contributions to Mineralogy and Petrology* **96**, 1–23.

Stephenson, R., Piepjohn, K., Schiffer, C., von Gosen,, W., Oakey, G. N. & Anudu, G. (2018). Integrated crustalgeological cross-section of Ellesmere Island. In: Pease, V. & Coakley, B. (eds) Circum-Arctic Lithosphere Evolution, Geological Society, London, Special Publication **460**, 7–17, https://doi.org/10.1144/SP460.12.

Saumur, B. M. (2015). HALIP legacy samples, part I—the Ottawa collection. In: Dewing, K. (ed.) *Report of Activities for the High Arctic Large Igneous Province (HALIP) GEM 2 Western Arctic Project. Geological Survey of Canada Open File* **7976**, 9–16.

Saumur, B. M. & Williamson, M.-C. (2016). Geochemistry of volcanic rocks from the High Arctic Large Igneous Province (HALIP), Axel Heiberg Island and Ellesmere Island, Nunavut, Canada, Geological Survey of Canada Open File. **8002**, 22.

Saumur, B. M., Williamson, M.-C., Muecke, A. & Muecke, G. (2015). HALIP legacy samples, Part II—the Dalhousie Collection. In: Dewing, K. (ed.) *Report of Activities for the High Arctic Large Igneous Province (HALIP) GEM 2 Western Arctic Project. Geological Survey of Canada Open File* **7976**, 17–19.

Saumur, B. M., Dewing, K. & Williamson, M.-C. (2016). Architecture of the Canadian portion of the High Arctic Large Igneous Province and implications for magmatic Ni–Cu potential. *Canadian Journal of Earth Sciences* **53**, 528–542.

Saumur, B. M., Williamson, M. C. & Bédard, J. H. (2021). Targeting magmatic Ni–Cu mineralization in the Canadian High Arctic large igneous province: integrating geochemistry, magmatic architecture and structure. Mineralium Deposita in press, doi:10.1007/s00126-021-01054-3

Schiffer, C. & Stephenson, R. (2018). Regional crustal architecture of Ellesmere Island, Arctic Canada. In: Pease, V. & Coakley, B. (eds) *Circum-Arctic Lithosphere Evolution. Geological Society, London, Special Publications* **460**, 19–32.

Shaw, D. M. (1970). Trace element fractionation during anatexis. *Geochimica et Cosmochimica Acta* **34**, 237–243.

Shephard, G. E., Trønnes, R. G., Spakman, W., Panet, I. & Gaina, C. (2016). Evidence for slab material under Greenland and links to Cretaceous High Arctic magmatism. *Geophysical Research Letters* **43**, 3717–3726.

Sievwright, R. H., Wilkinson, J. J., O'Neill, H., St C. & Berry, A. J. (2017). Thermodynamic controls on element partitioning between titanomagnetite and andesitic–dacitic silicate melts. *Contributions to Mineralogy and Petrology* **172**, 62.

Sobolev, A. V., Hofmann, A. W., Kuzmin, D. V., Yaxley, G. M., Arndt, N. T., Chung, S. L., Danyushevsky, L. V., Elliott, T., Frey, F. A., Garcia, M. O., Gurenko, A. A., Kamenetsky, V. S., Kerr, A. C., Krivolutskaya, N. A., Matvienkov, V. V., Nikogosian, I. K., Rocholl, A., Sigurdsson, I. A., Sushchevskaya, N. M. & Teklay, M. (2007). The amount of recycled crust in sources of mantle-derived melts. *Science* **316**, 412–417.

Stracke, A. (2012). Earth's heterogeneous mantle: a product of convection-driven interaction between crust and mantle. *Chemical Geology* **330–331**, 274–299.

Sun, S.-S. & McDonough, W. F. (1989). Chemical and isotopic systematics of oceanic basalts: implications for mantle compositions and processes. In: Saunders, A. D. & Norry, M. J. (eds) *Magmatism in the Ocean Basins. Geological Society, London, Special Publications* **42**, 313–345.

Tegner, C., Storey, M., Holm, P. M., Thorarinsson, S. B., Zhao, X., Lo, C. H. & Knudsen, M. F. (2011). Magmatism and Eurekan deformation in the High Arctic Large Igneous Province: ^{40}Ar/^{39}Ar age of Kap Washington Group Volcanics, North Greenland. *Earth and Planetary Science Letters* **303**, 203–214.

Tegner, C., Michelis, S. A. T., McDonald, I., Brown, E. L., Youbi, N., Callegaro, S., Lindström, S. & Marzoli, A. (2019). Mantle dynamics of the Central Atlantic Magmatic Province (CAMP): constraints from platinum group, gold and lithophile elements in flood basalts of Morocco. *Journal of Petrology* **60**, 1621–1652.

Thompson, R. N., Esson, J. & Dunham, A. C. (1972). Major element chemical variation in the Eocene lavas of the Isle of Skye, Scotland. *Journal of Petrology* **13**, 219–253.

Thompson, R. N., Gibson, I. L., Marriner, G. F., Mattey, D. P. & Morrison, M. A. (1980). Trace element evidence of multistage mantle fusion and polybaric fractional crystallization in the Palaeocene lavas of Skye, NW Scotland. *Journal of Petrology* **21**, 265–293.

Thorsteinsson, R. (1971). *Geology, Strand Fiord. Geological Survey of Canada. Map* **1301A**.

Thorsteinsson, R. & Tozer, E. T. (1970). Geology of the Arctic Archipelago. In: Douglass, R. J. W. (ed.) *Geology and Economic Minerals of Canada. Geological Survey of Canada Economic Geology Report* **1**, 547–590.

Townsend, M., Pollard, D. & Smith, R. (2017). Mechanical models for dikes: A third school of thought. *Tectonophysics* **703–704**, 98–1016.

Trettin, H. P. (1987). Pearya: a composite terrane with Caledonian affinities in northern Ellesmere Island. *Canadian Journal of Earth Sciences* **24**, 224–245.

Trettin, H. P. (1989). The Arctic Islands. In: Bally, A. W. & Palmer, A. R. (eds) *The Decade of North American Geology. The Geology of North America. An Overview*. Boulder, CO: Geological Society of America, pp. 349–370.

Trettin, H. P. (1991a). The Proterozoic to Late Silurian record of Pearya. In: Trettin, H. P. (ed.) *Geology of the Innuitian Orogen and Arctic Platform of Canada and Greenland. Geological Survey of Canada, Geology of Canada* **3**, 241–259.

Trettin, H. P. (1991b). Tectonic Framework. In: Trettin, H. P. (ed.) *Geology of the Innuitian Orogen and Arctic Platform of Canada and Greenland. Geological Survey of Canada, Geology of Canada* **3**, 59–66.

Trettin, H. P. (1991c). Middle Devonian to Early Carboniferous Deformations, Northern Ellesmere and Axel Heiberg Islands. In: Trettin, H. P. (ed.) *Geology of the Innuitian Orogen and Arctic Platform of Canada and Greenland. Geological Survey of Canada, Geology of Canada* **3**, 309–317.

Trettin, H. P. (1996). *Chemical analyses of Upper Cretaceous volcanics and related(?) sills, northwestern Ellesmere Island, District of Franklin. Geological Survey of Canada, Open File* **3274**, 30 pp.

Trettin, H. P. & Parrish, R. (1987). Late Cretaceous bimodal magmatism, northern Ellesmere Island: isotopic age and origin. *Canadian Journal of Earth Sciences* **24**, 257–265.

Troll, V. R., Chadwick, J. P., Ellam, R. M., Mc Donnell, S., Emeleus, C. H. & Meighan, I. G. (2005). Sr and Nd isotope evidence for successive crustal contamination of Slieve Gullion ring-dyke magmas, Co. Armagh, Ireland. *Geological Magazine* **142**, 659–688.

Turner, S. & Hawkesworth, C. (1995). The nature of the sub-continental mantle: constraints from the major-element composition of continental flood basalts. *Chemical Geology* **120**, 295–314.

Turner, S., Hawkesworth, C., Gallagher, K., Stewart, K., Peate, D. & Mantovani, M. (1996). Mantle plume, flood basalts, and thermal models for melt generation beneath continents: assessment of a conductive heating model and application to the Paraná. *Journal of Geophysical Research: Solid Earth* **101**, 11503–11518.

Viereck, L. G., Flower, M. F. J., Hertogen, J., Schmincke, H.-U. & Jenner, G. A. (1989). The genesis and significance of N-MORB sub-types. *Contributions to Mineralogy and Petrology* **102**, 112–126.

Walter, M. J. (1998). Melting of garnet peridotite and the origin of komatiite and depleted lithosphere. *Journal of Petrology* **39**, 29–60.

Wang, X.-C., Wilde, S. A., Xu, B. & Pang, C.-J. (2016). Origin of arc-like continental basalts: Implications for deep-Earth fluid cycling and tectonic discrimination. *Lithos* **261**, 5–45.

Weaver, B. L. (1991). The origin of ocean island basalt end-member compositions: trace element and isotopic constraints. *Earth and Planetary Science Letters* **104**, 381–397.

Weis, D., Garcia, M. O., Rhodes, J. M., Jellinek, M. & Scoates, J. S. (2011). Role of the deep mantle in generating the compositional asymmetry of the Hawaiian mantle plume. *Nature Geoscience* **4**, 831–838.

Whalen, L., Gazel, E., Vidito, C., Puffer, J., Bizimis, M., Henika, W. & Caddick, M. J. (2015). Supercontinental inheritance and its influence on supercontinental breakup: The Central Atlantic Magmatic Province and the break up of Pangea. *Geochemistry, Geophysics, Geosystems* **16**, 3532–3554.

White, R. S. & McKenzie, D. (1989). Magmatism at rift zones: the generation of volcanic continental margins and flood basalts. *Journal of Geophysical Research* **94**, 7685–7729.

White, R. S. & McKenzie, D. (1995). Mantle plumes and flood basalts. *Journal of Geophysical Research: Solid Earth* **100**, 17543–17585.

Willbold, M. & Stracke, A. (2010). Formation of enriched mantle components by recycling of upper and lower continental crust. *Chemical Geology* **276**, 188–197.

Williamson, M.-C., Saumur, B.-M. & Evenchick, C. A. (2016). HALIP volcanic–intrusive complexes, Axel Heiberg Island, Nunavut. In: Williamson, M.-C. (ed.) *Report of Activities for High Arctic Large Igneous Province (HALIP)—GEM 2 Western Arctic Region Project: Bedrock Mapping and Mineral Exploration. Geological Survey of Canada Open File* **7950**, 14–26.

Williamson, M.-C., Saumur, B.-M., Grasby, S. E. & Hadlari, T. (2017). *Field studies of High Arctic Large Igneous Province (HALIP) intrusions, Axel Heiberg Island and Ellesmere Island, Nunavut (GEM-2 report of activities, western Arctic region). Geological Survey of Canada Open File* **8169**, 13 pp.

Winchester, J. A. & Floyd, P. A. (1977). Geochemical discrimination of different magma series and their differentiation products using immobile elements. *Chemical Geology* **20**, 325–343.

Wooden, J. L., Czamanske, G. K., Fedorenko, V. A., Arndt, N. T., Chauvel, C., Bouse, R. M., King, B.-S. W., Knight, R. J. & Siems, D. F. (1993). Isotopic and trace-element constraints on mantle and crustal contributions to Siberian continental flood basalts, Noril'sk area, Siberia. *Geochimica et Cosmochimica Acta* **57**, 3677–3704.

Zhang, H.-F., Goldstein, S. L., Zhou, X.-H., Sun, M., Zheng, J.-P. & Cai, Y. (2008). Evolution of subcontinental lithospheric mantle beneath Eastern China: Re–Os isotopic evidence from mantle xenoliths in Paleozoic kimberlites and Mesozoic basalts. *Contributions to Mineralogy and Petrology* **155**, 271–293.